Measurement of the Radiation Exposure for High Altitude Flights in the Polar Region

Dissertation
zur Erlangung des Doktorgrades
der Mathematisch-Naturwissenschaftlichen-Fakultät
der Christian-Albrechts-Universität
zu Kiel

vorgelegt von
Dipl.-Phys. Thomas Möller

Kiel, 2013

Referent: Prof. Dr. Bernd Heber

Korreferent: PD Dr. Frank Wissmann

Tag der mündlichen Prüfung: 28.11.2013

Zum Druck genehmigt: 05.12.2013

gez. Prof. Dr. Wolfgang J. Duschl, Dekan

Zusammenfassung

Die Erde ist fortwährend einer energiereichen Teilchenstrahlung aus dem Weltall ausgesetzt. Diese Strahlung wird Galaktische Kosmische Strahlung genannt und besteht hauptsächlich aus Protonen, Heliumkernen, Elektronen und sehr wenigen schweren Ionen. Ein Teil der Galaktischen Kosmischen Strahlung kann das Magnetfeld der Erde durchdringen und löst durch Wechselwirkungen mit den Luftmolekülen eine Teilchenkaskade aus. Die primären Teilchen und die dabei frei werdenden Sekundärprodukte erzeugen in der Erdatmosphäre ein natürliches Strahlungsfeld, das aus neutralen und geladenen Teilchen besteht. Die Zusammensetzung des Strahlungsfeldes ist abhängig von der magnetischen Breite und von der Höhe, so dass sich das Strahlungsfeld auf Höhe der Internationalen Raumstation (ISS), auf Reiseflughöhe und am Erdboden grundsätzlich unterscheidet. Das Strahlungsfeld am Erdboden ist dominiert von den Zerfallsprodukten der radioaktiven Isotope in der Erdkruste und wird in dieser Arbeit nicht weiter untersucht. Das Strahlungsfeld auf Reiseflughöhe und in Höhe der ISS ist sehr gut bekannt, da die Expositionen des fliegenden Personals und der Astronauten ständig berechnet oder gemessen werden. Für Höhen oberhalb von 20 km und unterhalb des ISS Orbits (400 km) sind die Expositionen durch das Strahlungsfeld jedoch nicht ausreichend gut bekannt. Da in Zukunft das Strahlungsfeld in diesen Höhen zunehmend durch Weltraumtourismus und den für die nahe Zukunft geplanten Überschallflugzeugen immer mehr an Bedeutung gewinnen wird, liegt das Ziel dieser Arbeit in der Untersuchung des Strahlungsfeldes bis in Höhen von 25 km. Für diese Untersuchung wurde ein aus vier Halbleiterdetektoren bestehendes Teilchenteleskop entwickelt. Aufgrund der Anordnung der Detektoren ist es möglich, zwischen geladenen und elektrisch neutralen Teilchen zu unterscheiden. Dieses Teilchenteleskop wurde mit verschiedenen Schwerionen, radioaktiven Quellen und Neutronen bestrahlt und kalibriert. Außerdem wurden verschiedene Messungen auf Reiseflughöhe durchgeführt, um die Funktionsweise des Teilchenteleskops in einem natürlichen und gemischten Strahlungsfeld zu überprüfen. Um bis zu einer Höhe von 25 km Messwerte zu erhalten, wurde ein unbemannter Ballonflug in der Nähe des Polarkreises durchgeführt. Basierend auf dieser Messung konnte die Strahlenexposition bis zu einer Höhe von 25 km abgeschätzt werden.

Abstract

The Earth is permanently exposed to energetic particle radiation from outer space called galactic cosmic rays. The radiation is mainly composed of protons, alpha-particles, some electrons and few heavy nuclei. A part of the galactic cosmic rays can penetrate the Earth's magnetic field, whereby a particle cascade is initialized by nuclear interaction with the molecules of the atmosphere. The primary cosmic ray particles as well as the produced secondary particles form a natural radiation field composed of charged and neutral particles. The composition of the radiation field depends on the geomagnetic latitude and altitude. Thus, the radiation field changes for different altitudes such as at the orbit of the International Space Station (ISS), at common cruising altitudes, and at the ground. The radiation field at ground level is dominated by the terrestrial radiation and it is not considered in this work. Due to the fact that the exposure of air crew and astronauts is permanently calculated and measured, the radiation field at cruising altitudes and onboard the ISS is well known. For altitudes above 20 km and below the ISS orbit (400 km), however, the radiation exposure is mostly unknown. In future the radiation field in these altitudes will become more important because of the emergences of space tourism and new generation supersonic aircraft. Therefore, this work focuses on the radiation exposure up to an altitude of 25 km. For this purpose a particle telescope consisting of four segmented silicon semiconductor detectors was developed. Due to the arrangement of the detectors, it is possible to separate neutral and charged particles and the belonging calculated dose rates. In this work the particle telescope has been calibrated with several heavy ions, radioactive sources and with neutrons of different energies. Furthermore, measurements onboard aircraft were conducted in order to verify the performance of the telescope in a complex natural radiation field. In order to acquire measurements up to an altitude of 25 km an unmanned balloon flight near the polar circle was conducted. Based on this measurement presented in this work, it is now possible to estimate the radiation exposure up to an altitude of 25 km.

Contents

1. Introduction **1**

2. Radiation Environment in the Earth's Atmosphere **5**

2.1. Cosmic Rays 6

2.2. Development of the Radiation Field in the Earth's Atmosphere . . 7

2.2.1. Solar Modulation of the Galactic Cosmic Ray Flux 8

2.2.2. Shielding Effect of the Earth's Magnetic Field 9

2.2.3. Production of Secondary Cosmic Rays 11

3. Dosimetry **17**

3.1. Dosimetric Terms 17

3.2. Dosimetry in the Atmosphere 20

4. Interaction With Matter **23**

4.1. Charged Particles 23

4.2. Neutrons 24

4.2.1. Elastic Scattering 25

4.2.2. Compound Nuclear Reaction 26

4.3. Photons 27

4.3.1. Photoelectric Effect 28

4.3.2. Compton Effect 28

4.3.3. Pair Production 29

5. The Flight Radiation Environment Detector (FRED) **31**

5.1. Mechanical Design 31

5.2. Electronical Design 32

5.3. Sensor Head 34

5.4. Calibration 35
5.4.1. Charged Particles 35
5.4.2. Neutral Particles 41

6. Measurements and Results **53**
6.1. Measurement Onboard an Aircraft 53
6.1.1. The Measurement Flight From Tokio to Frankfurt 53
6.1.2. The Measurement Flight From Frankfurt to Johannesburg 55
6.1.3. Results From Aircraft Measurements 57
6.2. Measurement Onboard a Stratospheric Balloon 63
6.2.1. Analysis of the Count Rates 68
6.2.2. The Altitude Dependence of the Dose Rate in Silicon . . . 78
6.2.3. The Mean Quality Factor and the Dose Equivalent Rate . 80

7. Conclusion **87**

A. Data Sheet of FRED **101**

B. Calibration Curves and Values **103**

C. Performance Mesurements **111**

List of Acronyms

ADC	Analogue Digital Converter	32
BEXUS	Balloon-borne Experiments for University Students	63
CAD	Computer-Aided Design	32
CMEs	Coronal Mass Ejections	9
CSA	Charge Sensitive Amplifier	32
DOSTEL	Dosimetry Telescope	60
EPP	Expanded Polypropylene	64
FL	Flight Level	21
FPGA	Field Programmable Gate Array	32
FRED	Flight Radiation Environment Detector	2
GCR	Galactic Cosmic Rays	5
GPS	Global Positioning System	70
HIMAC	Heavy Ion Medical Accelerator in Chiba	35
ICRP	International Commission of Radiation Protection	18
ICRU	International Commission of Radiation Units and Measurements	18
IGRF	International Geomagnetic Reference Field	10
ISS	International Space Station	83
LET	Linear Energy Transfer	18
NASA	National Aeronautics and Space Administration	1
PCBs	Printed Circuit Boards	32
PHA	Pulse Height Analysis	33
PE	Polyethylene	111
PTB	Physikalisch-Technische Bundesanstalt	41
SEM	Standard Error of the Mean	37
SRIM	Stopping and Range of Ions in Matter	37
TEPC	Tissue Equivalent Proportional Counter	22
UDP	User Datagram Protocol	33

1. Introduction

Humans are constantly exposed to natural radiation. This radiation consists of the terrestrial radiation and cosmic rays which originate from outer space. The terrestrial radiation stems from radionuclides in the Earth's crust. Ionizing radiation can be harmful because it can damage DNA. Even though the human body is able to repair these damages, errors can occur during the repair processes which can lead to further harmful effects like e.g. cancer. The probability of such defects depends on the intensity of the radiation. It is distinguished between deterministic and stochastic radiation damage. Short time radiation exposure, above a certain threshold results in a deterministic radiation damage. For most deterministic radiation damages, like e.g. redness of the skin, hair loss or anemia, this threshold is 500 mSv. Below this threshold no acute radiation damage occurs but subsequent stochastic radiation damage, like e.g. leukaemia, cancer or eye cataracts, cannot be excluded.

The natural radiation on ground is normally not harmful, however, an air crew in addition is exposed to the radiation field of the atmosphere. Because of this it is important to monitor the radiation level in higher altitudes of the atmosphere. The radiation field at normal cruising altitudes between 9 and 12 km is well known because there were many investigations and measurement campaigns in the last 50 years, see e.g.[*Schrewe*, 2000] or [*Wissmann*, 2006]. Furthermore, the radiation exposure of astronauts at the International Space Station (ISS) is also monitored. Nevertheless, for altitudes around and above 20 km only very few measurements have been performed up to now.

Figure 1.1 shows typical values for the radiation exposure in several altitudes. This work shows a measurement of the radiation exposure for high altitude flights. This is of importance because the industry is developing a new generation of supersonic aircraft with operation altitudes above 20 km. Figure 1.2 shows a National Aeronautics and Space Administration (NASA) and Lookheed Martin case study of such supersonic aircraft. Furthermore, space tourism will

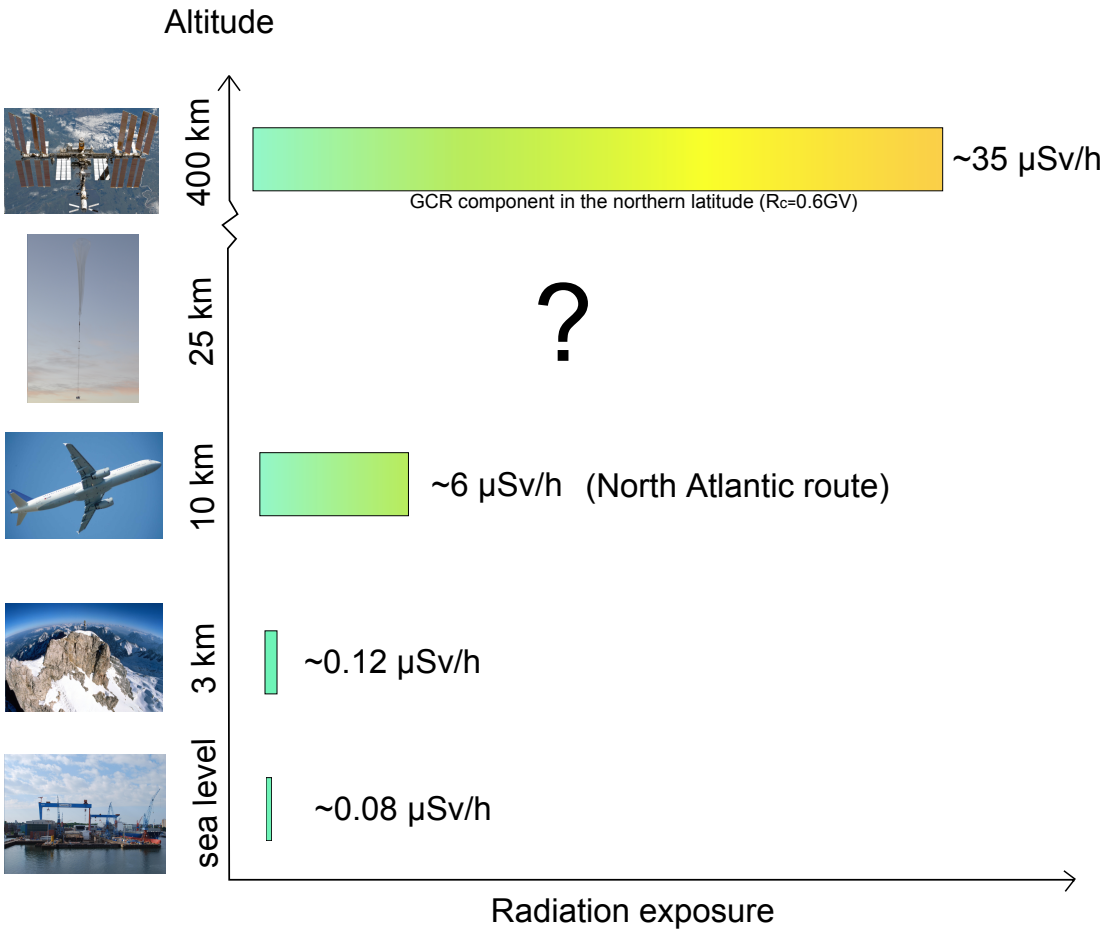

Figure 1.1.: The natural radiation exposure in several altitudes.

get more important in the near future, with several companies aiming to provide low Earth orbit flights. One of the most prominent examples is Virgin Galactic which plans space flights up to an altitude of 110 km. Another example is the manned balloon flights for space tourism. These examples emphasize the importance of high-altitude radiation monitoring as introduced in this thesis. Based on a balloon flight measurement near the polar circle this work will estimate the radiation exposure for stratospheric flights. For this investigation the Flight Radiation Environment Detector (FRED), a very small and light-weight particle telescope based on silicon semiconductor detectors, has been developed. For the characterization of FRED several calibration measurements in different radiation fields were conducted because these measurements are important for the interpretation of the measurements in unknown radiation fields. Furthermore, for

verification of FRED in a mixed radiation field measurements onboard an aircraft have been performed.

Figure 1.2.: A case study from the NASA and Lookheed Martin for a supersonic aircraft. Image credit:NASA[1].

Stucture of the Work

Chapter 2 gives an overview of the radiation field in the Earth's atmosphere. Here various influences and the development of the natural radiation field will be described. In chapter 3 the important dosimetric quantities are introduced. Furthermore, typical radiation protection values for the common cruising altitude are shown. Subsequently chapter 4 gives a brief overview of the physical interaction processes of particle radiation with matter followed by the introduction of the FRED instrument (see chapter 5), where design and the working principle of the detector is shown. Furthermore, the calibration measurements with several charged particles and neutrons are presented. Chapter 6 builds the main part of the thesis, showing the measurement in the Earth's atmosphere. At first the measurement and results onboard an aircraft are shown because this mixed radi-

[1] http://www.nasa.gov/multimedia/imagegallery/image_feature_1698.html

ation field is well known and can be used as a performance test. The second part shows the measurement and results onboard the stratospheric balloon. Finally chapter 7 summarizes the important results of the thesis and gives an outlook for future investigation.

Note, parts of the detector description in chapter 5 and especially the charged particle calibration in chapter 5.4.1 have been submitted to the proceeding of 33rd International Cosmic Ray Conference in Brazil, 2013. Furthermore, parts of chapter 6.2.1 have been submitted to the proceedings of the 21st Symposium on European Rocket and Balloon Programme and Related Research in Switzerland, 2013.

2. Radiation Environment in the Earth's Atmosphere

The Earth is permanently exposed to energetic particle radiation from deep space. This phenomenon was discovered by Viktor Hess in 1912 [*Hess*, 1912]. At that time the natural radioactivity was known but one thought that the origin of measured ionizing radiation were radioactive nuclei in the Earth's crust. Motivated by measurements conducted by the German physicists Theodor Wulf (1868-1946) and Karl Bergwitz (1875-1958), Hess performed manned balloon flights up to an altitude of 5350 m. He measured with several electrometers that the intensity of the radiation increased with the altitude. He concluded that there was an additional radiation which impinged the Earth from space. He called it "Höhenstrahlung", which nowadays is known to consist of Galactic Cosmic Rays (GCR) and secondary cosmic rays produced in the atmosphere. In this chapter an explanation of how the radiation field in the Earth's atmosphere evolves from the cosmic rays is given.

Figure 2.1.: Viktor Hess in his balloon[1].

[1] http://en.wikipedia.org/wiki/File:Hessballon.jpg

2.1. Cosmic Rays

GCRs originate from outside our heliosphere and have their origin in the star evolution within our galaxy, like e.g. in supernova remnants [*Büsching et al.*, 2005]. They enter the heliosphere isotropically and constant in time. The GCRs consist of 98% nuclei and 2% electrons whereby the nuclei are composed of 87% protons, 12% helium ions and 1% heavy ions [*Simpson*, 1983]. The left graph in figure 2.2 shows an energy spectrum for the different species of GCR. Most of

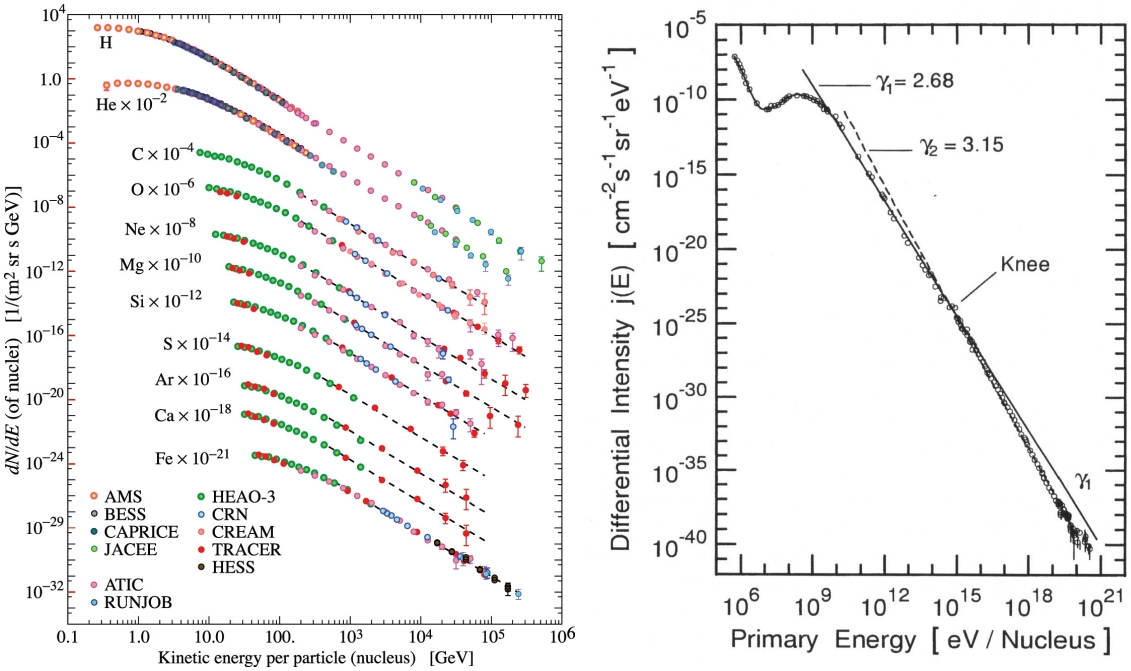

Figure 2.2.: On the left side one can see an energy spectrum and composition[2] of the GCR [*Beringer, J. et al. (Particle Data Group)*, 2012] and the graph on the right side shows an energy spectrum[3] of the GCR flux. One can see that the flux decreases according to a power law above 10^{10} eV [*Grieder*, 2001].

the particles are relativistic and the energy range expands from 10^6 eV up to 10^{20} eV with a maximum of intensity between 10^8 eV and 10^9 eV. On the right graph in figure 2.2 a differential intensity energy spectrum of the GCR flux is displayed.

[2]This figure is accessible via Particle Data Group, http://pdg.lbl.gov.

[3]Reprinted from Cosmic Rays at Earth, P. K.F. Grieder, Copyright (2001), with permission from Elsevier (License number 3234780325601)

Above 10^{10} eV the GCR flux decreases according to a power law $I(E) \propto E^{-\gamma}$ with $\gamma = 2.68$ - 3.15 [*Grieder*, 2001].

2.2. Development of the Radiation Field in the Earth's Atmosphere

The Earth is constantly exposed to GCR particles. Particles with a certain minimum rigidity can enter the atmosphere. Other particles will be deflected by the magnetic field of the Earth due to the Lorenz force. Once a GCR particle enters the atmosphere, it can produce an air shower by nuclear interaction with atmospheric atoms in an altitude between 20 km and 30 km. A complex radiation field arises from the air shower composed of different charged and neutral par-

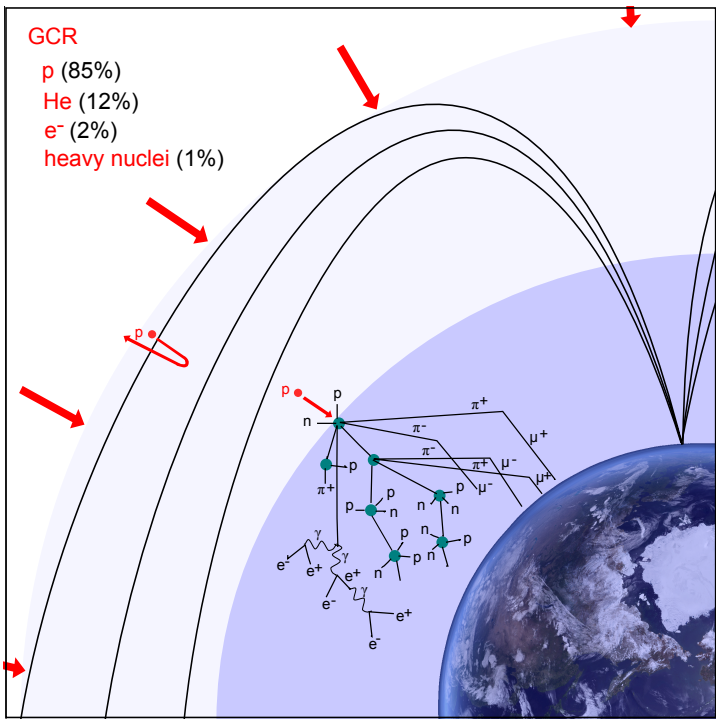

Figure 2.3.: The development of the radiation field in the Earth's atmosphere.

ticles. Using unmanned balloons, in 1935 Pfotzer discovered, that the intensity of the ionizing radiation has a maximum at an altitude of approximately 20 km [*Pfotzer*, 1936], as shown in Figure 2.4. A constant level of GCR intensity reaches the atmosphere and due to the increasing density of the Earth's atmosphere and

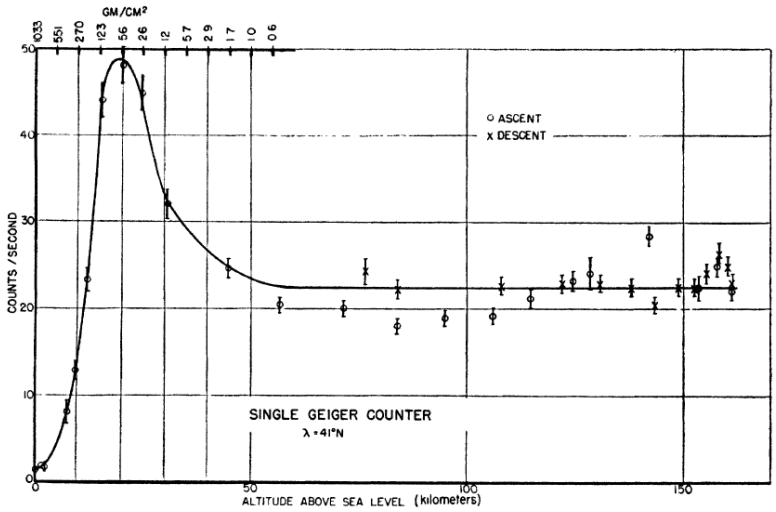

Figure 2.4.: Intensity of charged particles in dependence of the altitude [*Van Allen and Tatel*, 1948] Copyright(1948) by The American Physical Society.

thus an increasing secondary particle production the particle flux increases reaching a maximum at 20 km. Below this so called Pfotzer maximum the absorption increases faster than the production of particles and therefore the particle flux decreases. In the following sections the interaction processes will be described in more detail, starting with the solar modulation on the GCR flux which has a significant influence on the radiation field in the atmosphere.

2.2.1. Solar Modulation of the Galactic Cosmic Ray Flux

A quantity to describe the solar activity is the number of sun spots. They were observed and counted since the development of the telescope in the 17th century. Thereby an eleven year cycle of the sun spot numbers was discovered. Long term measurements of the GCR flux and the sun spot numbers indicate an anticorrelation between the intensity of the GCR flux on Earth and the solar activity. Figure 2.5 shows the monthly mean value of the measured count rates from the Kiel neutron monitor in black and in red the monthly sun spot number. The variation of the neutron monitor count rate is anti-correlated to the eleven year cycle of the sun.
The sun constantly emits electromagnetic radiation and particles. These particles

[4]Kiel neutron monitor data are accessible via Neutron Monitor Data Base, http://www.nmdb.eu and the sunspots number via Solar Influences Data analysis Center, http://sidc.oma.be.

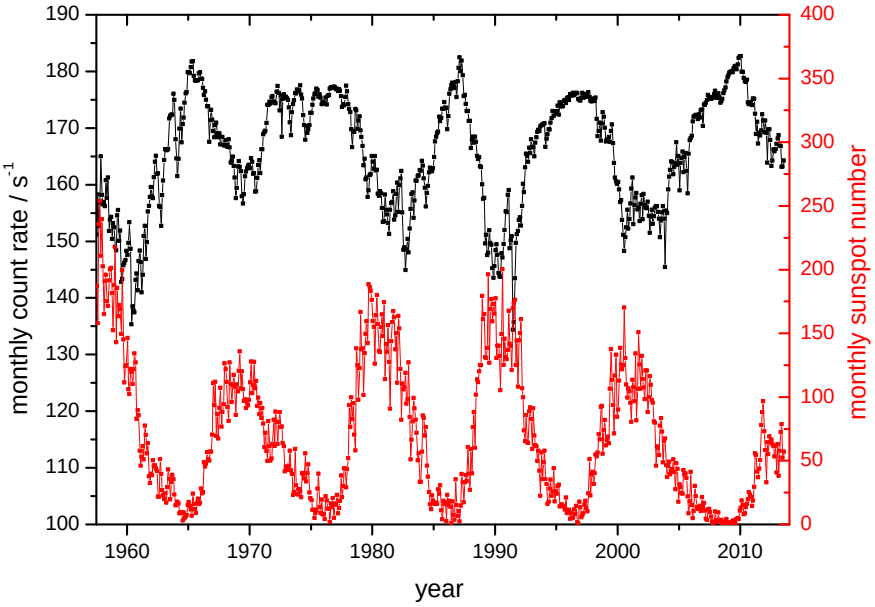

Figure 2.5.: The black curve shows count rates measured by the neutron monitor in Kiel and the red curve shows the monthly sunspot number for the same time period[4].

are mainly protons, electrons and some heavy ions which are called solar wind. The magnetic field of the sun is frozen in the solar wind and builds the so called Parker spiral [*Prölss*, 2004]. With increasing solar activity the number of Coronal Mass Ejections (CMEs) increases. Due to these ejections matter is accelerated so that it can leave the corona of the sun. Thereby the sun can emit X-ray and γ-rays as well as micro and radio waves. The eruptions are located near the sun spots. Furthermore, high energetic particles can be produced, which propagate along the Parker spiral. If the Earth is magnetically connected with the sun these particles can reach the Earth, e.g. a CME with eligible topology and intensity can activate a geomagnetic storm on Earth. In the latter case it can cause technical disturbances on Earth, e.g. it can have an effect on transmission lines, electronics, satellites, or airplanes.

2.2.2. Shielding Effect of the Earth's Magnetic Field

Charged particles of the GCR will be distracted in the Earth's magnetic field due to the Lorentz force. Therefore particles need a minimum rigidity in order to resolve the Lorentz force and to enter the atmosphere. Other particles will be

deflected. The rigidity is defined as momentum per charge. Störmer developed a theory for the motion of charged particles in the magnetic field of the Earth [*Longair*, 1992]. With this theory it is possible to calculate a minimum required rigidity for every location and given direction of arrival in a perfect dipole field without higher moments. Thereby, one can calculate the rigidity for an incident particle that cannot reach the location from the given direction of incidence. This threshold is called cut-off rigidity due to the fact that the spectrum of incident particles is cut off at this point (see figure 2.7). This cut-off rigidity is the minimum rigidity for particles which can enter the atmosphere. For vertical incident particles the following relation is given:

$$R_c = \frac{p \cdot c}{Z \cdot e} = \frac{M}{4 \cdot (R_e)^2} \cos^4(B_m) \tag{2.1}$$

R_c = vertical cut-off rigidity
R_e = Earth's radius
p = momentum of the particle
Z = charge number of the particle
e = elementary charge
c = speed of light
M = dipole moment of the Earth
B_m = geomagnetic latitude

The unit of rigidity is volt or energy per charge.
As seen in figure 2.6 the vertical cut-off rigidity depends on the geomagnetic latitude. The values increase from the poles to the equator. Due to this effect the particle flux is decreasing from the poles to the equator. The cut-off values shown in figure 2.6 were calculated with the simulation code "PLANETOCOSMICS" [*Desorgher et al.*, 2006] using the International Geomagnetic Reference Field (IGRF) 2010 model [*Herbst*, 2012]. Figure 2.7 shows proton energy spectra measured in different cut-off rigidity regions by the satellite experiment PAMELA [*Casolino et al.*, 2008]. The black dots display the primary proton spectrum and the colored dots show measurements in different cut-off rigidity regions. One can see that a larger part of the spectrum is cut off with increasing cut-off rigidity. The particle flux below the cut-off rigidity consists mainly of albedo particles back scatterd by the Earth's atmosphere.

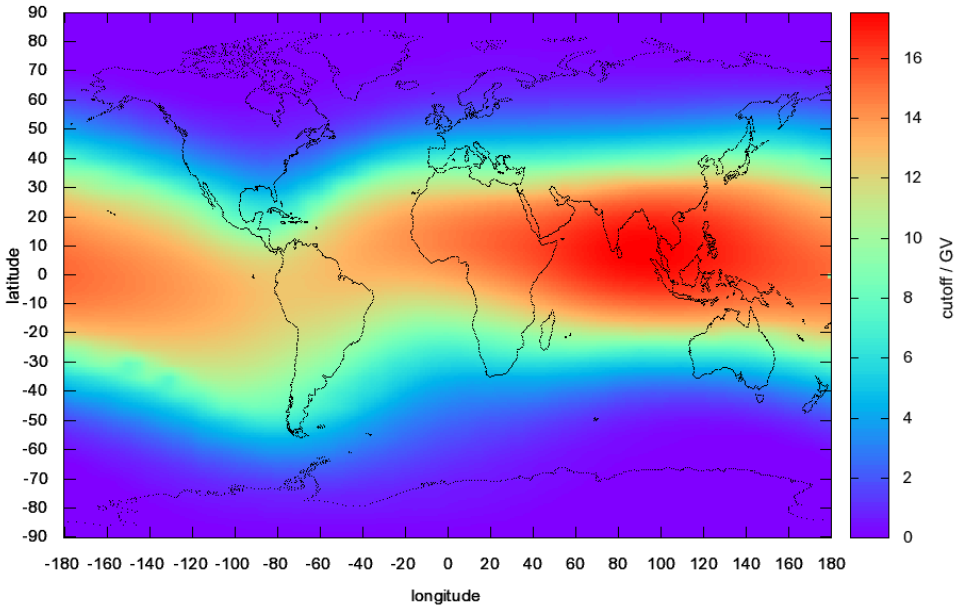

Figure 2.6.: Vertical cut-off rigidity for an altitude of 20 km.

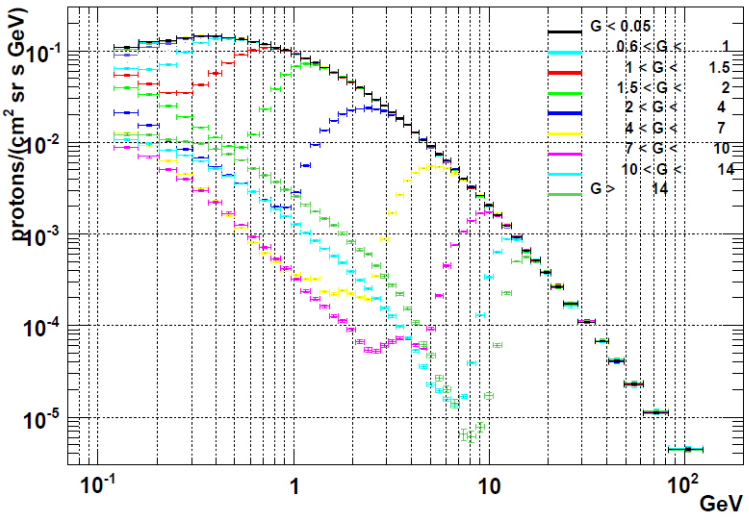

Figure 2.7.: Proton flux measured in different cut-off rigiditiy regions by the satellite experiment PAMELA [*Casolino et al.*, 2008].

2.2.3. Production of Secondary Cosmic Rays

GCRs that are able to enter the atmosphere can create an air shower by nuclear interaction with the atmospheric atoms. During the interaction the primary par-

ticle loses a part of its energy. The particle can activate multiple reactions if the particle energy is sufficient. The first collisions of high energy GCR particles with nitrogen or oxygen atoms are spallogenic reactions which produce secondary particles. These reaction knock fast neutrons and protons out of the target nuclei in the moving direction of the primary particle. After such a reaction the atmospheric atomic nuclei can remain highly stimulated. These nuclei then can emit more neutrons, protons, or fragments of the nuclei for the disexcitation. Figure 2.8 shows the main interaction process of GCR particles with the atmospheric atoms. The heavy ions of the GCRs will be completely fragmented after their

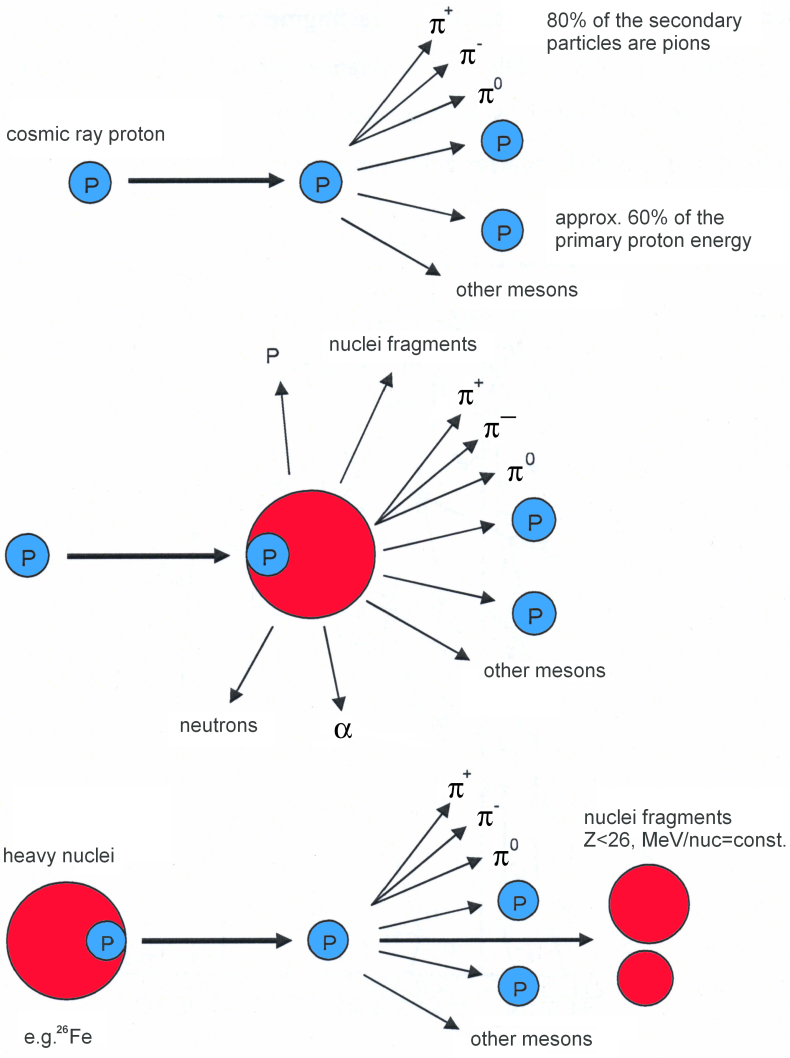

Figure 2.8.: Interaction processes in the Earth's atmosphere adapted from *Von Lany* [2001].

first interaction. Due to their short mean free path this happens in the outer atmospheric layers. The spallogenic reactions produce pions which are mesons with a short lifetime. Therefore, the distance in the atmosphere is short, even though they have relativistic velocity. Due to the short lifetime the probability of a pion decay is higher than the interaction with an atmospheric nucleus. The important decay channels with the typical average life times [*PDG*, 2008] are:

$$\begin{array}{lcll} \pi^+ & \rightarrow & \mu^+ + \nu_\mu & (2,6033 \pm 0,0005) \cdot 10^{-8}\text{s} \\ \pi^- & \rightarrow & \mu^- + \bar{\nu_\mu} & (2,6033 \pm 0,0005) \cdot 10^{-8}\text{s} \\ \pi^0 & \rightarrow & \gamma + \gamma & (8,4 \pm 0,6) \cdot 10^{-17}\text{s} \end{array}$$

π = pion, μ = muon, ν_μ = muonneutrino, $\bar{\nu_\mu}$ = muonantineutrino, γ = gamma quant.

For the consideration of the air shower the neutrinos and antineutrinos will not be considered because they very rarely interact with matter. Neutral pions decay into two gamma quants at the point of origin. Thereby an electromagnetic component of the air shower is created and the cascade is generated onward via pair production and bremsstrahlung. This produces electrons, positrons, and further gamma quants. In the course of the air shower the number of particles for the electromagnetic component increases, but the mean energy of the particles decreases. Once the energy decreases below 1.022 MeV - the needed energy for pair production - the absorption of the particles dominates and the number of particles will be decimated.
The muons that are produced in the pion decay are not stable but they can reach the surface of the Earth due to their relativistic velocity and their typical life time of $2.2 \cdot 10^{-6}$s. The important decay channels with the typical average life times [*PDG*, 2008] are:

$$\begin{array}{lcll} \mu^+ & \rightarrow & e^+ + \bar{\nu_\mu} + \nu_e & (2,197019 \pm 0,000021) \cdot 10^{-6}\text{s} \\ \mu^- & \rightarrow & e^- + \nu_\mu + \bar{\nu_e} & (2,197019 \pm 0,000021) \cdot 10^{-6}\text{s} \end{array}$$

μ = muon, e^- = electron, e^+ = positron ν_μ = muon neutrino, $\bar{\nu_\mu}$ = muon antineutrino, ν_e = electron neutrino, $\bar{\nu_e}$= electron antineutrino.
Muons also contribute particles to the electromagnetic component as one can see

in the decay channels of the muon. Figure 2.9 shows the development of an air shower produced by a single GCR particle.

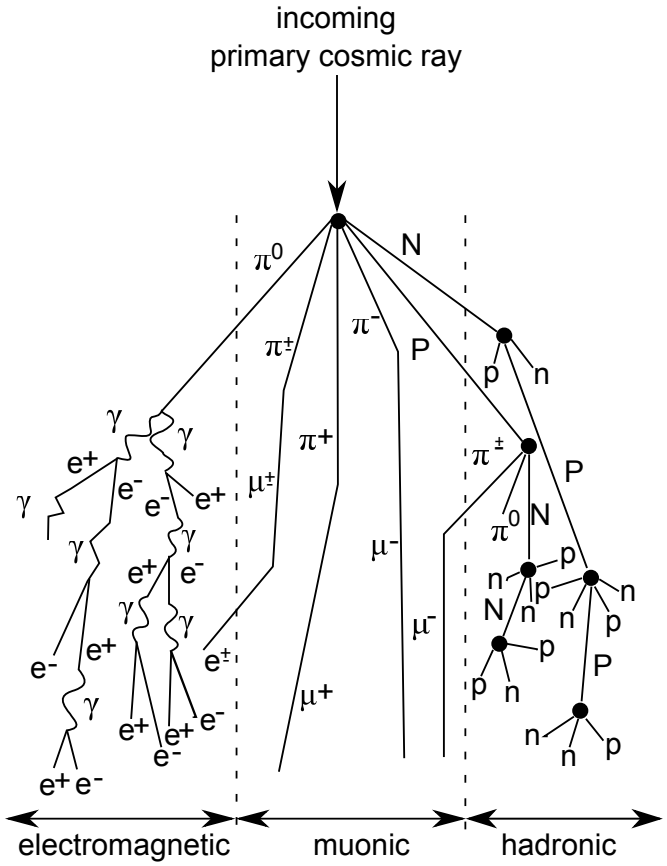

Figure 2.9.: Schematic representation of the development of particle production trough the atmosphere taken from [*Herbst*, 2012], adapted from [*Simpson*, 2000].

In cruising altitudes between 10 and 12 km the GCR particles are completely converted into secondaries consisting of protons, neutrons, electrons, and gamma rays. Due to the shielding effect of the Earth's magnetic field there is a latitude effect of the secondary cosmic rays. In a dedicated altitude the intensity of the secondary cosmic rays will not increase above a certain latitude. The passage in this plateau is called knee, which is located in the range of 50 to 60 degrees northern latitude. It depends on the observed secondary cosmic ray component and the altitude. The reason for the latitude effect and location of the knee is that the effective production by the primary GCR is different for the different secondary components. Stable and quasi stable particles can only reach the observation point if they have enough energy to cross the atmosphere to this point. This

minimum energy is a result of energy loss of the particles in the atmosphere. An additional parameter for unstable particles is the life time. For example, muons can cross the atmosphere due to time dilation but they need to have relativistic kinetic energies. Therefore, for every component and every altitude there is a minimum energy for GCR particles, above which the observed component will be effectively produced. This minimum energy is called atmospheric cut-off. The mean energy is significantly higher for GCR particles that produce muons, due to their lifetime, than for particles that produce corresponding protons. Therefore, the protons show a stronger latitude effect. The explanation for the development of the knee in the latitude effect is that the atmospheric cut-off will be dominated by the production process with decreasing geomagnetic cut-off rigidity. Due to this there is a latitude above which the flux intensity is constant for an observed altitude. The atmospheric cut-off is depending on the altitude above the ground and on the observed secondary cosmic ray component.

3. Dosimetry

Radiation dosimetry deals with the measurement of energy deposition in matter and tissue resulting from the exposure to ionizing radiation. Due to the effect that the human body has no organ of perception for ionizing radiation and that some kind of energy deposition could be harmful for the human body it is important to measure the radiation exposure in specific areas. This chapter will explain the dosimetric terms which are important for this work. Furthermore, the measured dosimetry effects in the atmosphere over the last decades will be shown.

3.1. Dosimetric Terms

Radiation exposure is measured via the interaction of ionizing radiation with a detection material. This results in an energy deposition and therefore, to an energy transfer to the material which can be characterized by the quantity dose. The simplest description of dose is the ion dose I. The ion dose is defined by the ratio of created charge ΔQ and the mass element Δm of the detection material:

$$I = \frac{\Delta Q}{\Delta m} \tag{3.1}$$

The unit is C/kg. The ion dose indicates the number of created free charge carriers in the detection material. With this value and the information on how much energy is needed to create a free charge carrier in the detection material, it is possible to calculate the energy deposition. This calculated term is the absorbed dose D. It is the ratio of energy deposition ΔE and the mass element Δm of the irradiated detection material:

$$D = \frac{\Delta E}{\Delta m} \tag{3.2}$$

The SI-unit is J/kg and the name of this unit is Gray (Gy): 1 Gy = 1 J/kg.
The absorbed dose does not account for the biological effectiveness of the different kinds of ionizing radiation, therefore the absorbed dose is insufficient for

the purpose of radiation protection. For example the biological effectiveness of α-radiation is roughly 20 times higher than for β-radiation of the same absorbed dose because α-radiation creates a higher ionization density on a short range than the electrons of the β-radiation. This is important because for biological tissue a higher ionization density is more harmful [*Laskowski and Pohlit*, 1974].
Due to this effect the International Commission of Radiation Protection (ICRP) and the International Commission of Radiation Units and Measurements (ICRU) established a quantity called quality factor Q which considers the different biological effectiveness of different kinds of radiation. The quality factor depends on the Linear Energy Transfer (LET), which is the energy loss of charged particles owing to collisions with electrons divided by the path length (dE/dx). The typical unit for LET is keV/μm in biological tissue or in water respectively. The quality factor from the ICRP is given in eq. 3.3, while figure 3.1 shows the trend of the quality factor depending on the LET.

$$Q(LET) = \begin{cases} 1 & \text{for } LET < 10 \text{ keV} \cdot \mu m^{-1} \\ 0.32 \cdot LET - 2.2 & \text{for } 10 \text{ keV} \cdot \mu m^{-1} \geq LET \leq 100 \text{ keV} \cdot \mu m^{-1} \\ 300/\sqrt{LET} & \text{for } LET > 100 \text{ keV} \cdot \mu m^{-1} \end{cases} \tag{3.3}$$

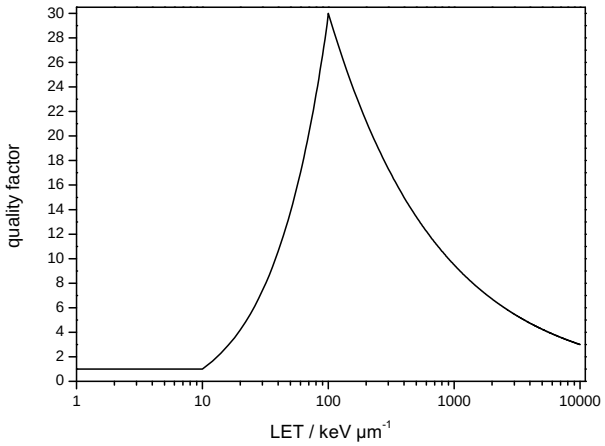

Figure 3.1.: The quality factor in dependence of the LET according to ICRP-60 [*ICRP*, 1991].

For example, the quality factor of photons is energy-independent equal to 1 because of the low ionization density produced by photons leading to an LET of

less than 10 keV/μm. The multiplication of absorbed dose D with the quality factor Q gives the dose equivalent H.

$$H = Q \cdot D = \int Q(LET)\ D_{LET}\ dLET \tag{3.4}$$

The dose equivalent H has the same unit as the absorbed dose D [J/kg] because the quality factor is dimensionless. For clarification that the dose equivalent considers the biological effectiveness the unit Sievert (Sv) is used here. A further quantity, used in radiation protection is the effective dose E which includes the different sensibilities of the several organs to different kinds of radiation, whereas the dose equivalent considers only the effectiveness of the different kinds of radiation. The definition of the effective dose E is:

$$E = \sum_T w_T \cdot H_T = \sum_T w_T \sum_R w_R \cdot D_{T,R} \tag{3.5}$$

where $D_{T,R}$ is the mean absorbed dose in the specific organ T and w_R the radiation weighting factor for the radiation type R (see table 3.1). The sum over R gives H_T, the equivalent organ dose for the specific organ T. Taking into account of the organ weighting factor w_T the sum over all organs is the quantity effective dose which is not measurable. For example the organ weighting factor for gonad is 0.2, for the lung 0.12 and for skin 0.01 [*StrlSchV*, 2001]. The sum over all organ weightings factor is 1.

Table 3.1.: The radiation weighting factor according to ICRP-60 *ICRP* [1991]

Radiation type		Radiation weighting factor w_R
photons		1
electrons,Myon		1
neutrons	$E_{kin} < 10$ keV	5
	10 keV $< E_{kin} <$100 keV	10
	100 kev $< E_{kin} <$ 2 MeV	20
	2 MeV $E_{kin} <$ 20 MeV	10
	20 MeV $< E_{kin}$	5
protons	$E_{kin} >$ 2 MeV	5
heavy ions		20

The term ambient dose equivalent describes a dose measurement in a specific location. This measurement is done in free air and underestimates the dose equivalent

because secondary particles are produced in a human body, this can increase the dose equivalent. Due to this fact the ambient dose equivalent $H^*(10)$ was defined. The ambient dose equivalent is the dose equivalent in a specific location in an aligned and expanded radiation field measured in the depth of 10 mm in the ICRU-sphere in the beam direction. The ICRU-sphere is a spherical phantom composed of ICRU soft part tissue (tissue equivalent material with a density of 1 g/cm^3) and a diameter of 30 cm [*Krieger*, 2002].
In Germany, the maximum accepted values of radiation exposure are defined in the Radiation Control Regulations (RöV) and the Radiation Protection Ordinance (StrlSchV). Operational radiation exposed people are grouped into categories A and B. People with a radiation exposure between 1 mSv and 6 mSv per year are classified in category B. People with a radiation exposure greater than 6 mSv/a and under 20 mSv/a are classified in category A. In exceptional cases with permission the maximal accepted value can be increased to a limit of 50 mSv/a if the radiation exposure will not be greater than 100 mSv in the next 5 years [*StrlSchV*, 2001]. Table 3.2 summarizes the maximum accepted values. Due to the recommendation of the ICRP air crews were classified as radiation workers in the EU Directive EURATOM/29/96.

Table 3.2.: Overview of the maximum accepted values for radiation workers in Germany.

	maximum accepted effective dose
no classification	$<$ 1 mSv/a
radiation worker category B	$<$ 6 mSv/a
radiation worker category A	$<$ 20 mSv/a
radiation worker category A with permission if the exposure will be not greater than 100 mSv in the next 5 years	$<$ 50 mSv/a
career dose	$<$ 400 mSv

3.2. Dosimetry in the Atmosphere

The radiation field in cruising altitudes is well-known due to the fact that air crews are classified as radiation workers and thereby a lot of measurements to monitor the radiation environment were conducted. The typical cruising altitude

of an airplane is in the range between 8 km and 14 km. Usually in aviation a typical altitude declaration is the Flight Level (FL) which is a pressure altitude. For the calculation of a FL the altitude in foot must be divided by 100, e.g. 13.7 km or 45000 ft under standard atmospheric conditions (1013 hPa) corresponds to FL450. For the dosimetry the FL as altitude declaration is useful because a FL is an isobaric plane. That means a FL has a constant shielding trough the residual atmosphere. The complex radiation field in cruising altitudes is mainly composed of secondary particles. Due to their biological effectiveness neutrons add 30 % to 70 % to the dose equivalent in cruising altitudes [*Strahlenschutzkommission*, 1997]. A report of the Commission on Radiological Protection describes that the ambient dose equivalent is an adequate approximation for the effective dose of the air crew because the effective dose can not be measured. Therefore the ambient dose equivalent is measured and the effective dose is calculated by a computer program for the radiation protection register [*Strahlenschutzkommission*, 1997]. Figure 3.2 shows measurements with a silicon detector during solar minimum conditions. On the left side the absorbed dose rate in silicon for several flight levels and cut-off rigidities is shown. The figure on the right side displays the same

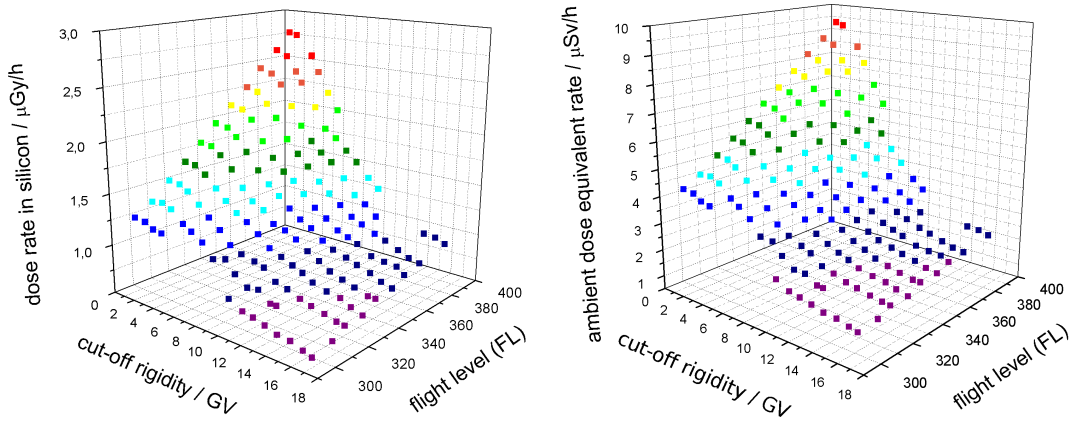

Figure 3.2.: The absorbed dose rate in silicon measured with NAVIDOS during solar minimum conditions (2009 to 2010) (left side). On the right side the same measurement converted into an ambient dose equivalent is shown [*Möller et al.*, 2010].

measurement converted into an ambient dose equivalent. For the conversion of the absorbed dose into an ambient dose equivalent rate the calibration function

[*Möller*, 2008] was used which depends on the cutoff rigidity. The calibration function ranges between 3.35 near the poles and 2.4 near the equator. The figure also demonstrates the linear increase of the dose rate with increasing altitude for different cut-off rigidity regions and the latitude effect of the dose rate. Due to the stronger shielding effect of the magnetic field the dose rate decreases to the equator (high cut-off rigidity values) because the production of secondary particles decreases, especially the production of neutrons. Therefore the latitude effect is stronger for the ambient dose equivalent. A further measurement is shown in figure 3.3 [*Schrewe*, 2000]. This measurement was taken with a Tissue Equivalent

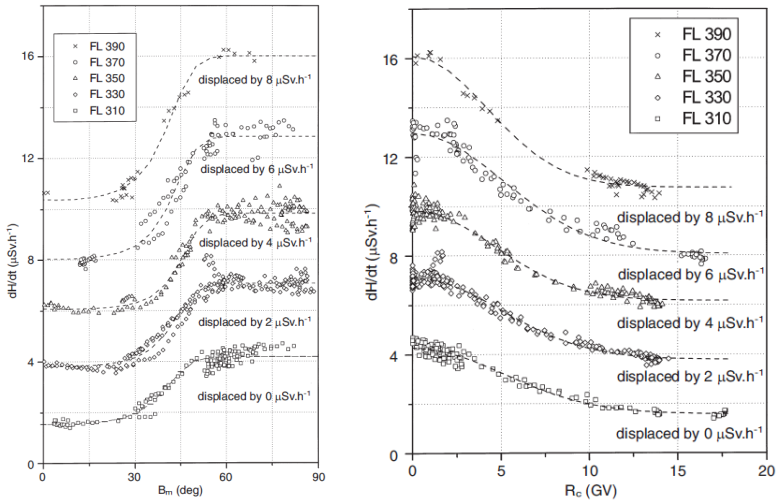

Figure 3.3.: The ambient dose equivalent rate in cruising altitudes measured between 1997 and 1999. The left panel shows the measured ambient dose equivalent depending on the magnetic latitude and the right panel shows the same measured values depending on the cut-off rigidity [*Schrewe*, 2000], by permission of Oxford University Press (License Number 3234780173783).

Proportional Counter (TEPC) in the time period from 1997 to 1999. The left figure shows the measured ambient dose equivalent depending on the magnetic latitude. One can see the latitude effect of the dose rate. In the polar region ($B_m > 60°$) and in the equator region ($B_m < 30°$) the ambient dose equivalent is on a constant level. The ambient dose equivalent rate level is higher in the polar region and it decreases to the equator region. This behavior is shown for different flight levels. The right plot shows the same measured values depending on the cut-off rigidity, showing the same plateau-like structure.

4. Interaction With Matter

This chapter describes several physical interaction processes of charged and neutral particles with matter. In particular, interactions with silicon will be discussed as the detection material of the detector used in this work is silicon

4.1. Charged Particles

A penetrating charged particle will lose its energy along its particle trajectory in matter due to the coulomb interaction with the atomic electrons. The result of this interaction is an excitation or ionization of the atoms. The Bethe-Bloch-equation describes the mean energy loss per path length:

$$-\frac{dE}{dx} = \frac{z^2 e^4 n_e}{4\pi\epsilon_0 v^2 m_e}\left(\ln\left(\frac{2m_e v^2}{I}\right) - ln(1-\beta^2) - \beta^2\right) \tag{4.1}$$

z = charge number of the particle
v = velocity
n_e = electron density
I = mean ionization potential
$\beta = \frac{v}{c}$

This equation is not depending on the mass of the particle but it depends on charge and velocity. In non-relativistic case ($\beta \ll 1$) the equation can be simplified:

$$-\frac{dE}{dx} \propto \frac{z^2}{v^2} \tag{4.2}$$

and the energy loss then decreases with $\frac{1}{v^2}$. If the particle velocity increases the interaction time decreases, therefore the interaction probability gets smaller. The energy loss minimum is located in the range of double to triple of the particle rest energy. If the particle velocity reaches approximately the speed of light ($\beta \to 1$) the relevance of the logarithmic term increases and the energy loss

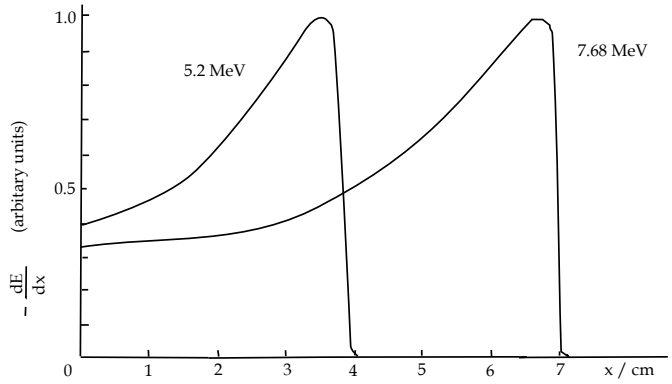

Figure 4.1.: The Bragg-Peak for the energy loss of alpha particles in air of different energy. Adapted from [*Musiol et al.*, 1992]

curve rises slightly. Due to the small interaction time of relativistic particles, their energy loss in matter is small. Therefore relativistic particles are termed minimum ionizing particles.
Furthermore, the range R of the particles in matter can be calculated by the Bethe-Bloch-equation with the following definition [*Pauls*, 1998]:

$$R = \int \frac{1}{\frac{dE}{dx}} dE \tag{4.3}$$

Every particle has a specified range in matter because during the interaction it transfers energy whereby its velocity decreases. Due to this it can produce several ion pairs per path length. If the detector thickness is sufficient particles can be stopped in the detection volume. The energy loss has a maximum near the end of the particle's range in matter, a phenomenon called Bragg-Peak. Figure 4.1 shows the Bragg-Peak for alpha particles with different energies in air.

4.2. Neutrons

Due to the fact that neutrons have no charge, they cannot interact with the electrons of the atomic shell by coulomb interaction. They interact with the atomic nucleus via strong interaction. For fast neutrons ($E_{kin} \gg 0.5$ MeV) between two essential reaction mechanisms are distinguished [*Hertz*, 1961]:

1. the elastic scattering of the neutrons at the target nucleus and

2. the compound nucleus reaction with absorption of the neutron and the two special cases: the inelastic scattering and the resonance scattering.

The probability of such a reaction is described by the cross section σ. A general definition of the cross section is:

$$\sigma = \left(\frac{N}{t}\right) / \left(\frac{N_{total}}{t \cdot A}\right)$$

with N = number of the interacting particles, N_{total} = total number of incident particles, t = considered time interval and A = considered unit area.
The total cross section σ_{total} is the sum of all specific cross sections. It describes the general probability for an interaction with a target material. The typical unit of the cross section is Barn which has the dimension of an area ($1b = 10^{-28}m^2$) in the SI unit system.

4.2.1. Elastic Scattering

During elastic scattering a neutron is elastically scattered at the nucleus of the target atom. Neutrons lose energy but they still are considered as independent particles. The elastic scattering and the mechanical elastic collision are comparable. According to this the energy transfer ΔE of a neutron to the nucleus depends on the scattering angle ϑ, the mass of the nucleus m_T, the neutron mass m_n, as well as the neutron energy E_n. The following equation describes the energy transfer:

$$\Delta E = \frac{4 \cdot (m_T \cdot m_n)}{(m_T + m_n)^2} \cdot \cos^2 \vartheta \cdot E_n \tag{4.4}$$

For the maximum of the energy transfer $\vartheta = 0$ (central collision) this equation can be simplified by using $m_n = 1$ and the target nucleus mass m_T will be specified in multiples of the neutron mass m_n. The result is:

$$\Delta E_{max} = \frac{4 \cdot m_T}{(m_T + 1)^2} \cdot E_n \tag{4.5}$$

This equation shows that neutrons can only transfer up to 13% of their primary energy to a silicon nucleus ($m_T = 28$) by elastic scattering. Furthermore, it clearly describes that the maximum energy transfer ΔE_{max} will be reached by collision partners with the same mass ($m_T = m_n$). Therefore, the interaction between neutrons and hydrogen target nuclei (protons) result in the maximum energy transfer. This explains the importance of neutrons for dosimetry because the human body mass consists of 10% hydrogen.

4.2.2. Compound Nuclear Reaction

An atomic nucleus can absorb a neutron via the compound nuclear reaction. The outcome is a compound nucleus. The model of compound nuclear reaction is based on the liquid drop model, which was developed by Breit and Wigner in 1936. According to the liquid drop model the nuclei act as molecules in an incompressible fluid [*Demtröder*, 2005]. The assumption is that the absorbed energy is uniformly distributed to all nucleons similar to a heat input in a fluid. In this situation of the reaction the compound nucleus is stimulated. According to the conservation of energy the excitation energy is equivalent to the total energy of the absorbed neutron. The probability for a compound nucleus is high if the excitation energy value and the energy level of the compound nucleus is equivalent. A compound nuclear reaction cross section is defined as:

$$\sigma_c = \pi \cdot \left(R + \frac{\lambda}{2\pi}\right)^2 \cdot \frac{4kK}{(K+k)^2} \tag{4.6}$$

with R = radius of the nucleus in cm, λ = the De Broglie relation of the projectile in cm, k = the wave number of the projectile in cm^{-1} and K = the wave number of the nucleus in cm^{-1} [*Stöcker*, 2004].
A resonance in the cross section will be observed if the excitation energy value and energy level of the target nuclei is equivalent. The cross section for heavy nuclei shows a lot of resonance because the nucleus has a lot of energy levels. A possibility for an overlap of the resonance exists and the cross section for high neutron energies can fade to a continuum [*Wirtz and Beckurts*, 1958].
The excited compound nucleus can decay in different output responses independently from the input reaction. The output response is depending on the energy transfer of the incident neutron. If the energy transfer is insufficient to emit again a neutron, this results in bound levels in the term diagram. These excited bound levels decay through the emission of γ-ray photons into the ground state of the atomic nucleus [*Wirtz and Beckurts*, 1958]. At higher energies the nucleus can emit again neutrons, e.g. with the primary neutron energy. This process is called resonance scattering. If neutrons with energies less than the primary energy are emitted by the nucleus, it stays in an excited state which will decay into the ground state under emission of γ-rays. This decay process is called inelastic scattering.
Fast neutrons, which are typical secondary cosmic rays, can also generate charged

particles, mainly protons and alpha particles. Thereby the angular distribution of a compound reaction is isotropic. Figure 4.2 shows the different reaction channels for a compound nuclear reaction in silicon. The main interaction process

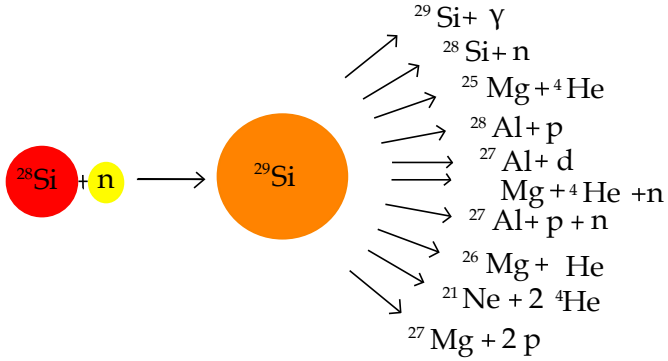

Figure 4.2.: Reaction channels of the compound nuclear reaction with silicon [*Stöcker*, 2004]

for heavy nuclei with neutrons up to 100 MeV is the compound reaction. For neutrons greater than 50 MeV spallation processes are possible and for neutrons greater than 100 MeV these processes prevail.

4.3. Photons

A Photon is an elementary particle of the electromagnetic radiation. They can be described as electromagnetic waves or as particles. Important for this work is the ionizing part of the electromagnetic radiation, in particular the γ - and X-rays. γ- and X-rays overlap in the energy range but their origin is different. X-rays are emitted by specific transitions in the atomic shell or as bremsstrahlung and γ-rays by transitions in the nuclei. The definition of an upper and lower limit for γ-rays is not exact. Therefore, a random lower limit of 10 keV has been defined [*Musiol et al.*, 1992]. For X-rays the energy range is defined as 1 keV to 400 keV. The principle interaction processes for photons with matter are:

- photoelectric effect
- compton effect
- pair production

A more detailed description of these three processes can be found in the following subsections.

4.3.1. Photoelectric Effect

The incident photon energy is absorbed by an electron from the electron shell of the target atom. This electron will be excited or emitted from the shell if the absorbed photon energy is greater than the electron binding energy E_B. The kinetic energy of the electron is $E_{kin} = h \cdot v - E_B$. This process will mainly occur at low photon energies. The definition of the cross section for the photoelectric effect is:

$$\sigma_{Photo} \propto \frac{Z^\alpha}{E_\gamma^3} \tag{4.7}$$

with Z = atomic number of the target material, E_γ = incident photon energy and $\alpha \in \{R|4 \leq \alpha \leq 5\}$
In the spectrum the photoelectric effect is visible as a line with the whole energy of the photon.

4.3.2. Compton Effect

The Compton effect is an elastic scattering of photons by a quasi-free shell electron of the target material. Depending on the scattering angle ϑ the photon loses a part of its energy by wavelength shift. The energy of the scattered photon E'_γ can be described with the following equation [*Knoll*, 2000]:

$$E'_\gamma = \frac{E_\gamma}{1 + (E_\gamma/0.511) \cdot (1 - \cos\vartheta)} \tag{4.8}$$

with E_γ = energy of the incident photon, 0.511 MeV = rest energy of the electron and ϑ = scattering angle of the photon.
This equation shows that the maximum energy transfer will be released by backscattering ($\vartheta = \pi$). In the spectrum an energy continuum from the origin up to the compton edge is visible. This edge is characteristic for the maximum of the transferred energy and it can be calculated with:

$$E_{c,max} = \frac{2 \cdot E_\gamma^2}{2 \cdot E_\gamma + 0.511\text{MeV}} \tag{4.9}$$

In this equation E_γ is the energy of the incident photon in MeV [*Musiol et al.*, 1992].

The compton effect will mainly occur at medium photon-energies and the cross section is proportional to the atomic number Z of the target material per energy of the incident photon E_γ [*Allkofer*, 1971].

$$\sigma_{Compton} \propto \frac{Z}{E_\gamma} \tag{4.10}$$

4.3.3. Pair Production

Pair production describes the interaction between a photon and an electrical field of the nucleus or the electron shell of an atom. In this process an electron-positron pair will be produced. For this reaction the incident photon needs at least double the value of the rest energy of an electron (1.022 MeV). Additional energy will be transferred into the kinetic energy of the electron or positron. Electrons and positrons decelerate fully independently by multiple scattering. At any time the positron can catch an electron from the direct environment. By the annihilation process two γ-quants, each with 0.511 MeV, are created. If both photons exit the detection volume the double escape peak becomes visible in the γ-ray spectrum. The energy of the double escape peak is 1.022 MeV less than the full energy peak (photo-peak). If only one photon is exiting the detector than the single escape peak is visible. The position in the spectrum is shifted by 0.511 MeV [*Knoll*, 2000]. Figure 4.3 shows an ideal γ-spectrum which was created by all described interaction processes.

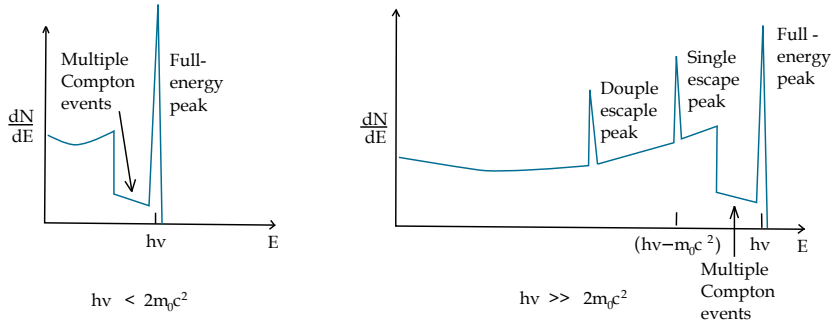

Figure 4.3.: An ideal γ-spectrum[1] for a detector, on the left side a spectrum for a photon energy less than 1.022 MeV and on the right side for greater than 1.022 MeV adapted from *Knoll* [2000].

[1] This material is reproduced with permission of John Wiley & Sons, Inc.

The cross section is proportional to the atomic number Z and the incident photon-energy E_γ.

$$\sigma_{pair} \propto Z^2 \cdot \ln E_\gamma \tag{4.11}$$

The cross section equation for all interaction processes (4.7, 4.10 and 4.11) increases with high atomic number Z. Due to this a material with high atomic number qualifies as γ-radiation absorber, e.g. lead is a very good shielding material for γ-rays.

5. The Flight Radiation Environment Detector (FRED)

FRED is a particle telescope consisting of four segmented silicon semiconductor detectors which was developed to measure neutral and charged particles. In this chapter the mechanical and the electronical design of FRED will be discussed, and the functionality of the sensor head will be described in detail. Furthermore, the calibration measurements with several charged and neutral particle sources will be explained.

5.1. Mechanical Design

FRED is a small and light-weight particle detector telescope. The height of the housing is 99.5 mm, with a footprint on the plate of 112 mm x 100 mm. Due to the housing being made of magnesium the total mass is just 371 g. Figure 5.1

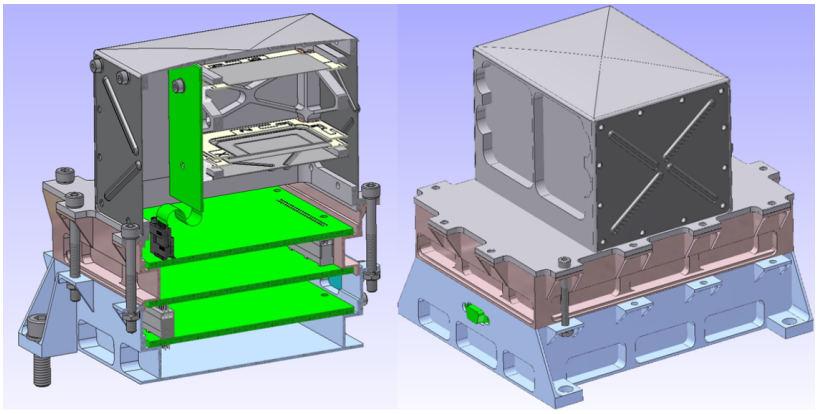

Figure 5.1.: The mechanical design of FRED. The left side shows a cross section of the experiment housing. The PCBs (green) are mounted inside the housing. And on the right side one can see a CAD drawing of the whole instrument [*Möller et al.*, 2013a].

shows a Computer-Aided Design (CAD) drawing of FRED. The Printed Circuit Boards (PCBs) are located in the lower part of the housing and are mounted to it. The four silicon semiconductor detectors are mounted on carrier frames made of AlN 180. These carriers are placed inside an aluminium framework which is mounted to the housing in the upper part. A CAD drawing of the detector stack is shown in figure 5.2.

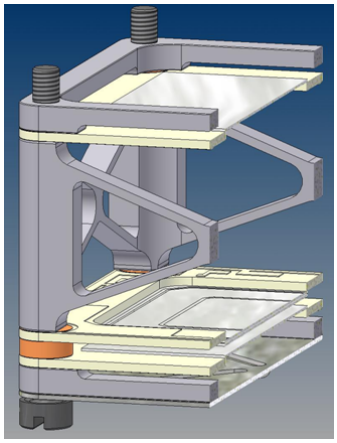

Figure 5.2.: Cross section of the Detector Stack. The detectors (silver) are placed on carriers (yellow). The carriers are mounted on a framework (gray).

5.2. Electronical Design

The experiment FRED mainly consists of three components. These are the Detector Stack, the Irena which is used to handle the data processing and storage, and the Power board. The Detector Stack is connected to the Power board over a filter board. Furthermore, the detector signal circuit is connected via the filter board to the Irena which is made up of two PCBs, the analogue and the digital board. Figure 5.3 shows a schematic drawing of the whole experiment. An incoming particle interacts with the silicon in the Detector Stack. Thereby, free charge carriers are created. The Charge Sensitive Amplifier (CSA) collects and converts them into a voltage pulse. The voltage pulse will be shaped and amplified with two different amplifications and read out by the Analogue Digital Converter (ADC). From that the Field Programmable Gate Array (FPGA) determines the pulse height. If the pulse height is not in the higher detection range of the high gain then the low gain is used. For the analysis of the signal the

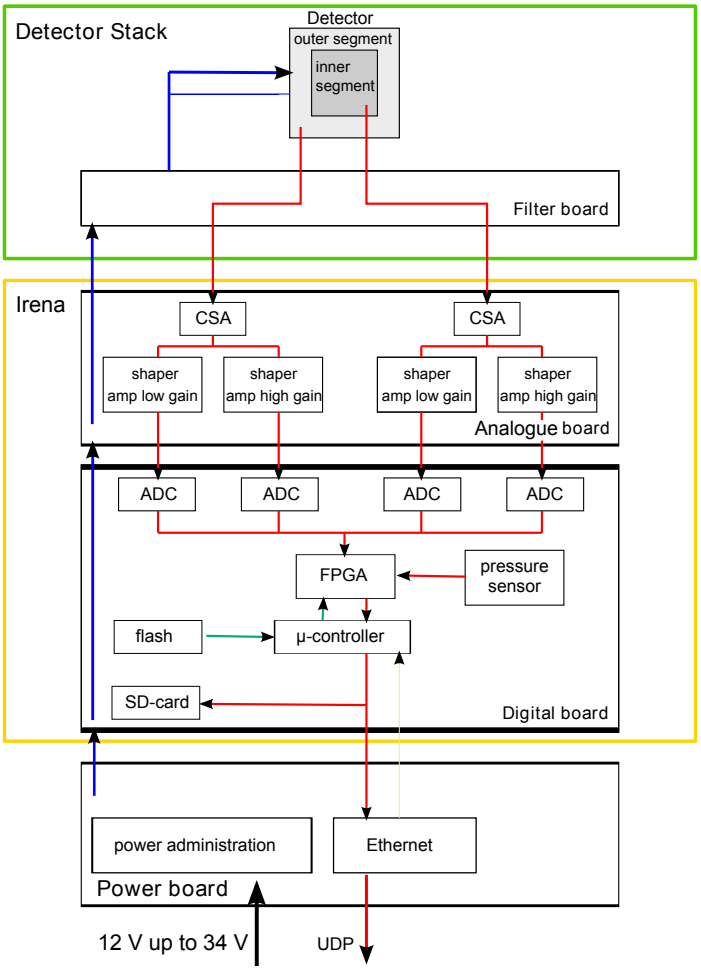

Figure 5.3.: Schematic of the electronics [*Möller et al.*, 2013a].

FPGA samples the ADC with 3 MHz and stores the last 64 ADC values. After every sampling the ADC values are compared with a given pulse shape. For this, 16 defined ADC values are multiplied with 16 defined values of the given pulse shape. The sum of these 16 multiplications is stored after every sample. If this sum has a maximum and a certain height (trigger level) the signal of the ADC is detected as a pulse and a trigger is set. In case of a trigger signal the Pulse Height Analysis (PHA) data for high and low gain of all nine detector segments are sent to the micro-controller. The micro-controller gets the output of the FPGA and stores the PHA data with time stamps on the SD-card. Furthermore, the data are sent from the micro-controller to the ethernet controller per User Datagram Protocol (UDP). The first function of the micro-controller after switch-on is to

load the configuration file from flash into the FPGA. In addition a pressure sensor is located on the Irena board. This pressure sensor was especially developed for the balloon flight campaign. Its function is to stop the writing on the SD card in the descent phase of the balloon when an air pressure of 800hPa is reached. The Power board is connected to a battery pack. This board is creating the -50 V detector bias voltage for the Detector Stack. Furthermore, it manages the different powers for the components. The ethernet connector for the downlink is also situated on this board.

5.3. Sensor Head

The Detector Stack is made up of four segmented silicon semiconductor detectors, which are arranged in a telescope geometry with an opening angle of 120°. The inner segments build a telescope with an opening angle of 60° (see left panel of figure 5.4). Due to this geometry it can determine the LET by using coincidence

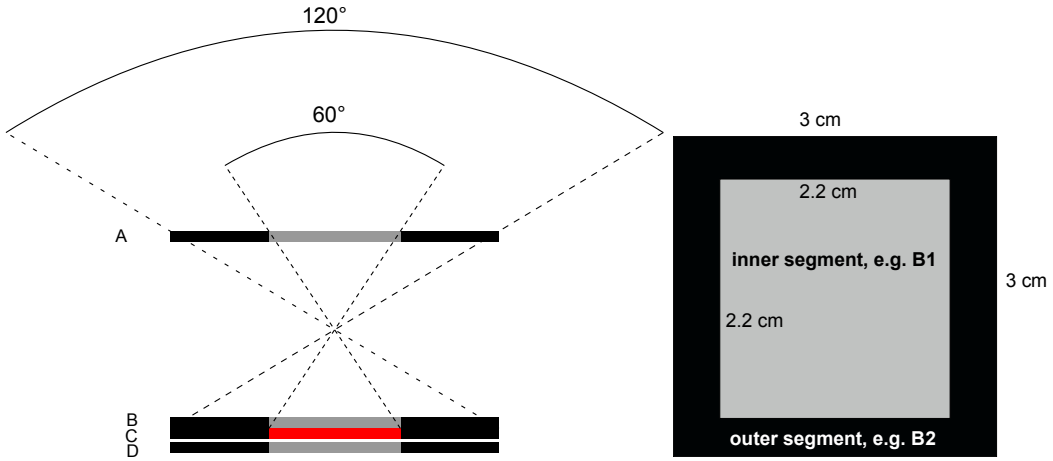

Figure 5.4.: Schematic of the detector arrangement [*Möller et al.*, 2013a] on the left side and a schematic of the detector segments on the right side.

condition, e.g. in detector A and B. From the LET it determines an average quality factor by using the ICRP60-functions [*ICRP*, 1991]. With this average quality factor it is possible to convert the dose in silicon into a dose equivalent which is the commonly used quantity for radiation protection as descripted in chapter 3. Figure 5.4 shows a schematic drawing of the Detector Stack. The detector thickness is 300 µm - for all detectors - and the form is square with a

30 mm edge length. The inner segments of the detectors are also squared with an edge length of 22 mm. Due to an additional guard ring between the inner and outer segment of the C-Detektor the edge length of the inner segment is 21 mm. Detectors B, C, and D are glued together as close as possible (limited by the distances needed for cables), to form a sandwich detector, as the detectors B and D and the outer segment of detector C are used as anticoincidence for the neutral particle channel (red area in figure 5.4), which builds the inner part of detector C.

5.4. Calibration

In this chapter, the different calibration measurements which were conducted with FRED will be shown. The calibration is an important measurement because a calibration function is needed to calculate the energy loss in silicon. For the determination of the calibration function, several measurements with different charged and neutral particles and energies were made.

5.4.1. Charged Particles

As described in section 5.2 FRED has two different gain channels: the low and the high gain. For the determination of the calibration function for these channels and the different detector segments a ^{207}Bi radioactive source and different heavy ions were used. The heavy ion measurements with 100 MeV/nuc helium, 400 MeV/nuc carbon, 400 MeV/nuc oxygen, 600 MeV/nuc silicon and 500 MeV/nuc iron were conducted at the Heavy Ion Medical Accelerator in Chiba (HIMAC), Japan. Figure 5.5 shows the normalized measured heavy ion peaks in the high (left) and low gain (right) channel in the inner segment of the A-detector (A1H), which were used for the calibration purposes. As an example for a calibration measurement Figure 5.6 shows the iron run in the low gain channel of the inner segment of the B-detector because there was the largest beam background. The gray area indicates the used calibration peak. Note that fragmentations of the iron ions, the presence of air molecules and the detector housing form a beam background.
In order to determine the mean energy loss $\langle dE \rangle$ of the ion measurements Landau-Vavilov fit functions (see e.g. [*Leo*, 1987]) were used, as shown in figure 5.7.

Here the carbon 400 MeV/nuc measurement in the inner segment of the A-

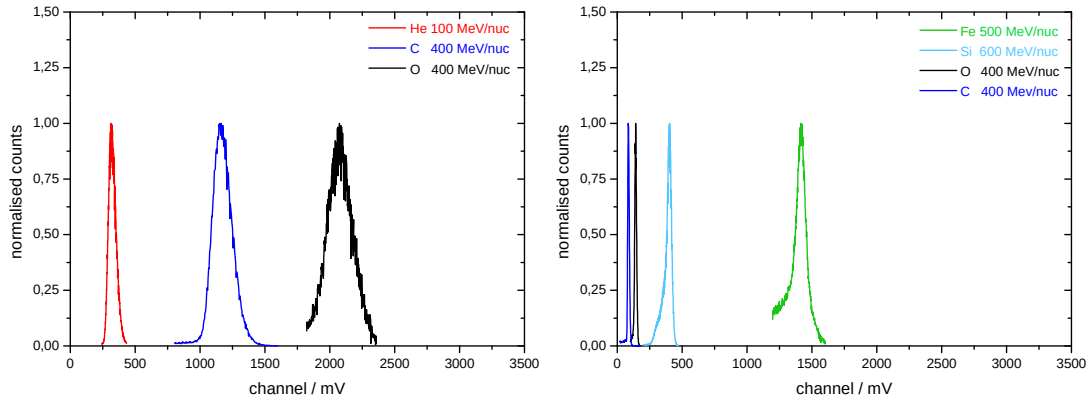

Figure 5.5.: The left panel shows the measured heavy ion peaks in the high gain channel of the inner segment of the A-detector (A1H). The helium peak is given in red, the carbon peak in blue and the oxygen peak in black are shown. The right panel shows the measured heavy ion peaks in the low gain channel of A1H. The carbon peak is given in blue, the oxygen peak in black, silicon peak in light blue and the iron peak in green. Due to fragmentation of the iron ions in the beamline and detector housing it starts not at zero [*Möller et al.*, 2013a] .

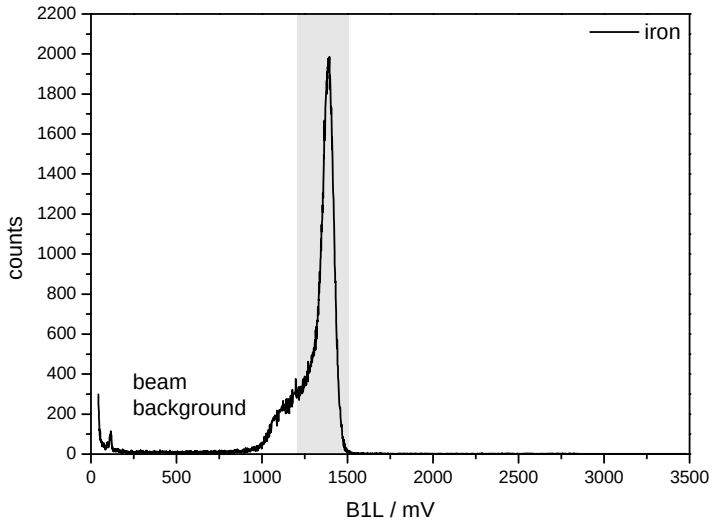

Figure 5.6.: The black curve shows the iron measurement in the low gain channel of the inner segment of the B-detector. The gray area shows the used peak for the calibration.

detector (blue curve) as well as the corresponding Landau-Vavilov fit (red curve) are displayed. This process was done for all detector segments and all heavy ion

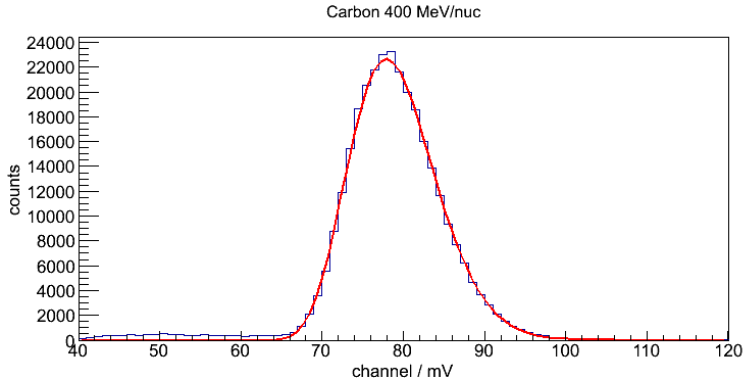

Figure 5.7.: The carbon 400 MeV/nuc measurement (blue) in the low gain channel for the inner segment of the A-detector. The red curve shows the Landau-Vavilov fit [*Möller et al.*, 2013a].

measurements. In addition the fit was used to calculate the standard variation σ This is reasonable because the uncertainty of the mean energy loss is the Standard Error of the Mean (SEM) which is given by:

$$\Delta \langle dE \rangle = \frac{\sigma}{\sqrt{N}}, \tag{5.1}$$

with N the number of total counts of the distribution.

For the calibration purposes the energy loss in silicon of the heavy ions was calculated with the software Stopping and Range of Ions in Matter (SRIM) [*Ziegler*, 2004]. Figure 5.8 shows the calibration values for the inner segment of the A-Detector (A1) which were measured with charged particle beams. On the left side the result of the high gain and on the right side of the low gain mode (black dots on the blue curve) calibration are shown. In addition the right panel shows a comparison of both calibrations. Note that the error bars of the calibration values can not be seen because they are too small. Also shown are calibration functions determined by a linear fit of the form f(x)=$S \cdot x$ where S denotes the calibration factor. In table 5.1 the results of the calibration factors for all detector segments and the two gain levels are shown. Due to the linearity relation between energy loss and mV-channels the slope of the calibration function describes the bin width of the mV-channels. As an additional information the gain factor V between high and low gain is shown in table 5.1. This shows that the low gain

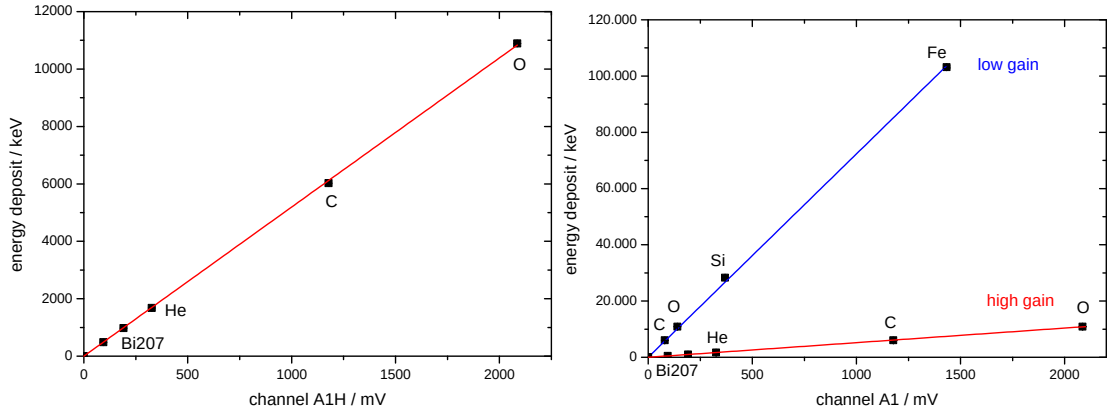

Figure 5.8.: Calibration curve for the high gain of the inner segment of the A-detector (A1H) on the left side (red curve) and the calibration curve for the same detector segment but for the low gain channel (A1L) on the right side (blue curve). Furthermore, one can see a comparison of the two calibration curves [*Möller et al.*, 2013a].

Table 5.1.: Calibration values [*Möller et al.*, 2013a]

Detector segment	high gain / $\frac{keV}{mV}$	low gain / $\frac{keV}{mV}$	gain factor V
A1	5.19 ± 0.02	72.32 ± 0.02	13.93
A2	5.26 ± 0.01	73.23 ± 0.02	13.92
B1	5.25 ± 0.02	73.84 ± 0.02	14.06
B2	5.24 ± 0.02	77.46 ± 0.02	14.78
C1	5.00 ± 0.02	70.50 ± 0.02	14.10
C2	4.90 ± 0.01	71.11 ± 0.02	14.51
D1	5.08 ± 0.03	70.01 ± 0.02	13.78
D2	5.03 ± 0.01	66.86 ± 0.02	13.29

channel bin is ∼14 times bigger than the one of the high gain. The high and low gain trigger threshold are at 15 mV excluding the C1-detector which has the trigger at 12 mV. Due to this information and the calibration values the energy loss range of the different detector segments can be calculated with $dE_H = S \cdot C_i$ (high gain) and $dE_L = S \cdot V \cdot C_i$ (low gain) whereby C_i denotes the channel number is between 12 or 15 up to 3500. In general, FRED can cover energies from 60 keV up to 270 MeV. This is equivalent to a LET range in water from 0.1 up to 429.8 keV/μm. The energy loss ranges for the different detector segments

are summarized in table 5.2. An additional measurement was conducted with a

Table 5.2.: Energy loss ranges for the different detector segments [*Möller et al.*, 2013a]

Detector segment	dE range high gain / MeV	dE range low gain / MeV
A1	0.07785 - 18.165	1.084 - 253.038
A2	0.07890 - 18.410	1.098 - 256.267
B1	0.07875 - 18.375	1.107 - 258.352
B2	0.07860 - 18.340	1.161 - 271.065
C1	0.06000 - 17.500	1.057 - 246.750
C2	0.07350 - 17.150	1.066 - 248.846
D1	0.07620 - 17.780	1.050 - 245.008
D2	0.07545 - 17.605	1.002 - 233.970

^{207}Bi radioactive source for the high gain channel in order to get more calibration points. Figure 5.9 shows the latter measurement in the high gain channel of the inner segment of detector A. For the calibration only the two designated peaks which originate from the two electron emission lines with the energies 481.7 keV and 975.8 keV were used. The other two peaks in figure 5.9 are double lines which can not be clearly distinguished from each other. The calibration points are also shown in Fig. 5.8 as the first two points on the high gain slope. To

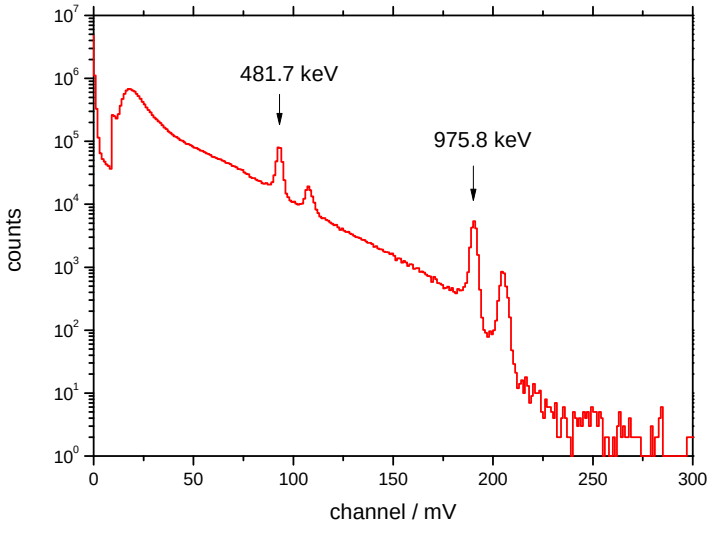

Figure 5.9.: The measured signal in the high gain of the inner segment of detector A with a ^{207}Bi radioactive source.

determine these calibration points from the electron measurements, it was used an intercalibration method between the different detector segments. Figure 5.10 shows a 2D histogram of the inner segments of the A- and B-detector (high gain). The x-axis displays the signals in the A-detector and the y-axis the signals in the

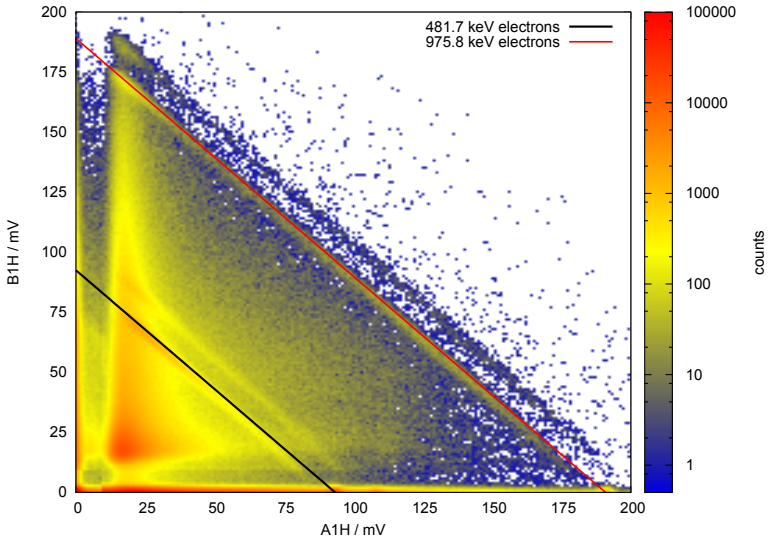

Figure 5.10.: The intercalibration of the inner segments of the A- and B-detector (high gain) with a ^{207}Bi radioactive source. The 481.7 keV (black line) and the 975.8 keV (red line) electrons of the source were used for the calibration [*Möller et al.*, 2013a].

B-detector. The electrons (black line) lose their total energy of 481.7 keV in both detector segments and the electrons on the red line also lose their total energy (975.8 keV) in the two segments. The extrapolation of these two lines to the x- and y-axis are the calibration points for the respective detector segment. For the intercalibration of the inner segment of detector C, signals of the inner segments of detector A and B were added. For the calculation of the summed signal it is necessary to convert the mV scale into the energy loss scale. For this conversion the calculated calibration values for the inner segment of the detectors A and B (see Table 5.1) were used. With this it is possible to calculate a 2D histogram with the summed signal of the inner segment of detector A and B versus the inner segment of detector C. The result is shown in figure 5.11. Since some of the electrons stop in the C-detector it is possible to do the same calibration process for the C-detector as for the A- and B-detector. This intercalibration process must be done for all detector segments to get additional calibration points for the

high gains of all detector segments.

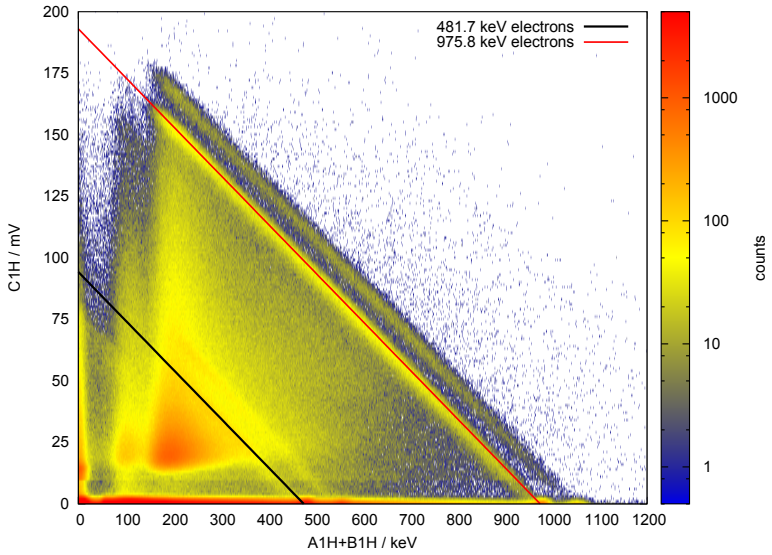

Figure 5.11.: The intercalibration of inner segment of the C-detector (high gain) with a ^{207}Bi radioactive source. The x-axis shows the summed signals (total energy loss) of the A- and B-detector in keV and the y-axis displays the signals in the inner segment of the C-detector in mV. The 481.7 keV (black line) and the 975.8 keV (red line) electrons of the source were used for the calibration [*Möller et al.*, 2013a].

5.4.2. Neutral Particles

For the verification of the neutral channel measurements in the quasi-monoenergetic neutron reference fields at the Physikalisch-Technische Bundesanstalt (PTB) in Braunschweig and at iThemba Labs in Cape Town, South-Africa, were conducted. Furthermore, a measurement with a γ-ray source was performed.

5.4.2.1. Measurements in the low-energy reference fields

The quasi-monoenergetic neutron reference fields between 1.2 MeV and 19 MeV are generated at the PTB accelerator facility. FRED used the reference fields with peak energies of 1.2, 2.5, 5, 8, 14.8 and 19 MeV. These fields are defined in the ISO 8592 standard. For the production of these reference fields the PTB used the D(d,n), T(p,n) and the T(d,n) target reactions [*Nolte et al.*, 2004].
All measurements were performed in front of the beam window (0° position) at a

distance of 2 m. It was necessary to conduct a background measurement with a shadow cone due to the gamma radiation and back scattered neutrons. With the information about the produced charges at the target, which was provided from the PTB, the measured energy spectrum can be corrected by the background. For the calculation of the neutron spectrum the ratio of the charges of the measurement and the shadow cone measurements was used. Figure 5.12 shows the results of the neutron measurements. Shown are the different measured neutron spectra in the inner segment of the C-detector (neutral channel). This means that these are only signals in the neutral channel and none in the anticoincidence. The 8 MeV spectrum (the right panel in the middle of figure 5.12) was not corrected because it was not possible to do a background measurement due to the limited beamtime. In addition the position of the expected neutron edges by elastic scattering is given as the red lines. These neutron edges were calculated with equation 4.5 in chapter 4.2.1 which shows that neutrons can transfer only up to 13% of their primary energy to a silicon nucleus, as discussed in more detail in chapter 4.2.1. The detected signals on the right side of the red lines in figure 5.12 are signals from the non elastic neutron interaction process. The red dashed lines in figure 5.12 show the expected neutron edge range because of the monoenergetic neutron energy uncertainty. *Nolte et al.* [2004] published these uncertainties for the neutron energies which are shown in table 5.3. In the measurements up to 8

Table 5.3.: Neutron uncertainty [*Nolte et al.*, 2004]

Neutron energy / MeV	Uncertainty / MeV
1.2	0.091
2.5	0.127
5	0.200
8	0.200
14.8	0.431
19	0.300

MeV a clear edge is visible and none for 14.8 and 19 MeV, due to the fact that the main interaction process in silicon change between 7 and 8 MeV as shown in figure 5.13. It shows the cross section for neutron interactions in silicon. The black line gives the total cross section, the blue line the non elastic scattering and the red line the elastic scattering process. It becomes obvious that above 8 MeV

the main interaction process is dominated by the inelastic scattering.

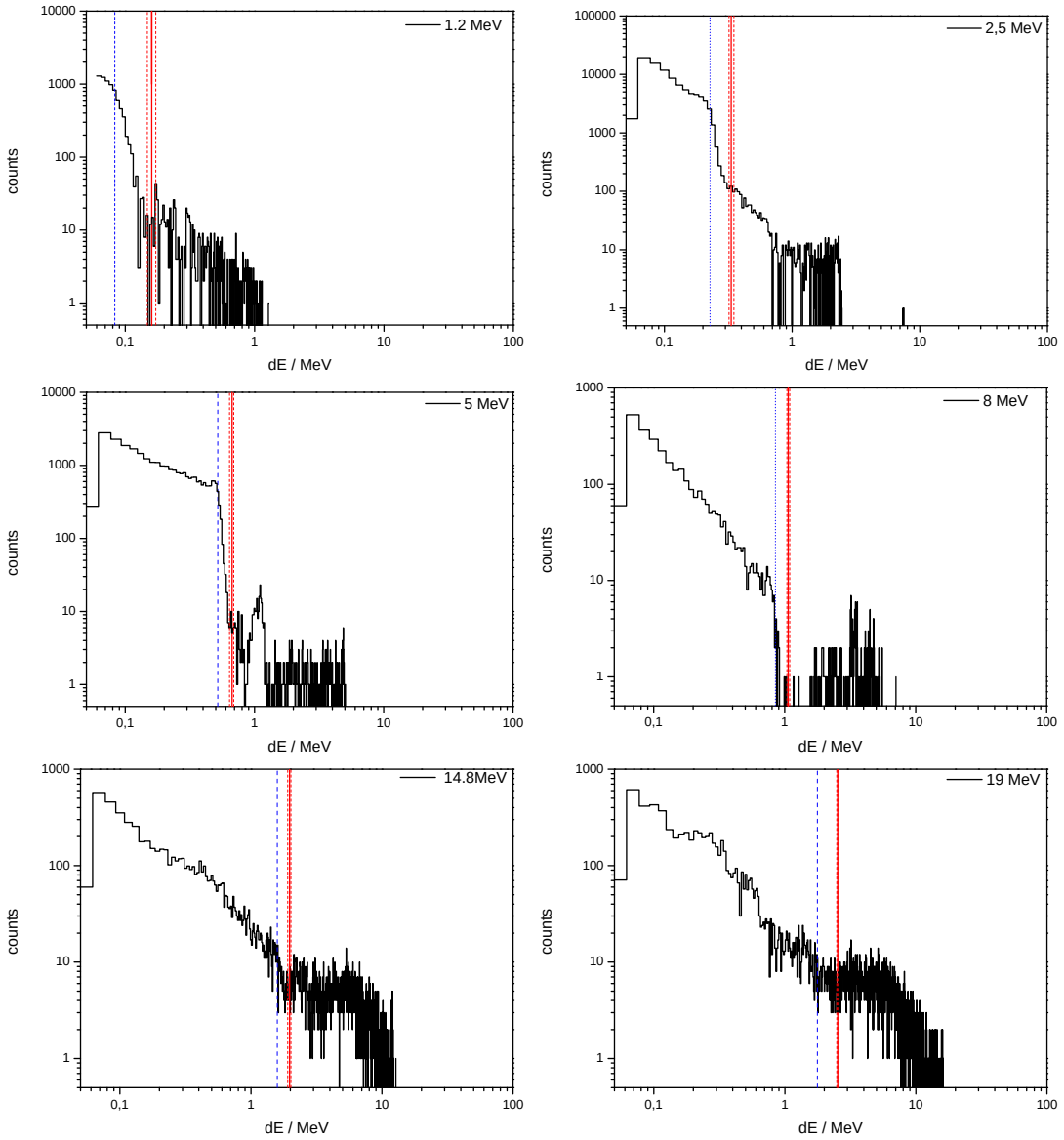

Figure 5.12.: The measured low-energy neutron spectra of the energies 1.2, 2.5, 5, 8, 14.8 and 19 MeV. The red line shows the expected edge of the respective neutron energy. The red dashed line displays the uncertainty of the expected edge. The blue dashed line shows the calculated position of the neutron edge from the measurement.

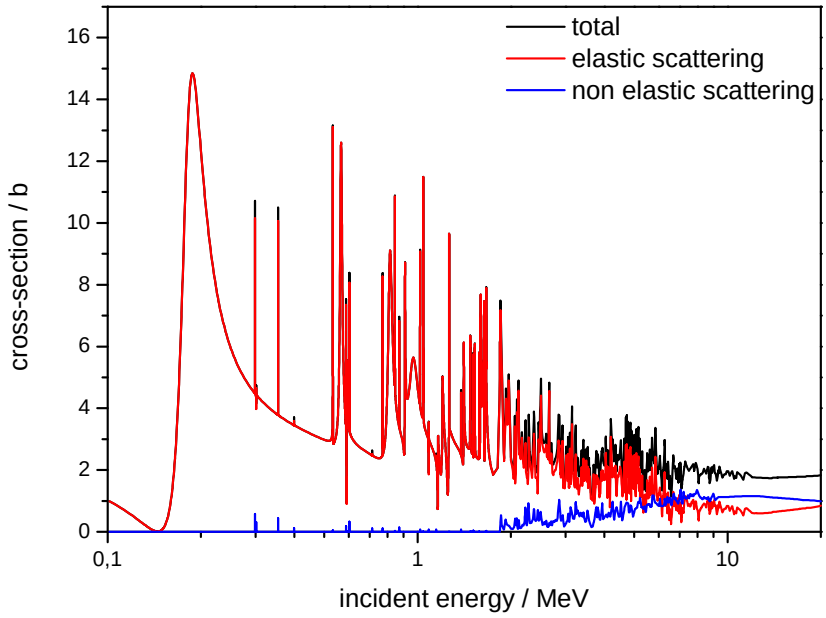

Figure 5.13.: The cross section[1] for neutron interactions in silicon. The black line shows the total cross section, the blue line the non elastic scattering and the red line the elastic scattering process. Above 8 MeV the main interaction process has changed from elastic to inelastic scattering.

The dashed blue line shows the calculated position of the edge. For the calculation of the neutron edges a scalable inverse error function fit was used :

$$f(x) = A \cdot erf(\frac{x - B}{C}) + D, \tag{5.2}$$

with the parameter:

- A: extension of the intensity on the edge position
- B: the position of the edge (half intensity)
- C: width
- D: the intensity height of the position

As an example for the calculation of the neutron edge position figure 5.14 shows

[1] The data are accessible via http://www.oecd-nea.org/janis/

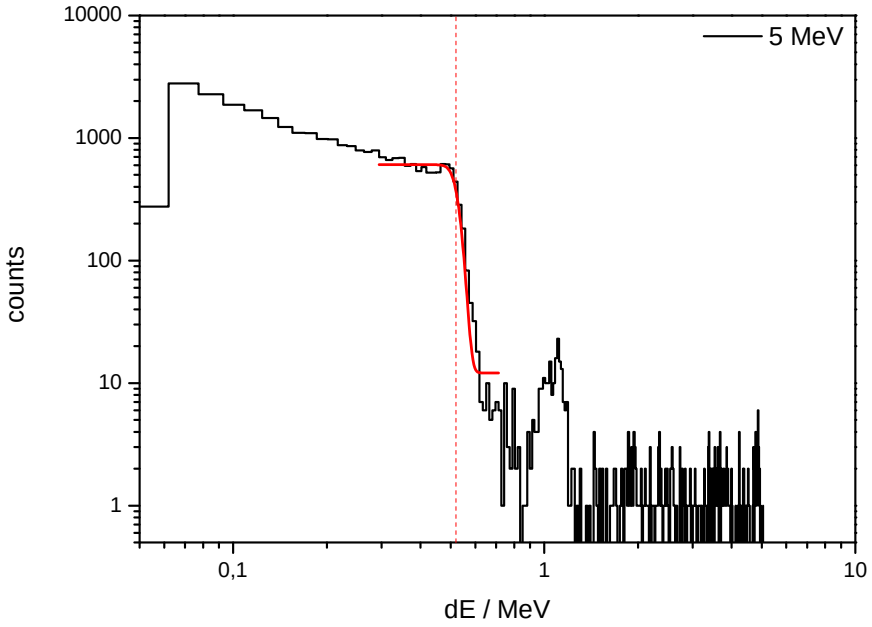

Figure 5.14.: The error function fit to the 5 MeV data in red. The red dash line shows the result of the calculation for the position of the neutron edge.

the error function fit (red) to the 5 MeV data. The red dashed line shows the result of the parameter B which describes the position of the edge[2].
Figure 5.12 shows that the expected and the calculated edge are not in the same position. Figure 5.15 depicts the percentage of the measured to the expected values. The error was estimated from the expected energy range. One can see that the measured value of the expected value rises up to a constant level (80%), a behavior which is expected. The value of the 14.8 MeV and 19 MeV measurement are not reliable due to the fact that these measurements showed no clear neutron edge (see figure 5.12). The effect that the expected neutron edges in the energy loss spectrum are shifted to lower energies can be explained by a pulse height defect, called plasma effect [*Tove and Seibt*, 1967]. This effect was observed for heavy ion measurements in silicon detectors, see e.g. [*Seibt et al.*, 1973] or [*Williams and Lawson*, 1974]. *Hamrita et al.* [2011] published that this effect depends on the Z of the heavy ions and for low Z charged particles, e.g. protons the plasma effect is negligible. The explanation of the plasma effect is that heavy ions produce a cloud of electron-hole pairs. The electric field, which is created

[2]The position is defined as half intensity of the edge

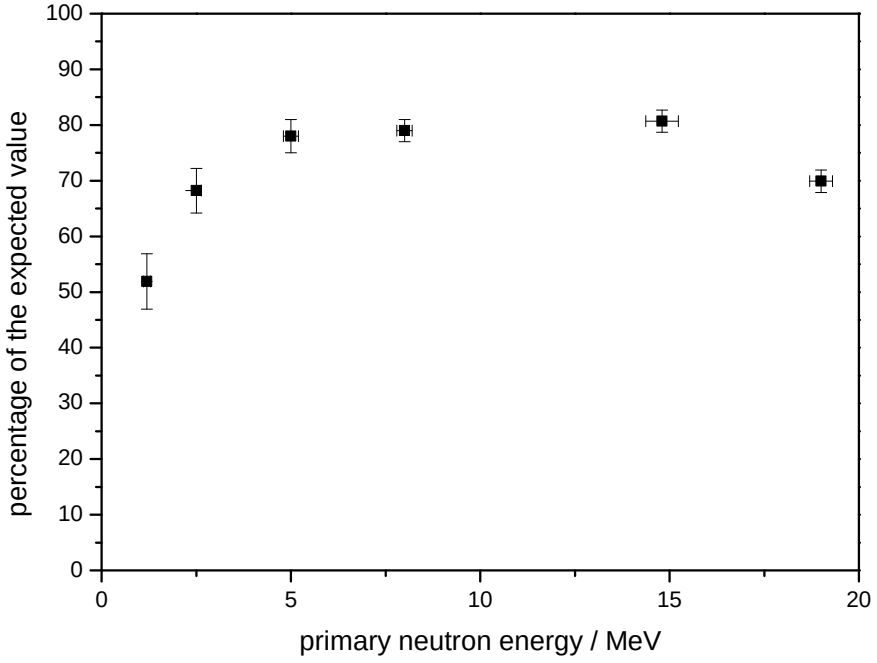

Figure 5.15.: The ratio of measured to expected value in percent

by the bias voltage of the detector, cannot penetrate this cloud in the beginning. The free charge carriers will begin to drift under the influence of the electric field only when the cloud has been sufficiently dispersed. During the initial phase of the cloud the charge carriers can recombine which results in a lower detected pulse height.

In this case FRED measured recoil silicon by the elastic neutron scattering process in silicon. Due to the very short ranges of the recoil silicon in silicon (up to some μm) and the very high ionization density (Z=14) on short range it is plausible that the energy gap between expected and measured value of the neutron edge is caused by the plasma effect. The calculated ranges of the recoil silicon in silicon are shown table 5.4. These values were calculated with SRIM.

Based on these measurements it is possible to determine a correction function for this effect, determined by the following approximation:

$$f(x) = a \cdot exp(-\frac{x}{b}) + c, \tag{5.3}$$

with the parameters:

$$a = 1.260 \pm 0.009 \quad b = 0.133 \pm 0.009\ MeV \quad c = 1.246 \pm 0.005$$

Table 5.4.: Range of recoil silicon in silicon

neutron energy / MeV	recoil Si energy / MeV	range in Si/ μm
1.2	0.156	0.211
2.5	0.325	0.439
5	0.650	0.840
8	1.065	1.180
14.8	2.020	1.760
19	2.530	2.020

Figure 5.16 shows the correction function for neutrons in red in the energy range of 1 MeV up to aproximinatly 10 MeV. This function is only usable for measurements in a neutron field. It considers only the elastic scattering process from neutrons in silicon.

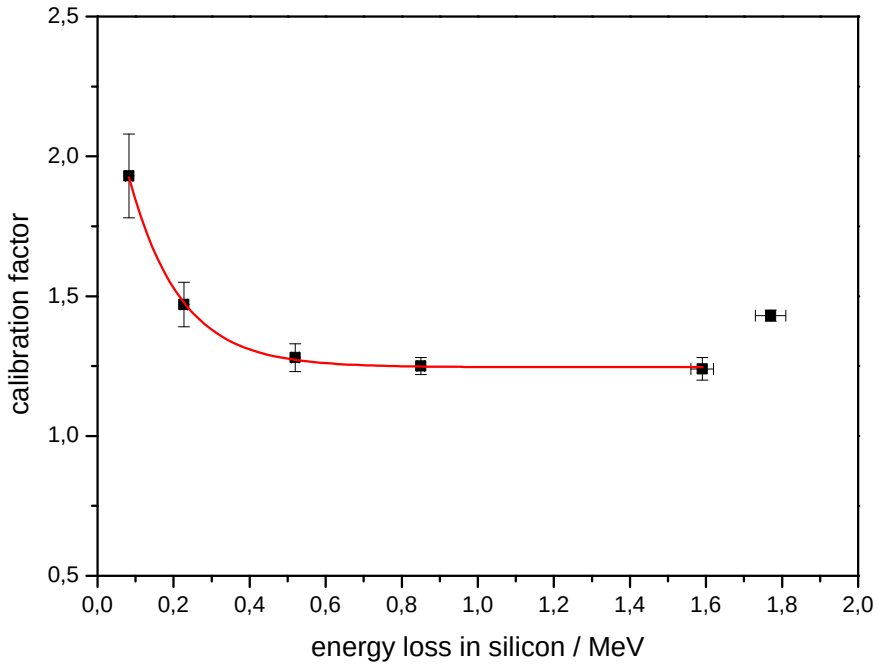

Figure 5.16.: The neutron correction function, which is only usable in a neutron field with neutron energies in a range of 1 MeV up to approximately 10 MeV

5.4.2.2. Measurements in the high-energy reference fields

High-energy neutron measurements with 66 MeV and 97 MeV were taken at the accelerator facility of iThemba Labs in South Africa. The reference field was produced by the exploitation of the ^{7}Li(p,n)^{7}Be target reaction [*Nolte et al.*, 2004].

It was necessary to conduct two measurements for the calibration with high-

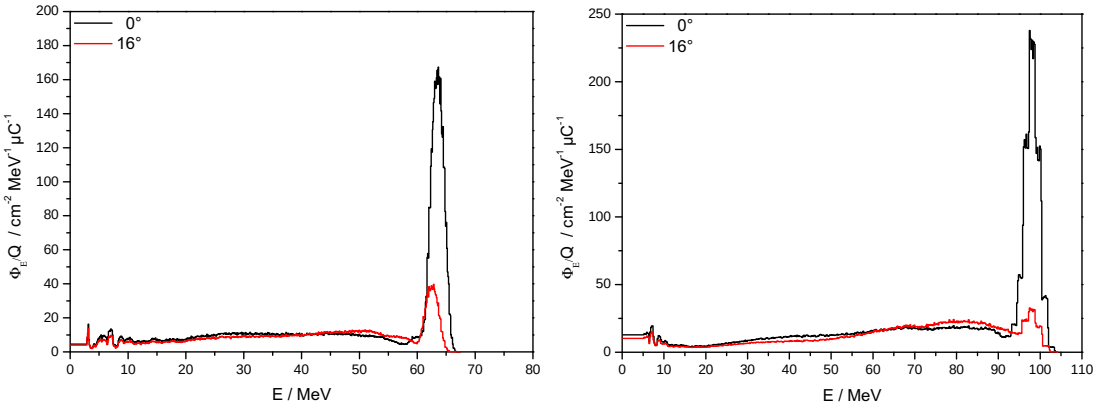

Figure 5.17.: The spectral fluence[3]of the 66 MeV (left side) and 97 MeV (right side) neutron measurement at iThemba Labs. The black curves show the spectral fluence at the 0° position. The red curves show the background measurement on the 16° position.

energy neutrons at the iThemba labs. The first measurement was performed inside the neutron beam at the 0° position and the second one outside of the beam to measure the background (at the 16° position). Figure 5.17 shows the spectral fluence on these two positions. The black curves show the 0° position and the red curve gives the results for the 16° position. It becomes obvious that at the 16° position mainly the background was measured. With a measurement on this position it is possible to correct the primary measurement inside of the beam (0° position). For this correction it is important to know the fluence from both measurements because the spectrum must be scaled by the ratio of the fluences. The fluence values were provided by the PTB as they conducted the metrology of the beam time [*Röttger*, 2013]. Figure 5.18 shows the 66 MeV (left panel) and the 97 MeV (right panel) neutron spectra measured in the inner segment of the C-detector. As mentioned above, these are only signals in the neutral channel and none in the anticoincidence. The black curves show the primary measure-

[3]The fluence values were provided by the PTB

ment inside the beam (0° position) and the red curves show the corresponding background measurement on the 16° position. The right panel reveals that there is no significant difference between the 97 MeV primary neutron measurement and the background measurement. This means FRED could not measure the 97 MeV neutrons. The very small difference can be caused by the background because the background at 16° and 0° is only approximately identical (see figure 5.17). The 66 MeV neutron measurement and its background measurement show

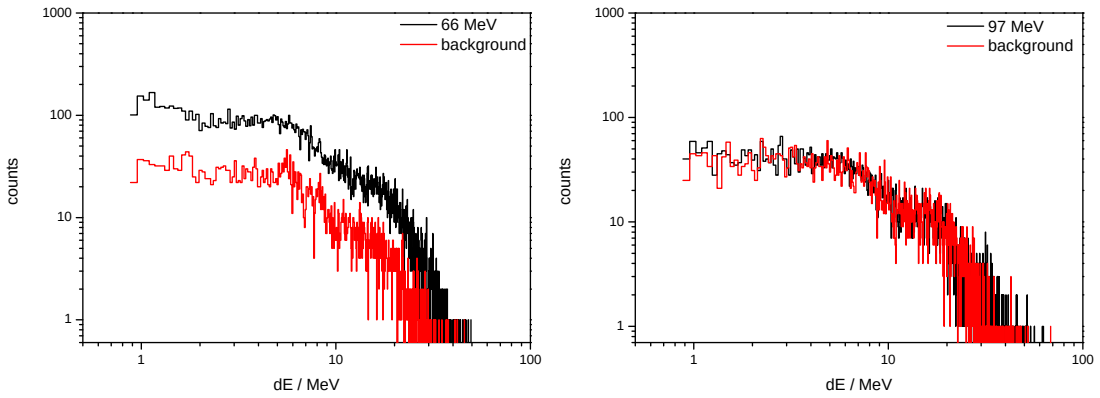

Figure 5.18.: The high-energy neutron measurement. The black curves show the measurement at the 0° position for 66 MeV (left side) and for 97 MeV (right side). The red curves show the corresponding background measurements at the 16° position.

a significant difference. Figure 5.19 shows the corrected spectrum for the 66 MeV measurement. For the correction the background measurement was scaled by the ratio of the PTB fluence values for the 0° and 16° measurement before the correction was applied. The difference spectrum shows a significant number of counts. That means FRED can measure the 66 MeV neutrons but the interpretation of the signal is difficult. For a detailed interpretation of these measurements detailed simulation work is necessary, however, is beyond the scope of this work. One possible explanation is that the high-energy neutrons interact with silicon by compound reaction and spallation processes (see section 4.2). The produced secondary particles in the detector can trigger the anticoincidence, which is a simple explanation why it is not possible to see the 97 MeV neutrons and a large part of the 66 MeV neutrons hits. Figure 5.20 shows this behavior in a 2D histogram for the 66 MeV (left) and 97 MeV (right) runs. It shows the high gain

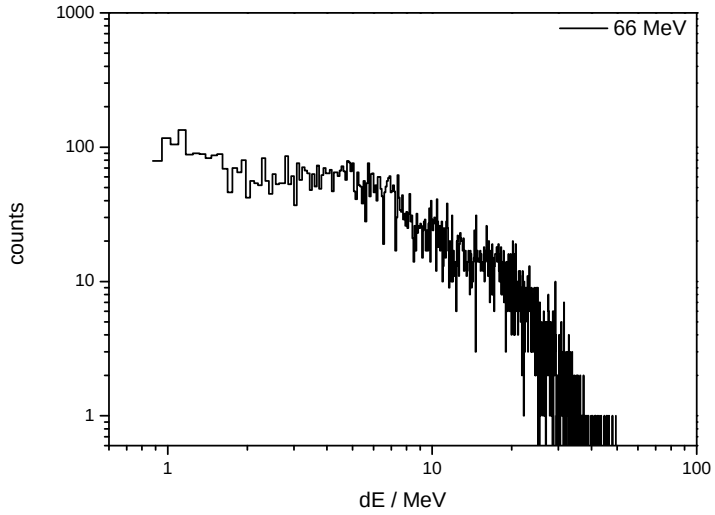

Figure 5.19.: The corrected 66 MeV neutron spectrum.

of the inner segment of detector C versus the inner segment of detector D (high gain). In addition it was considered that there were no hits in the B-detector nor the outer segment of C as further trigger condition. One can see that many secondary particles, produced in the C-detector triggered the D-detector, which is part of the anticoinicidence. These particles formed a cloud shaped structure due to the random energy loss in the two detector segments.

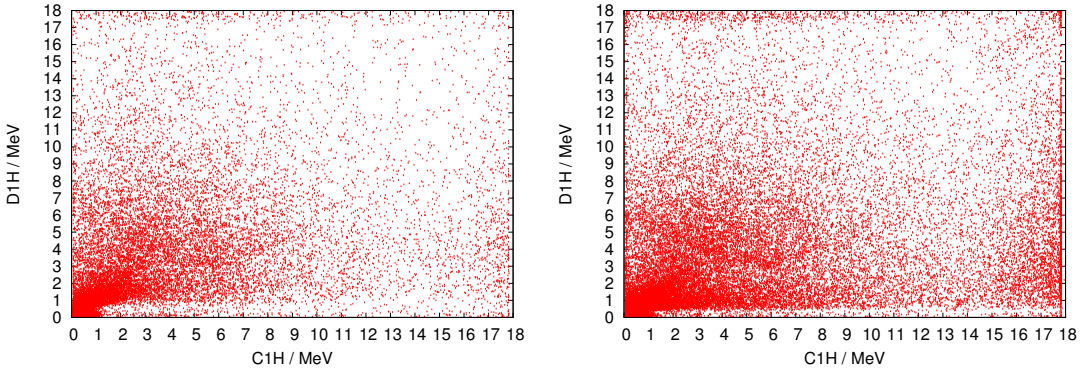

Figure 5.20.: The 2D histogram of the inner segment of detector C (high gain) and inner segment of detector D (high gain). In the left panel the 66 MeV neutron run and in the right panel the 97 MeV run is shown.

5.4.2.3. Measurements with a γ-source

The calibration of the neutral channel has been verified by a measurement with a γ-source. For this review a ^{137}Cs source was used, which emits photons with an energy of 0.662 MeV[4]. Due to the effects discussed in chapter 4.3 a compton edge at 0.478 MeV can be expected. This was calculated by use of equation 4.9. Figure 5.21 shows in black the measurement with anticoincidence conditions for the high gain of the inner segment of the C-detector (C1H). The red line depicts the expected value of 0.478 MeV of the compton edge. It shows that the measured compton edge and the calculated value are comparable. Because of this the calibration is valid and can be used for further investigations. Furthermore, this measurement shows that the observed plasma effect in the neutron measurement is real and no artifact of the calibration.

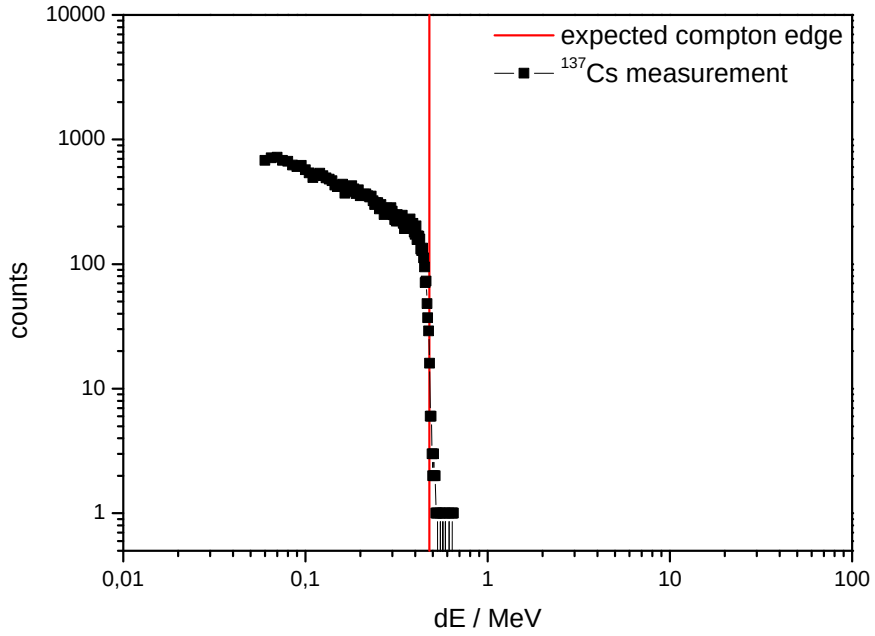

Figure 5.21.: The black curve shows a γ-source (^{137}Cs) measurement in the high gain of the inner segment of the C-detector (C1H). Anticoincidence condition for the C1H was used. The red line shows the expected value for the compton edge.

[4]The information is available via http://www.nndc.bnl.gov/nudat2/chartNuc.jsp

6. Measurements and Results

In this chapter, the different measurements in the Earth's atmosphere conducted with FRED will be shown. In order to verify the performance of the telescope in a complex natural radiation field the measurements onboard an aircraft will be addressed before the main measurement on the stratospheric balloon is shown. This flight was performed in order to get measurements in higher altitude to estimate the radiation exposure up to 25 km.

6.1. Measurement Onboard an Aircraft

6.1.1. The Measurement Flight From Tokio to Frankfurt

In the beginning of 2012 two measurement flights from Tokio (NRT) to Frankfurt (FRA) were conducted to acquire data in a low vertical geomagnetic cut-off rigidity region. In figure 6.1 the flight path of both flights is shown in red on a

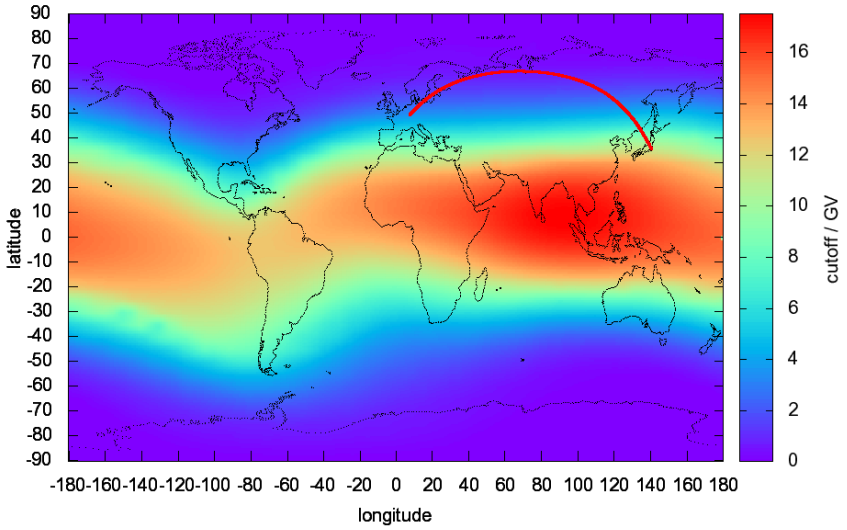

Figure 6.1.: The flight path on a world map of vertical geomagnetic cut-off rigidity for the measurement NRT-FRA.

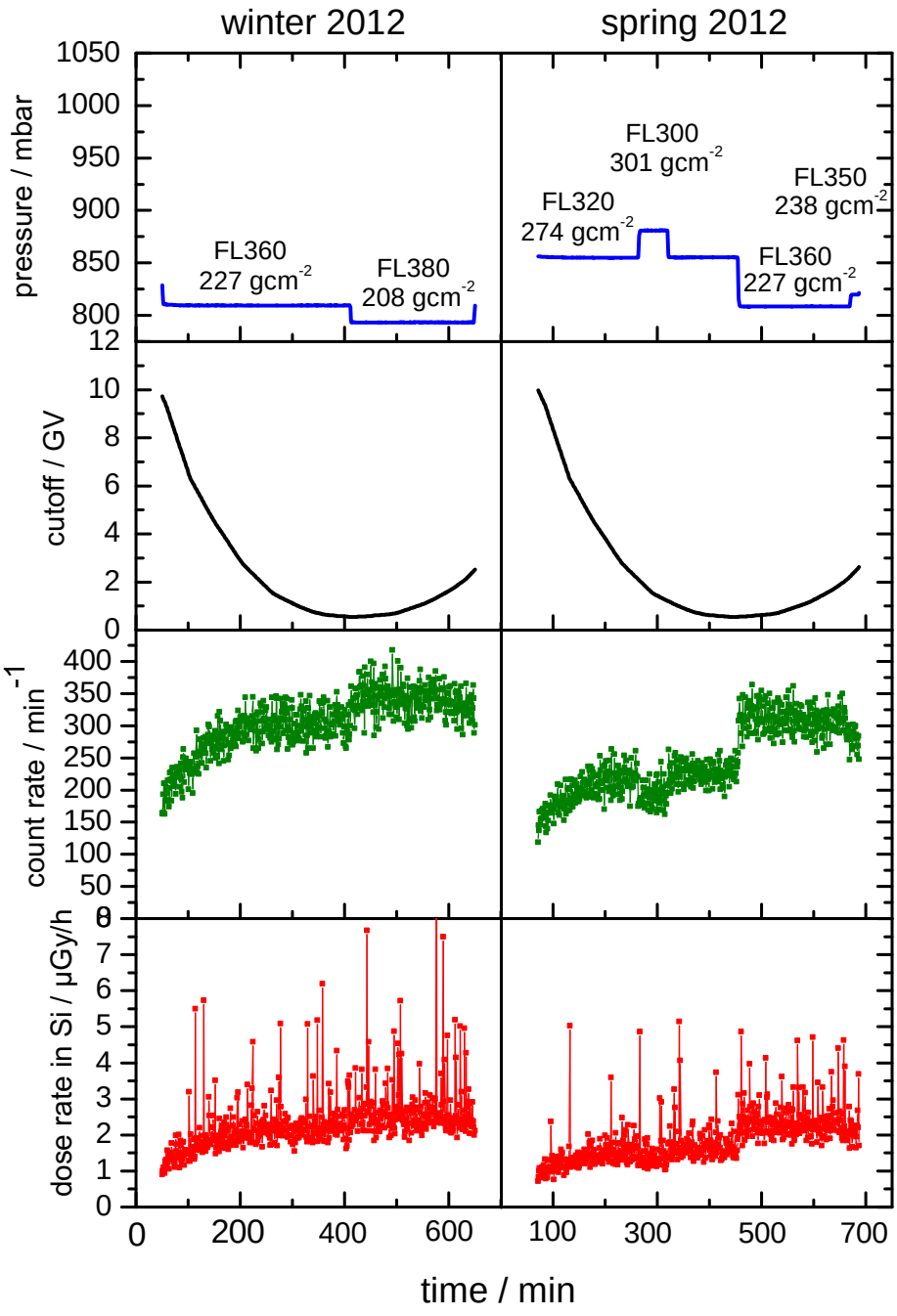

Figure 6.2.: The measurement flight NRT-FRA in the winter 2012 on the left side and in the spring 2012 on the right side. The blue curve shows the altitude information of the airplane, the black curve the cut-off rigidity on the flight path, the green curve displays the count rate and the red curve the dose rate in silicon.

world map of the vertical geomagnetic cut-off rigidity. Furthermore, the measurements from Tokio to Frankfurt are given in Figure 6.2. The blue curves depict the cabin pressure, an indicator for the flight level (FL) which are specified. In the second row the cut-off rigidity is shown in black. The measured count rate (green) and corresponding dose rate (red) are shown in the third and forth row panels. The spikes in the dose rate were produced by high LET particles which are neutrons or heavy nucleus interactions in the single detector. A comparison of these two flight shows that the dose rates are smaller during the second flight for comparable cut-off rigidity values. An explanation can be found in the lower cruising altitude of the second flight. In the count rate profile (green curve) the flight level changes can be seen very well. Furthermore the latitude effect in the dose rate and count rate were observed. With decreasing cut-off rigidity the dose rate and the count rate increased.

6.1.2. The Measurement Flight From Frankfurt to Johannesburg

In autumn 2011 a flight crossing the equator has been performed to acquire data for higher cut-off rigidity region. The measurement was performed on a flight from Frankfurt (FRA) to Johannesburg (JNB). In figure 6.3 the flight path is shown in red.

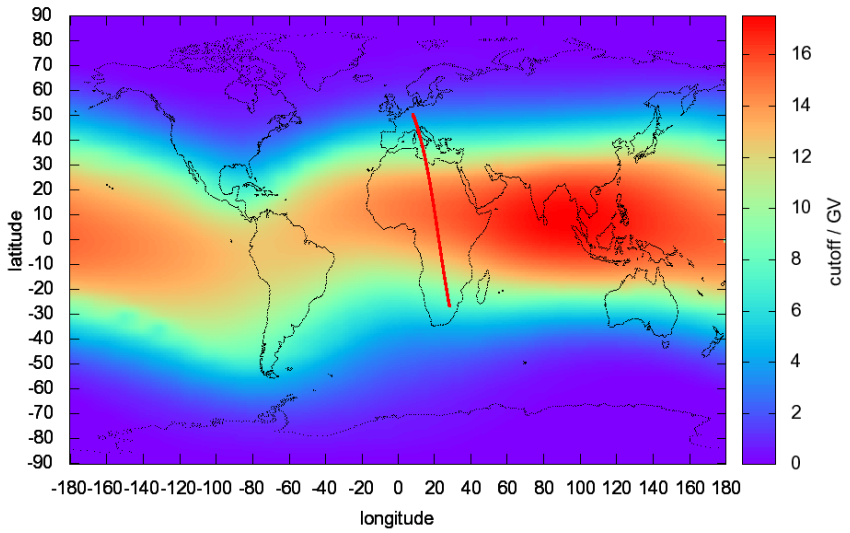

Figure 6.3.: The flight path on a world map of vertical geomagnetic cut-off rigidity for the measurement FRA-JNB.

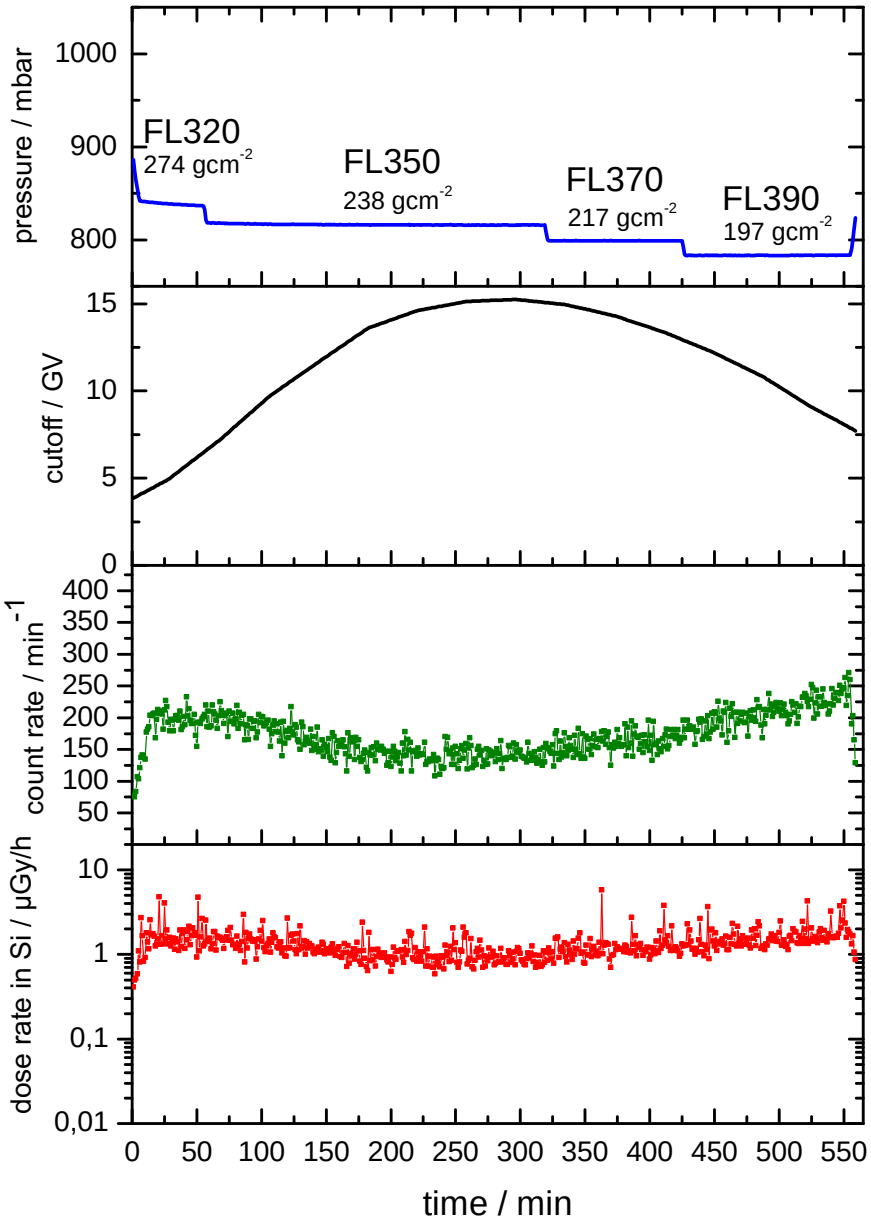

Figure 6.4.: The measurement flight FRA-JNB in the autumn of 2011. The blue curve shows the altitude information of the airplane, the black curve the cut-off rigidity on the flight path, the green curve displays the count rate and the red curve the dose rate in silicon.

Figure 6.4 depicts all important values of the measurement: in blue the flight level, in black the cut-off rigidity, in green the count rates, and in red the dose rate in silicon. The count rate and the dose rate profile show the latitude effect

whereas in the count rate the flight level changes can not be observed. A reason for this can be found in the large cut-off rigidity changes during the flight level changes. Furthermore, at the end of the time series the count rates are higher than in the beginning even though the cut-off rigidity regions are comparable. This is due to the higher cruising altitude towards the end of the flight.

6.1.3. Results From Aircraft Measurements

The radiation field at cruising altitude is well known and can be used for functional tests in a natural mixed radiation field. For this analysis the data from the two measurement flight from Tokio (NRT) to Frankfurt (FRA) and from the flight Frankfurt to Johannesburg (JNB) were used. In addition, when there were data available, the return flights were used as well. Depending on the measuring location the data can be sorted into different groups. Due to the described effects in chapter 3.2 there are two regions: the polar ($R_c < 2$GV) and the equator region ($R_c > 11$GV). Because of the few measurement points between these two regions, these data points were merged together in an intermediate region. Inside these three regions the altitude dependence of the dose rate in silicon between flight levels 300 and 400 was investigated. Figure 6.5 shows the result of the

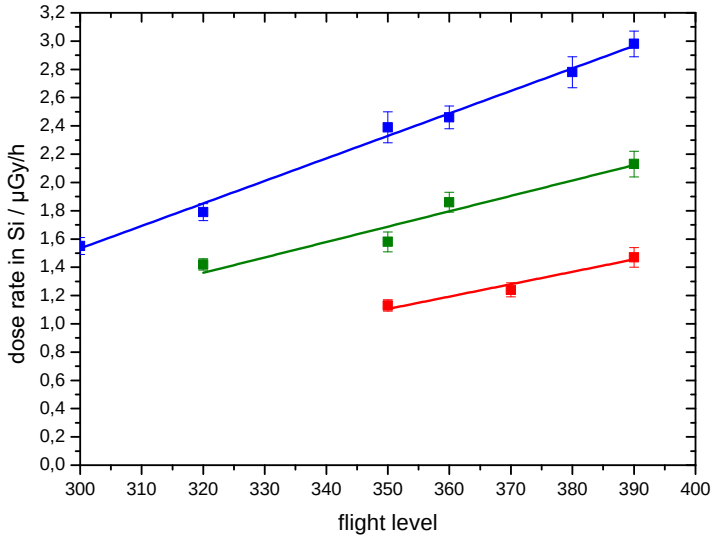

Figure 6.5.: The altitude dependence of the dose rate in cruising altitudes measured on board aircraft in the polar region (blue), in the transition region (green) and in the equator region (red) between flight levels 300 and 400.

altitude dependence in blue for the polar region, in green for the intermediate region and in red for the equator region. It shows the mean values in the single detector segment of A1, A2, B1 and B2 for the different flight level. The specified uncertainties are the SEM. For all three regions a linear increase of the dose between flight levels 300 and 400 is visible, a behavior previously observed by *Schrewe* [2000]. The linear fit parameter for the altitude dependence measurement is shown in table 6.1. A comparison of this result with the data in the

Table 6.1.: Linear fit parameter of the altitude dependence of the dose rate between the flight level 300 and 400.

region	slope / $\frac{\mu Gy/h}{FL}$	intercept / $\mu Gy/h$
polar region (R_c <2GV)	0.0159 $\pm 7 \cdot 10^{-4}$	-3.242 ± 0.243
transition region (2GV > R_c < 11GV)	0.0110 $\pm 2 \cdot 10^{-3}$	-2.123 ± 0.732
equator region (R_c >11GV)	0.0088 $\pm 1.7 \cdot 10^{-3}$	-1.964 ± 0.636

left plot in figure 3.2 shows that the slopes are comparable, but FRED measured larger dose rates in silicon ($\sim$ 12%) due to the higher energy lost range. This effect is greater than 12% in consideration of the solar cycle because the data were measured in two different phases of the solar cycle. The data in figure 3.2 were measured during solar minimum conditions and the data of FRED were measured during the increasing phase of the solar activity.
Furthermore, *Schrewe* [2000] showed the sigmoidal behavior of dose rate depending on the cut-off rigidity. For this investigation the measured data were scaled to flight level 360 with the slopes of the altitude dependence given in table 6.1. In addition for the detector segments A1, A2, B1 and B2 a mean value in a cut-off rigidity interval of 1 GV was build, as shown in Figure 6.6. The depicted values are mean values of the four detector segments in cut-off rigidity intervals with the SEM. The result shows the expected sigmoidal trend of the dose rate.
The next step is the evaluation of measured energy loss spectra. Figure 6.7 shows the energy loss spectra from the two flight routes. The left panel shows the energy loss spectrum from the flight Frankfurt to Johannesburg and the right panel from Tokio to Frankfurt. The blue curves depict the energy loss spectra in the A1 detector segment measured in coincidence mode. Because in coincidence condition the particles must hit the inner segments of detector A and B it is possible to identify these particles as charged. A comparison of these two spectra shows that

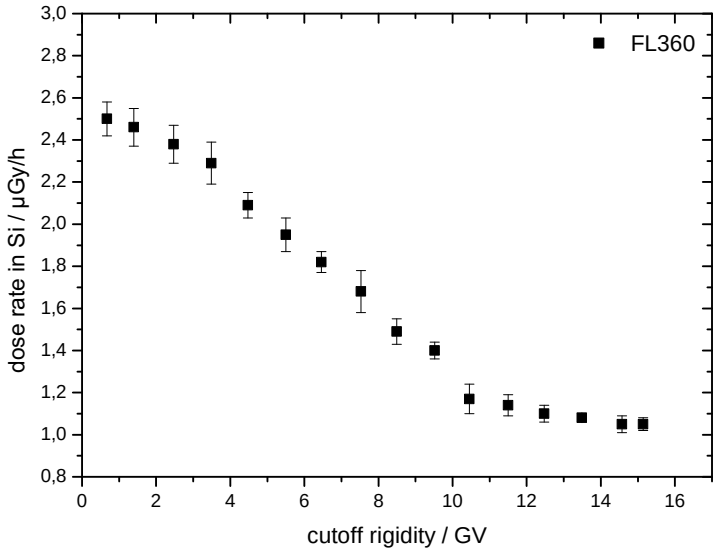

Figure 6.6.: The dose rate versus cut-off rigidity for the flight level 360 in a cut-off rigidity interval of 1 GV.

the particle flux near the equator (FRA-JNB) is smaller. Furthermore, the high energy channels detected less particles due to the higher cut-off rigidity values on the given flight path. In addition the red curves show the measured energy loss spectra for neutral particles. These particles had only triggered the inner

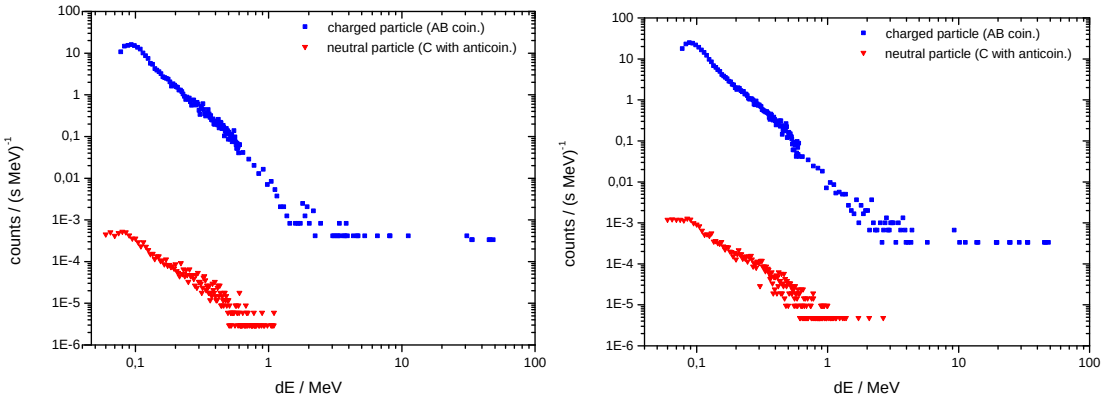

Figure 6.7.: Measured energy loss spectrum of the flight FRA-JNB (left panel) and energy loss spectrum of the flight NRT-FRA (right panel). The blue curves depict the energy loss spectra in the A1 detector segment measured in coincidence mode and the red curves show the measured energy loss spectra for neutral particles.

segment of detector C (C1) and not the anticoicidence (B1, B2, C2, D1, D2). For neutral particle fluxes the same behavior as for the charged particle flux was observed. Figure 6.8 shows the neutral spectrum from the flight Tokio to Frankfurt in more detail. It shows an edge at 130 keV which corresponds to the expected neutron edge in silicon due to the natural neutron spectrum shows two prominent peaks at around 1 MeV (intensity maximum between 1 and 2 MeV) and 100 MeV [*Goldhagen et al.*, 2004] and because of the fact that neutrons can only deposit 13% of their energy in silicon by elastic scattering (see chapter 4.2).

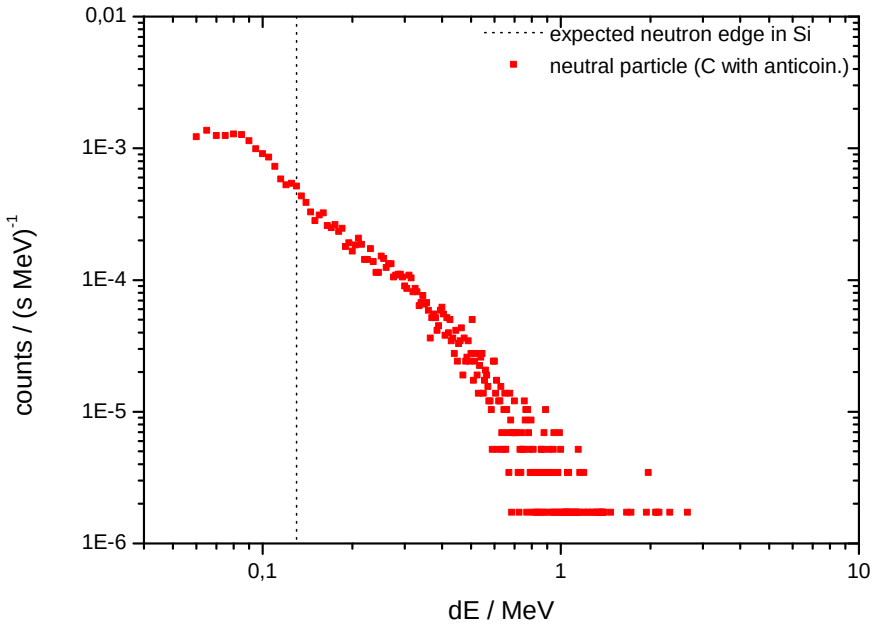

Figure 6.8.: The neutral spectrum measured during both flights NRT-FRA.

For the determination of the radiation protection unit dose equivalent the mean quality factor $\bar{Q}$ must be calculated. This can be done by analysis of the measured coincidence energy loss spectrum. The method will be described and illustrated in chapter 6.2.3 by using the example of the balloon flight measurement. At this point only the results of the mean quality factor $\bar{Q}$ at cruising altitudes will be shown in table 6.2. The mean quality factors are in good agreement with the Dosimetry Telescope (DOSTEL) measurements ($\bar{Q} = 1.37 \pm 0.1$) [*Beaujean et al.*, 2005]. The indicated error is the 10% uncertainty which was calculated by *Beaujean et al.* [1999, 2005] with the DOSTEL measurement during several flights. The comparison of the measured mean quality factor values of DOSTEL

Table 6.2.: Mean quality factors onboard aircraft

flight path	mean altitude	$\bar{Q}$
NRT-FRA (both flights together)	FL 350	1.36± 0.14
FRA-JNB	FL 360	1.08± 0.11

and FRED is acceptable because the measured particles are in the same LET range and were detected in the same material. Thereby the high-LET events will be produced by the same physical processes in silicon which are dominated by neutron-induced secondary short range particles. Due to the comparably rather poor statistics in the high-LET channels and the big impact of these particles to the mean quality factor, the uncertainties are also comparable.
With these mean quality factors $\bar{Q}$ and the water conversion factor F ($F = 1.20$) it is possible to calculate the ambient dose equivalent H from the absorbed dose D in silicon with the relation:

$$H = F \cdot \bar{Q} \cdot D. \tag{6.1}$$

Table 6.3 shows the results from the measurement flights.

Table 6.3.: Measured total dose onboard aircraft

flight path	mean altitude	D / μGy	H / μSv
NRT-FRA (Jan.)	FL 370	25.01±0.95	40.82±1.55
NRT-FRA (May)	FL 330	20.36±0.68	33.23±1.11
FRA-JNB	FL 360	12.83±0.46	16.63±0.46

The denoted absorbed dose values D are mean values from the single measurements in the detector segments A1, A2, B1 and B2 and the uncertainties are the SEM from these measurements. The uncertainty of the dose rate measurement is $\sim 4\%$. However, the calculated ambient dose equivalent values H are too small because of the rather poor sensitivity of neutrons in silicon. Table 6.4 shows the measured neutral dose during the flights and the part P of the mean total dose D in percent. The measured absorbed dose is mainly originating from charged particles and the part of the neutral dose can be negligible because table 6.4 shows that the neutral dose values are smaller than the uncertainty of the absorbed dose measurement ($\sim 4\%$). Therefore the calculated ambient dose equivalent in table

Table 6.4.: Measured neutral dose onboard aircraft

flight path	mean altitude	D / μGy	P / %
NRT-FRA (Jan.)	FL 370	0.85	3.4
NRT-FRA (May)	FL 330	0.66	3.2
FRA-JNB	FL 360	0.39	3

6.3 is too small. Figure 6.9 displays the relative contribution of the ambient dose

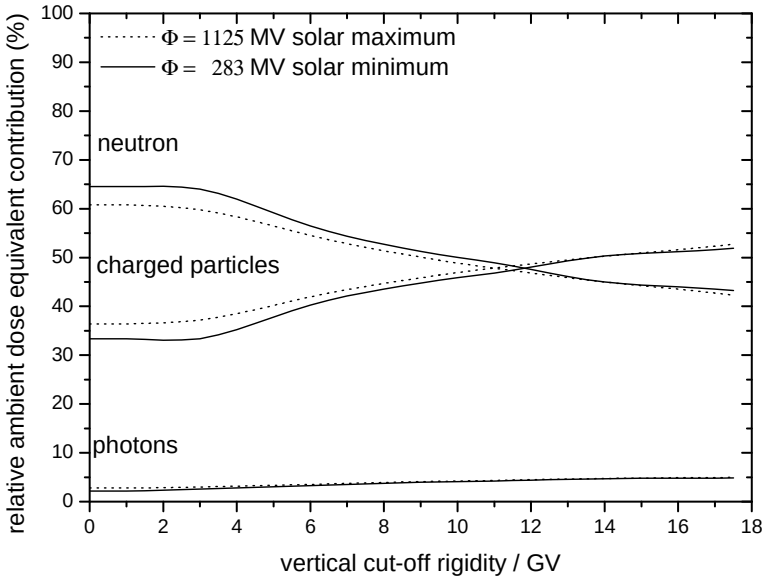

Figure 6.9.: The percentage of the composition of the ambient dose equivalent rate for the flight level 350 (left) for solar minimum and maximum conditions which was calculated with EXPACS. The solid line displays the dose rate composition for the solar minimum (Φ = 283MV) and the dotted line for solar maximum conditions (Φ = 1125MV) *Möller et al.* [2012].

equivalent rate at flight level 350 for the solar minimum and maximum conditions depending on the cut-off rigidity calculated with EXPACS [*Sato and Niita*, 2006]. The solid line displays the dose rate composition for solar minimum (Φ=283 MV) and the dotted line for solar maximum conditions (Φ=1125 MV). The comparison shows that the influence of the different components changes from solar cycle minimum to solar maximum. It becomes obvious that the neutron part of the ambient dose equivalent is between ∼35% and ∼65% depending on the cut-off rigidity. Due to the high percentage of the neutron dose the measured ambient

dose equivalent in silicon detectors is underestimated [*Möller et al.*, 2012].
The measurements with FRED onboard an airplane showed the expected behavior in the complex natural radiation field and the performance of FRED is excellent. Now it is possible to measure with FRED in a mainly unknown radiation field in higher altitudes up to 25km.

6.2. Measurement Onboard a Stratospheric Balloon

For the investigation of the radiation field in higher altitudes FRED has been part of a payload onboard the stratospheric balloon BEXUS 13. Balloon-borne Experiments for University Students (BEXUS) is a German-Swedish student program which provides the opportunity to send experiments into the stratosphere. These stratospheric balloons are unguided and reach a maximum altitude of 25 km. The typical flight time is between 2 to 5 hours, depending on weather and

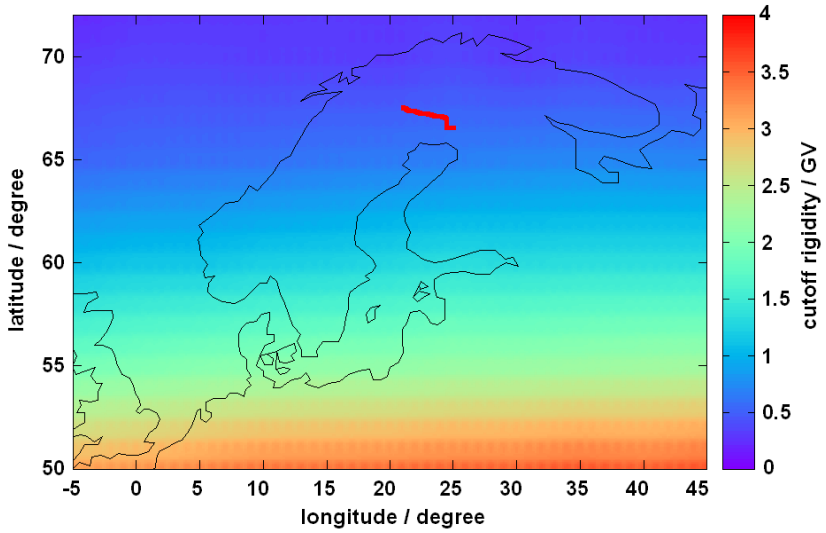

Figure 6.10.: The flight path of the BEXUS13 balloon.

wind conditions[1]. BEXUS 13 was launched on 28.09.2011 at 17:00 local time near Kiruna in northern Sweden on the European launching site for rockets and balloons, Esrange Space Center. Figure 6.10 depicts the flight path of the balloon marked in red on a map of the vertical geomagnetic cut-off rigidity. The impact site of the balloon was near Rovaniemi in Finland. During the flight the cut-off

[1]More information is available via http://www.rexusbexus.net

rigidity varied in the range of 0.45 GV up to 0.6 GV and therefore the cut-off rigidity changes can be neglected for the data evaluation.

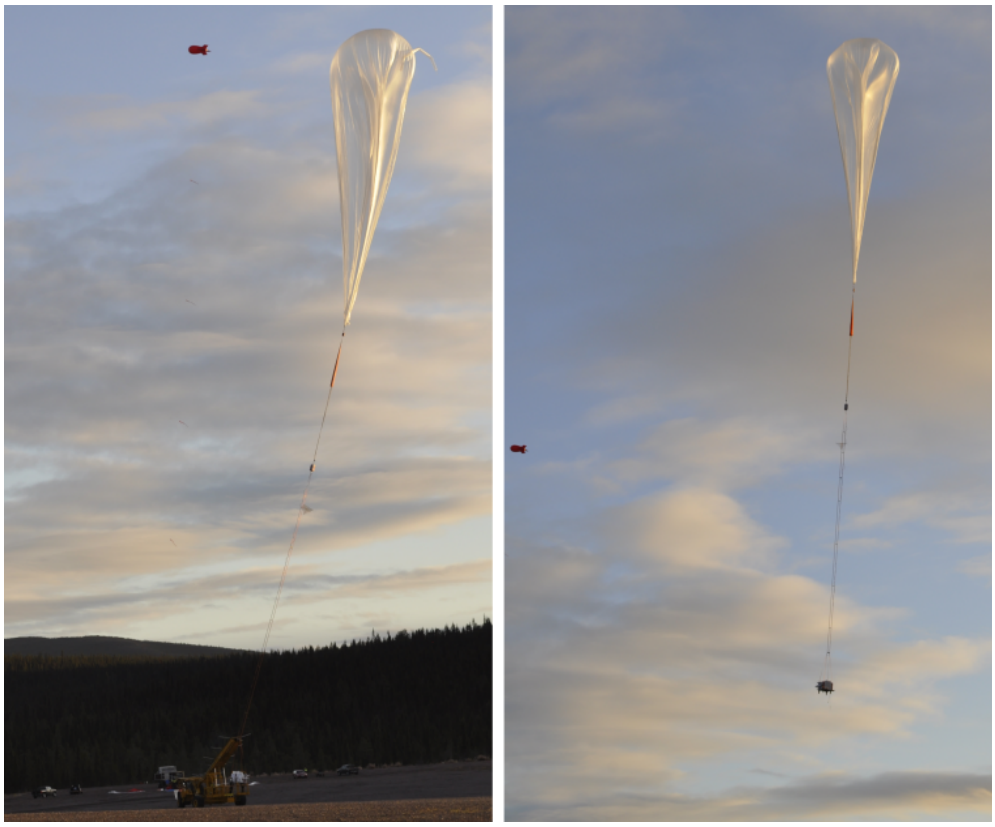

Figure 6.11.: The BEXUS13 lift off at ESRANGE near Kiruna.

Figure 6.11 shows two pictures of the BEXUS 13 flight train lift off. The BEXUS flight train provided several parameters, e.g. atmospheric pressure and temperature, GPS-information about altitude and geographic coordinates. Furthermore, data up- and downlink was provided to connect the experiment with a ground station during the flight. Relevant atmospheric parameters are shown in figure 6.13. FRED was mounted on an aluminium framework in the upper part of the gondola, shown in figure 6.12. For temperature insulation a Expanded Polypropylene (EPP) box (black box) displayed on the right picture was used. Figure 6.13 shows in green the temperature environment during flight. One can see that the operating environment of FRED had a wide range: +10 to -60° C. Various thermal-vacuum tests had proven that an EPP box wall thickness of 5 cm is sufficient to measure in this temperature environment. Furthermore, the tests had shown that there was no corona discharge during the exposure to the

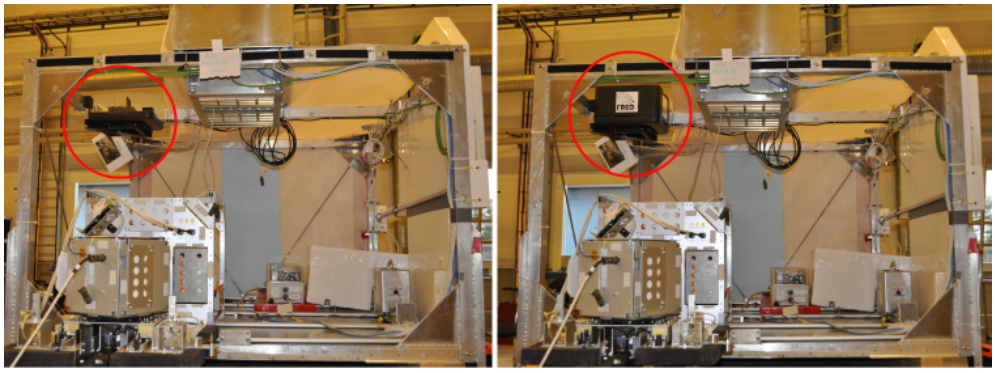

Figure 6.12.: The open gondola during the mounting phase. On the left picture one can see the position of FRED mounted on an aluminium framework in the upper part of the gondola without thermo insulation. On the right picture one can see FRED with the thermal insulation (black box).

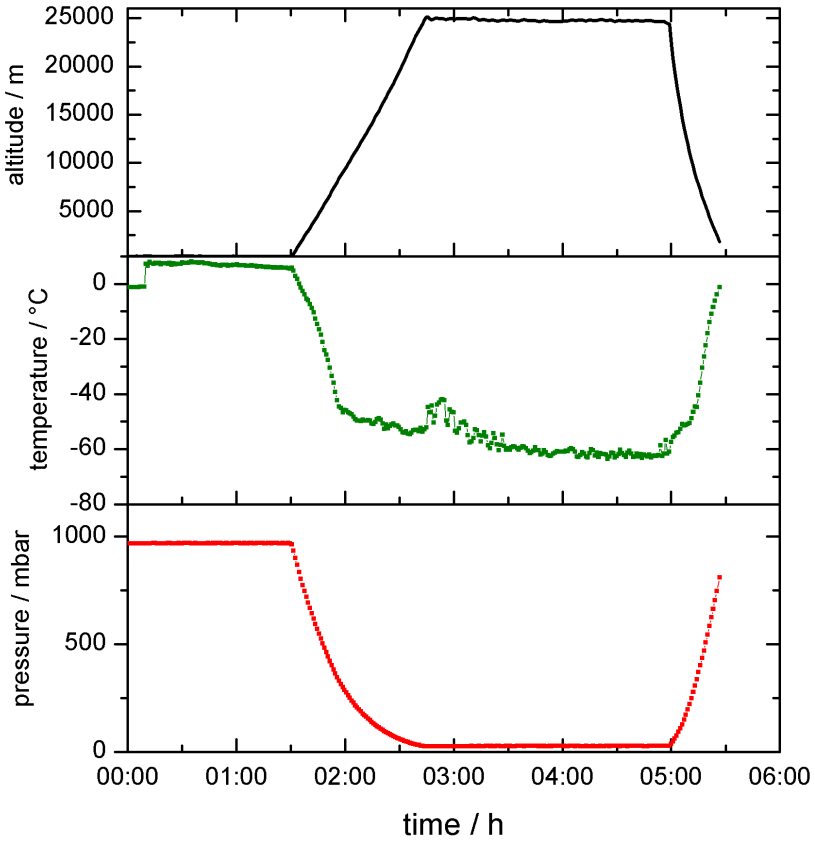

Figure 6.13.: BEXUS13 housekeeping data from the flight train.

low pressure environment.
Figure 6.14 shows the count rate time profile for the A-detector (A1H, A2H) and the B-detector (B1H, B2H) during the balloon flight in counts per minute. These count rate values are comparable. The count rate in the B1H (blue curve) is increased due to the higher active area of B1H and accords to the expected

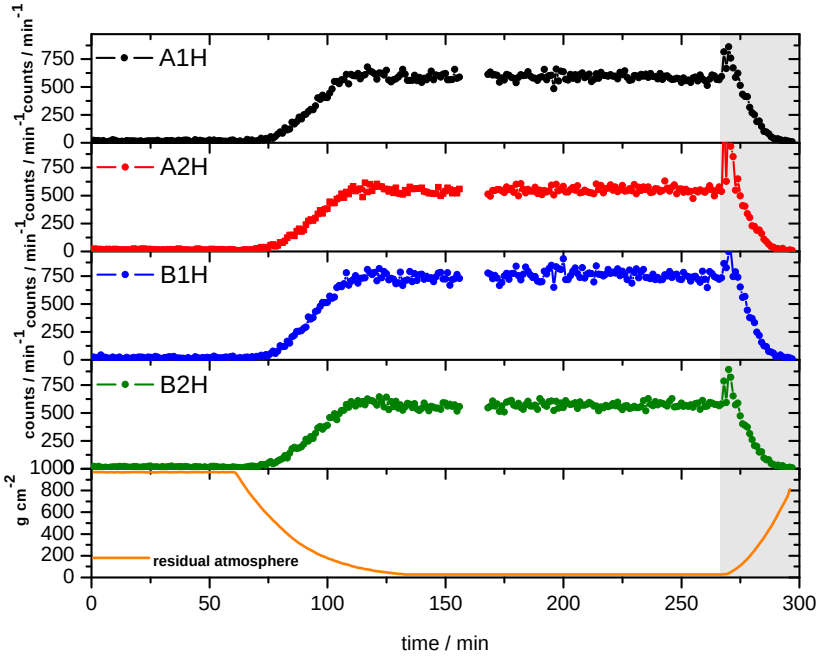

Figure 6.14.: The count rate time profile of the balloon measurement for high gain of the A and B detector segments. The increasing count rate in the gray area is a disturbance due to the cut down of the balloon.

values (see figure 6.17). The orange line shows the residual atmosphere during the measurement. The increasing count rate in the end of the time series (gray area) is a disturbance based on the cut down of the balloon. These values are not a part of the analysis in the following sections. From the measurements it is possible to calculate the dose rate in silicon. In figure 6.15 the dose rate time profile of the A- and B-detector derived from the measurements are shown. These measurements show spikes due to the low gain trigger which is shown in figure 6.16. It depicts count rates for the high gain in red and for the low gain in blue in the lower panel. The green curve in the upper panel indicates the altitude profile during the balloon flight (right y-axis) and the orange curve shows the

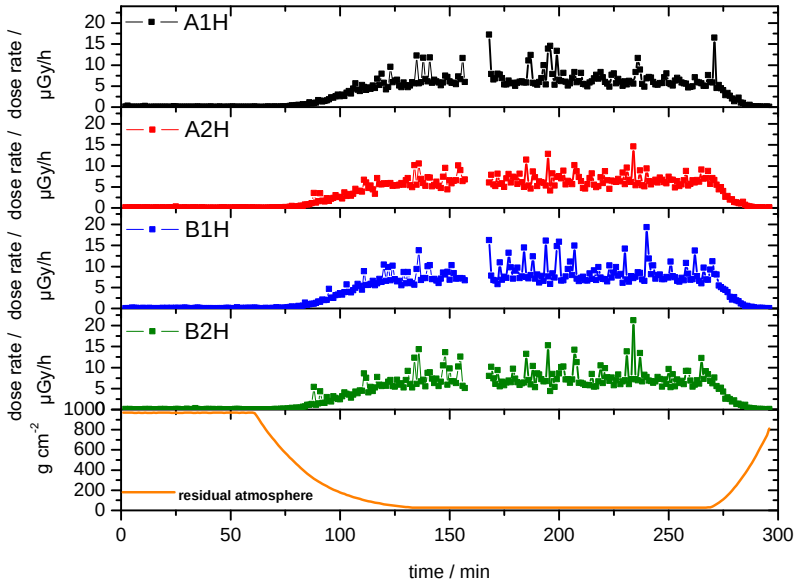

Figure 6.15.: Dose rate time profile measured on the balloon flight for high gain of the A and B detector segments.

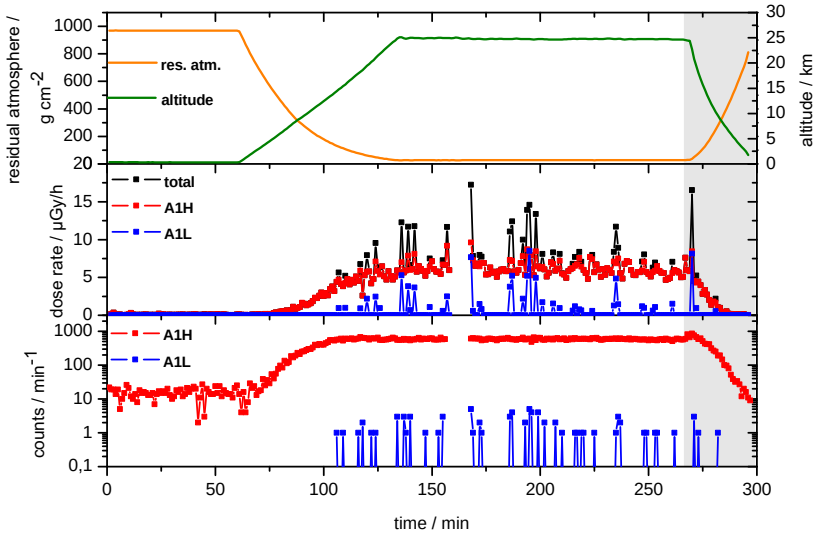

Figure 6.16.: Dose rate time profile for the A-detector. The increasing count rate in the gray area is a disturbance due to the cut down of the balloon.

corresponding value of the residual atmosphere. In the middle panel the dose rates in silicon in the inner segment of detector A (A1) for the high (red) and low gain (blue) are depicted. The black curve shows the total dose rate in silicon. A

comparison of these three panels yields that the spikes in the total dose derive from only a few particles measured in the low gain above 16 km altitude. For a low gain trigger particles must deposit at least 17.2 MeV in silicon, which means the observed spikes were produced by neutron, interaction by heavy nuclei or stopping particles.

6.2.1. Analysis of the Count Rates

Figure 6.17 shows the comparison of the high gain of the A1, A2, B1 and B2 detector segments. Due to the different active areas the count rates are scaled to cm^{-2}. It shows that the count rates of all detector segments are comparable. The increasing count rate at the end of the floating phase is an artifact that derives from the cut down and the descent of the balloon. These values are neglected, as mentioned previously.

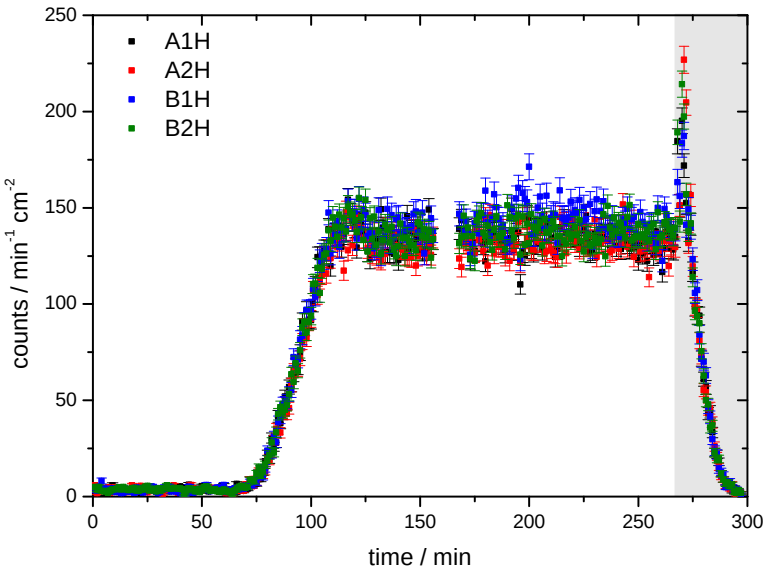

Figure 6.17.: The comparison of count rates per cm^2 in the detector segments A1H (black), A2H (red), B1H (blue) and B2H (green). The increasing count rate in the gray area is a disturbance due to the cut down of the balloon. These values are not a part of the analysis.

6.2.1.1. Determination of the Pfotzer Maximum

For the determination of the Pfotzer Maximum (see chapter 3.2) the count rate profile versus residual atmosphere was analyzed. A mean count rate profile from detector segments A1, A2, B1 and B2 is shown in figure 6.18. The detector seg-

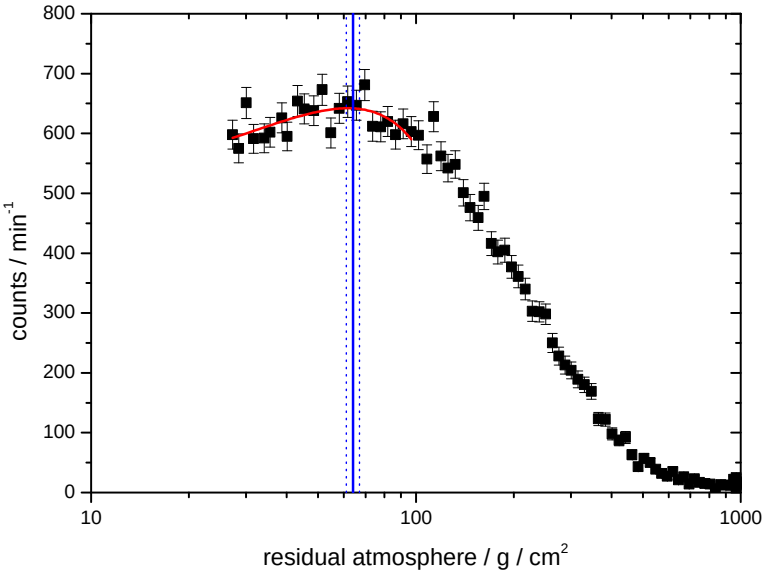

Figure 6.18.: The black dots show the mean value of counts per minute in A1H, A2H, B1H and B2H versus residual atmosphere. The red curve shows the used fit for the determination. The blue line is the result of the determination of the Pfotzer Maximum which is the maximum of the fit curve [*Möller et al.*, 2013b].

ments C2, D1 and D2 were ignored because the C2, and D-detectors had no own trigger conditions and C1 had a lower trigger threshold. The error bars represent the calculated Poisson error. The blue line depicts the calculated altitude of the Pfotzer Maximum. For this calculation a quadratic fit function (red) was used. Data smaller than 100 $\frac{g}{cm^2}$ were fitted with the following fit function:

$$f(p) = A + B \cdot p + C \cdot p^2 \tag{6.2}$$

The results of the fit parameters are shown in table 6.5. The fits yields a result for the Pfotzer Maximum of $64 \pm 3\ g/cm^2$. The error was estimated through the upper and lower limit of the fit parameter uncertainties. The Pfotzer Maximum value can be converted into the altitude unit km for a comparison with other

Table 6.5.: Pfotzer Maximum fit parameter

parameter	result
A	482.32±41.20 $\frac{1}{min}$
B	5.18±1.52 $\frac{cm^2}{min \cdot g}$
C	-0.04 ±0.01 $\frac{cm^4}{min \cdot g^2}$

literature values that are given in km. For the conversion the measured pressure and Global Positioning System (GPS) altitude information of the balloon was used which were provided from the balloon housekeeping data. Due to the pressure is corresponding to the residual atmosphere in Figure 6.19 one can see the GPS altitude in km versus residual atmosphere and the following fit function $A(x)$ (red curve):

$$A(x) = A_0 + B_1 \cdot \left(1 - exp\left(\frac{-x}{t_1}\right)\right) + B_2 \cdot \left(1 - exp\left(\frac{-x}{t_2}\right)\right) \tag{6.3}$$

This fit function is not a typical barometric formula because of the response function of the pressure sensor. In table 6.6 the fit parameters are given.

Table 6.6.: Altitude conversion function fit parameter

parameter	result
A_0	31.874±0.073 km
B_1	-14.412±0.068 km
t_1	49.277±0.678 g cm^2
B_2	-21.667±0.049 km
t_2	620.143 ±9.014 g cm^2

With this conversion function $A(x)$ it is possible to calculate the altitude in km. This function is only valid for the day of the balloon flight because the weather conditions affect characteristics of the function.
The converted values are shown in table 6.7. One can see that the Pfotzer Maximum is located in a range of 18.9 to 19.6 km which is in good agreement to the literature range of 18 to 20 km in the polar region, see e.g. [*Bazilevskaja et al.*, 2008]. Figure 6.20 shows the altitude trend of the count rate. Additionally, the calculated Pfotzer Maximum range is shown in blue.

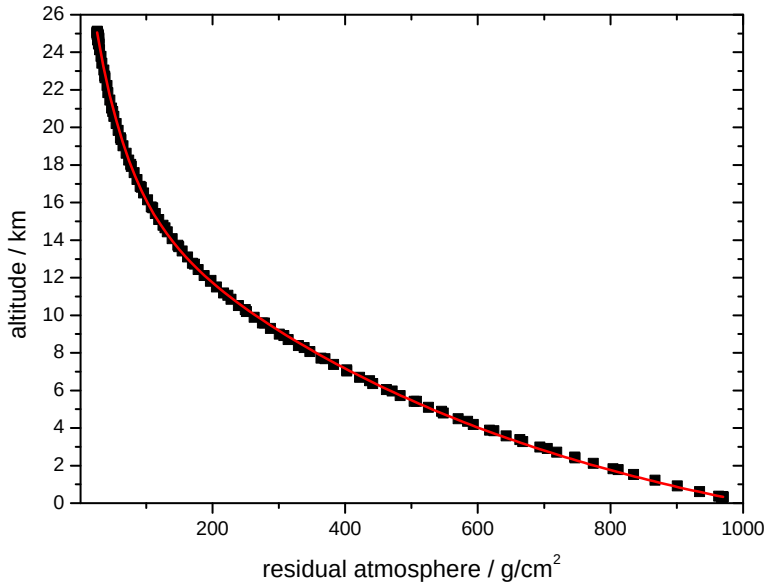

Figure 6.19.: Altitude in km versus residual atmosphere for the BEXUS 13 flight. The red curve shows the fit function $A(x)$.

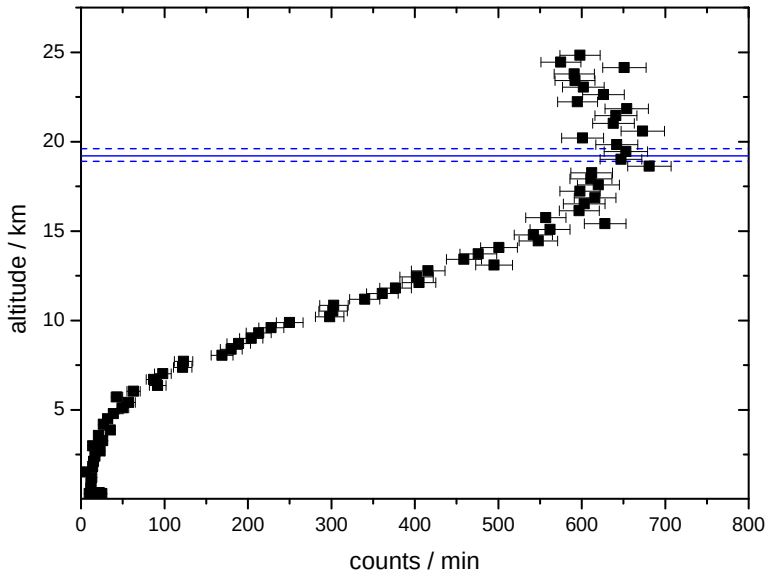

Figure 6.20.: The altitude trend of the count rate. The blue lines show the range of the calculated Pfotzer Maximum

6.2.1.2. Comparison of single and telescope counts

Through the comparison of the single and the telescope count rate the zenith angle distribution can be determined. This distribution is needed to calculate

Table 6.7.: The result of the determination of the Pfotzer Maximmum

residual atmosphere g/cm^2	altitude / km
61	19.6
64	**19.2**
67	18.9

the mean incident angle which is used for the calculation of the mean path length of the particles in the detector.
In figure 6.21 the time series of the balloon flight for the two different modes are shown. The black curve depicts the single count rate and the red curve the coincidence count rate (telescope mode), measured in the high gain of the inner segment of the A-detector (A1H). The given uncertainty is the Poisson error. During the floating phase of the balloon it could be observed that the single counts were about a factor of 4 higher. The altitude dependence of this ratio is shown in

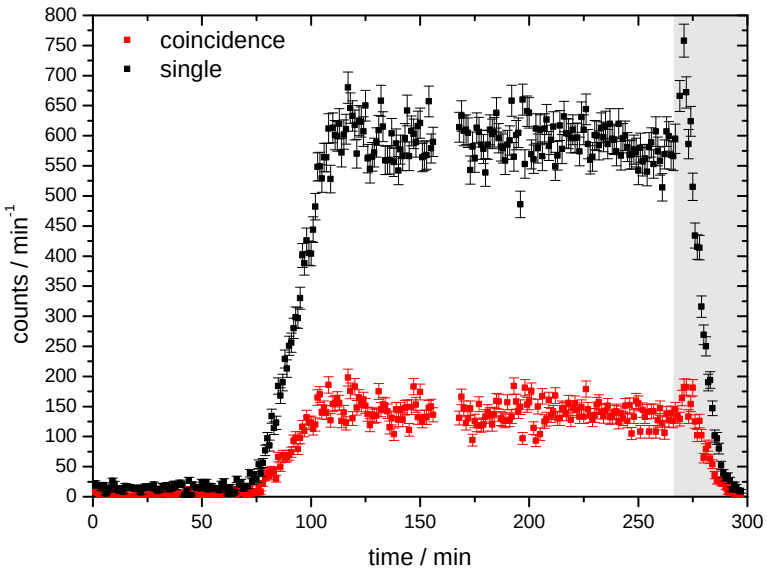

Figure 6.21.: The comparison of single (black) and coincidence (red) counts in the high gain of the inner segment of the A-detector (A1H). The shown uncertainty is the Poission error. The increasing count rate in the gray area is a disturbance due to the cut down of the balloon. These values are not a part of the analysis.

figure 6.22 in black. The values are averaged over 3 minutes and the shown error

bars are the SEMs. In addition, the ratio for the airplane measurement is shown in red. This value agrees very well with the balloon measurement. An expected value for an isotropic field (see below) is shown as the blue line. The balloon data shows that with higher altitude the field will get more isotropic. This behavior is expected because the shielding effect of the atmosphere decreases with higher altitude and thus also the absorption effect of inclined incident particles. For a

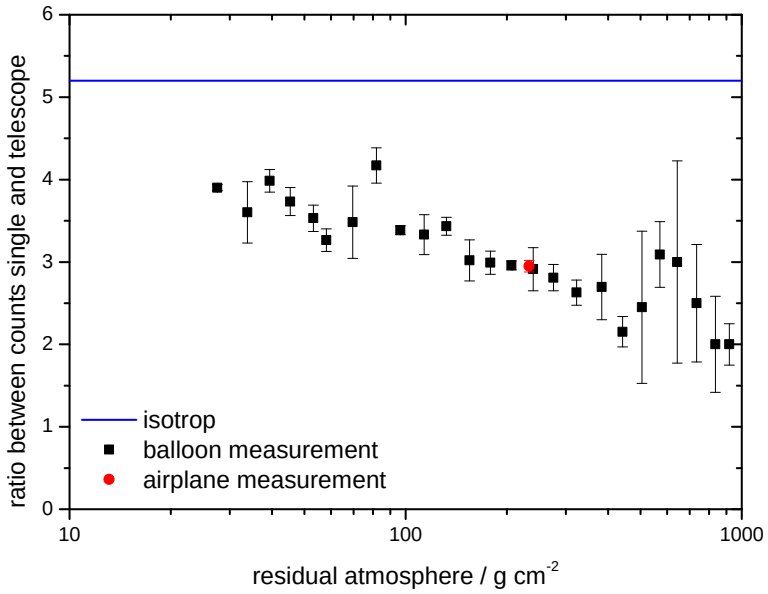

Figure 6.22.: The altitude dependence of the count rate ratio of single detector to telescope detector in black. The values are mean values of 3 minutes measurement times and the uncertainties are the SEM. The red dot shows the result of the airplane measurement and the blue line shows the expected value for an isotropic field.

detailed analysis the geometrical factor (GF) for a single planar detector and for the telescope which consists of the inner segments of the A and B detector, is calculated. The geometrical factor for a planar detector is defined as [*Sullivan*, 1971]:

$$GF = A \cdot 2\pi \cdot \int_0^{\frac{\pi}{2}} sin(\alpha) \cdot cos(\alpha) \cdot d\alpha = A \cdot \pi, \tag{6.4}$$

with A as the active area of the detector and α as the angle of incident. The result of GF for the inner segment of the A detector is:

$$GF = 4.41 \cdot \pi = 13.85 \text{ cm}^2\text{sr} \tag{6.5}$$

Sullivan [1971] describes a Monte Carlo method to calculate the geometrical factor for the telescope. This method was used by [*Köhler*, 2013] for the calculation of the geometrical factor for the telescope (A1B1), given by:

$$GF_T = 2.64 \text{ cm}^2\text{sr} \tag{6.6}$$

Because the geometrical factor is only defined for an isotropic field the ratio of GF and GF_T is the expected count rate ratio in an isotropic field (blue line in figure 6.22). Based on the measured ratios with FRED and the Monte Carlo simulation it is possible to determine the zenith angle distribution $W(\alpha)$ at common cruising altitude as well as at 25 km. The number of the detected particles (N) is defined as:

$$N = 2\pi \cdot A \cdot \int_0^{\frac{\pi}{2}} sin(\alpha) \cdot cos(\alpha) \cdot W(\alpha) \cdot d\alpha \tag{6.7}$$

In an isotropic field is $W(\alpha) = 1$. Figure 6.23 shows the simulation results of different zenith angle distributions $W(n, \alpha) = cos^n(\alpha)$ in black and the measured ratios of single and coincidence count rate at common cruising altitude given by the blue line. The red line represents the measured ratio at 25 km, while the dashed lines show the uncertainties for the respective measurement. It shows that a cos^2-distribution in common cruising altitudes and a cos-distribution for the zenith angle distribution reproduce the measured ratios. Table 6.8 shows a comparison of calculated and measured values. Furthermore, the results for calculations of the mean incident angle ($\bar{\alpha}$) for the particle telescope based on the Monte Carlo method are given. One can see that the difference of the mean incident angle for an isotropic and a cos^2-distribution is only in the order of 1°. With the mean incident angle ($\bar{\alpha}$) of the particle and the detector thickness (x) it is possible to calculate the mean path length ($\bar{l}$) for particles in the inner segment of detector A (A1) for the coincidence mode with the following relation:

$$\bar{l} = \frac{x}{cos(\bar{\alpha})} \tag{6.8}$$

The results of the calculation with a detector thickness of 300 μm is also given in table 6.8, showing only an insignificant difference of 3 μm between the isotropic and the cos^2-distribution. This reveals that the effect of a different zenith angle distribution to the mean path length is smaller than 1% and can be neglected. Consequently for the calculation of the LET the mean path length of an isotropic

[2] this ratio is independent of $W(\alpha)$

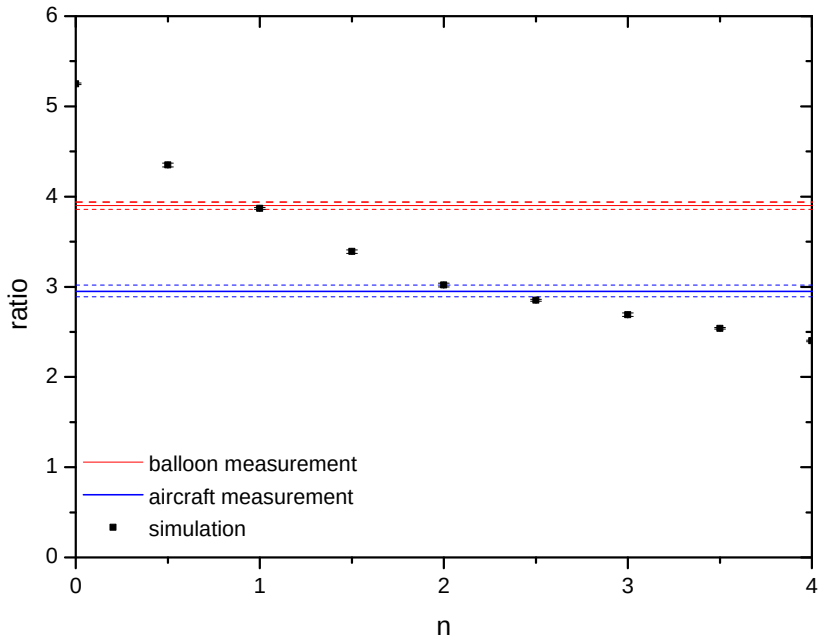

Figure 6.23.: The simulation result of different zenith angle distribution $W(n, \alpha) = cos^n(\alpha)$ shows the black dots. The blue line depicts the measured ratio of single and coincidence counts at common cruising altitude and the red line the measured ratio of the floating phase of the balloon (25 km).

Table 6.8.: The result of the zenith angle distribution ($W(\alpha)$), the mean incident angle $\bar{\alpha}$ and the mean path length $\bar{l}$ in A1 for common cruising altitude and 25 km.

$W(\alpha)$	measured ratio[2]	calculated ratio	$\bar{\alpha}$	$\bar{l}$ / μm
cos^2	2.95±0.07 (airplane)	3.02± 0.02	20.5 ∘	320
cos	3.90±0.04 (25 km)	3.87± 0.02	21.1 ∘	321
isotropic	-	5.25± 0.01	21.7 ∘	323

field at all altitudes was used. This is reasonable, especially considering that the uncertainty of the detector thickness, which is not specified by the manufacturer, would have a larger effect on the path length.

6.2.1.3. Neutral Count Rates

One major advantage of FRED has compared to other currently used charged particle detectors is its dedicated neutral particle channel (see chapter 5). Figure

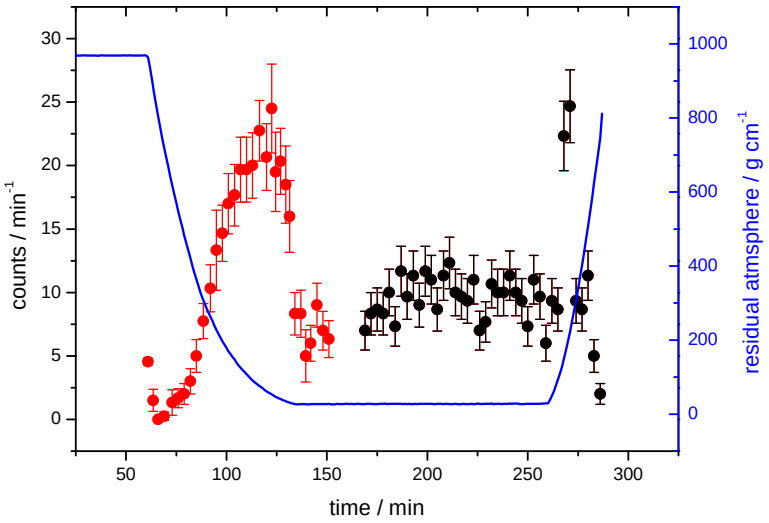

Figure 6.24.: The Neutral particle counts during the balloon flight. The red dots showed FRED in the normal mode (trigger > 60 keV) and the black dots displays the measurement with a higher trigger level (> 100 keV). The blue line shows the residual atmosphere

6.24 shows the 3 min mean valued time profile of the neutral particle count rate measured during the balloon flight. The red dots depict FRED in the normal mode (trigger level at 60 keV). The black dots display the measurement after switching the trigger level to 100 keV. The latter was necessary because a noise-problem becomes prominent in the inner segment of the C-detector during the floating phase (see data gap in figure 6.24). Additionally, the blue line shows the residual atmosphere during the measurement. After changing the trigger level (black dots) at first the counts shows a reasonably increase which then decreases slowly, although a constant count rate during the floating phase was expected. Furthermore, it should be expected that the count rate decreases after changing to a higher trigger level. Because of this unexpected behavior this phase of the measurement is not deemed reliable enough so that only the ascent phase of the balloon flight will be evaluated in more detail. Figure 6.25 shows the count rate in the neutral channel in dependence of the residual atmosphere. It shows that the count rate decreases directly after the launch at higher residual atmosphere due to neutral particles originating from the Earth's crust. After a few meters of altitude the count rate then increases up to a residual atmosphere of about $130\frac{g}{cm^2}$. For residual atmospheres smaller than $45\frac{g}{cm^2}$ a decreasing trend of the

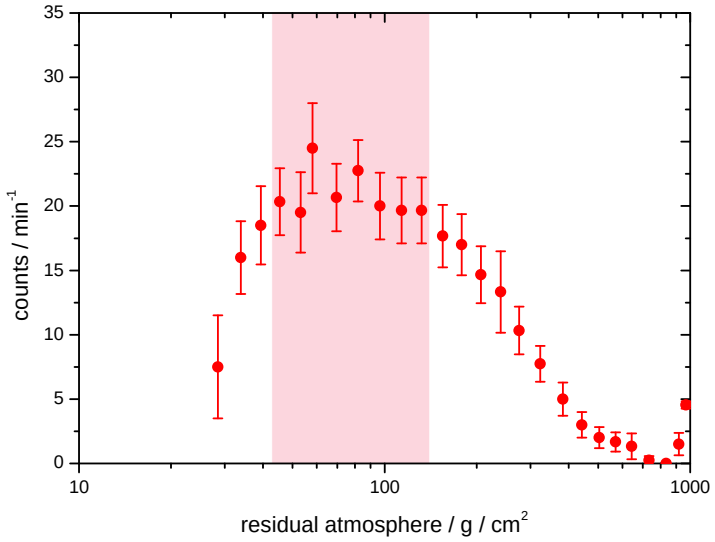

Figure 6.25.: The altitude dependence of the neutral count rate. The red area shows the wide spread maximum of the neutral particles in a range of 45 up to 130 $\frac{g}{cm^2}$ [*Möller et al.*, 2013b].

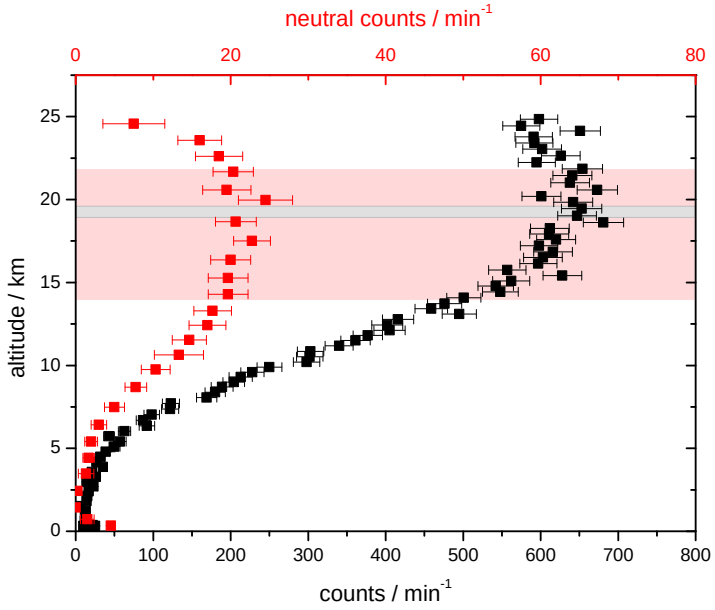

Figure 6.26.: The altitude dependence of the total count rate (black) and the neutral count rates (red). The gray area shows the Potzer Maximum and the red area the wide spread maximum of the neutral particles [*Möller et al.*, 2013b].

count rate is visible. In the range of 130 to 45 $\frac{g}{cm^2}$ the count rate shows an almost constant value considering of the Poisson uncertainty (red area in figure 6.25). Figure 6.26 shows a comparison of the altitude dependence of the charged particle (black dots) and neutral count rates (red dots). The gray area shows the result of the Pfotzer Maximum determination. A maximum of neutral particles can be seen between 14.5 and 22 km (red area). This comparison shows that the neutral particle counts differ by a factor of approximately 30 from the total count rates. Note that the different detection efficiencies for neutral and charged particles were not considered for this.

6.2.2. The Altitude Dependence of the Dose Rate in Silicon

In this section the altitude dependence of the measured absorbed dose rate in silicon is investigated. For this investigation a mean value, which is composed of the measured dose rate values in detector segment A1, A2, B1, B2 and C1 in an altitude range of 1 km, was calculated. Note that the other detector segments were neglected because they have no own trigger condition and thereby they are not comparable. Figure 6.27 shows the result of the mean values depending on the residual atmosphere as black dots. The uncertainty again is the SEM. Based on this data it was possible to adjust a mathematical function $\dot{D}(p)$ to the data which described the dose rate in silicon as a function of the residual atmosphere:

$$\dot{D}(p) = \dot{D}_0 + 2 \cdot \dot{D}_\mathrm{m} \cdot \left(1 + e^{(\frac{p-p_0}{S})}\right)^{-1} \tag{6.9}$$

where:

- $\dot{D}_0$ is the dose rate in Si on ground: 0.068 ± 0.003 μGy/h,
- $\dot{D}_\mathrm{m}$ is the maximum increase of the dose rate in Si: 8.75 ± 0.07 μGy/h,
- p_0 is the minimum of the residual atmosphere: 0 $\frac{g}{cm^2}$,
- S is the scale height: 124.11 ± 1.22 $\frac{g}{cm^2}$
- p is the value for the residual atmosphere

To determine the parameters of the fit function in eq.6.9 the dose rate data has been weighted with the number of data points for each individual altitude. The data points in the range of 30 to 50 g/cm^2 do not fit very well to the model

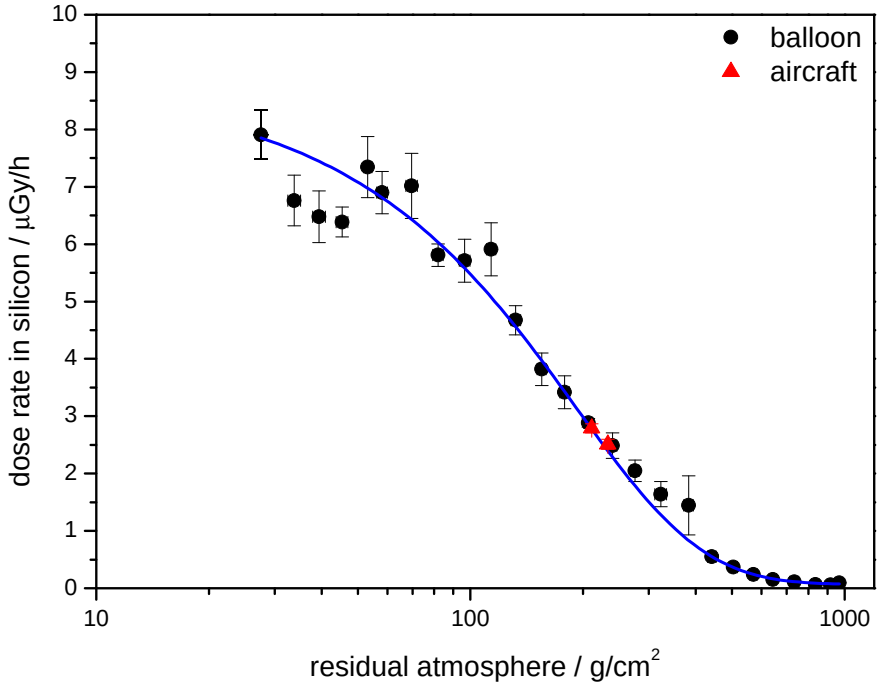

Figure 6.27.: Altitude dependence of the dose rate in silicon. The balloon measurement is shown in black, the aircraft measurement in the same vertical cut-off rigidity region (R_C=0.5 GV) and during comparable solar activity in red. The blue line displays the described model result.

because the balloon crossed these parts of the atmosphere in only 6 minutes and there were very few low gain triggers in this range of residual atmosphere. For example, figure 6.16 shows the time series for the A1 detector segment and these atmospheric layers were crossed in minutes 125 to 131. The lower panel displays the high gain count rate in blue and one can see that there are no counts during this time period.
To validate the model the red data points in figure 6.27 also show measurements from FRED taken onboard an aircraft in the same vertical cut-off rigidity region (R_C=0.5 GV) and during comparable solar activity. As can be seen the data are in very good agreement with the model developed in this work.

6.2.2.1. Absorbed Neutral Dose in Silicon

Figure 6.28 shows the altitude dependence of the absorbed neutral dose. These dose rates are calculated from the absorbed energy of the particles, which have

only interacted with the C1 detector segment. Again, the values are averaged

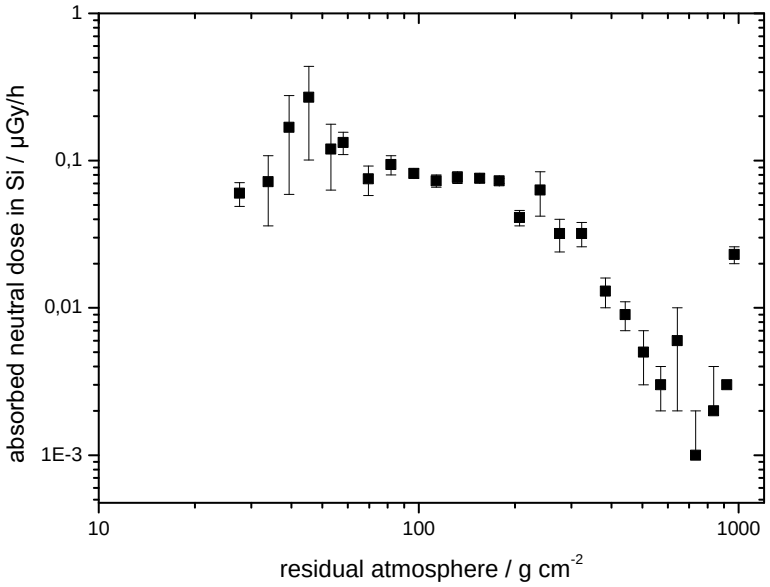

Figure 6.28.: Altitude dependence of the absorbed neutral dose rate in silicon.

over 3 minutes. One can see that the dose rate decreases directly after the launch as expected. After increasing altitude the count rate increases up to a residual atmosphere of about 230 $\frac{g}{cm^2}$ which is the common cruising altitude of an airplane. At this altitude the absorbed neutral dose rate reaches a constant level considering the uncertainties.

6.2.3. The Mean Quality Factor and the Dose Equivalent Rate

For the determination of the dose equivalent values the mean quality factor has to be calculated. By using coincidence condition between the A and B detector the LET of the particles from the energy loss spectrum can be determined. Figure 6.29 shows the LET in water for the inner segment of detector A measured at 25 km during the floating phase of the balloon. This spectrum was converted from the energy spectrum in silicon. For this conversion equation 6.10 was used to calculate the LET in water for every channel i.

$$LET_{\mathrm{i}}(water) \cong \frac{dE_{\mathrm{i}}}{l \cdot \rho_{\mathrm{Si}}} \cdot F_{\mathrm{Si-water}} \cdot \rho_{\mathrm{water}} \tag{6.10}$$

- l is the mean path length: 323 μm
- ρ_{Si} is the density of silicon: 2.33 g/cm^3

- $F_{\mathrm{Si-water}}$ conversion factor (silicon to water: 1.2)

- ρ_{water} is the density of water: 1 g/cm^3

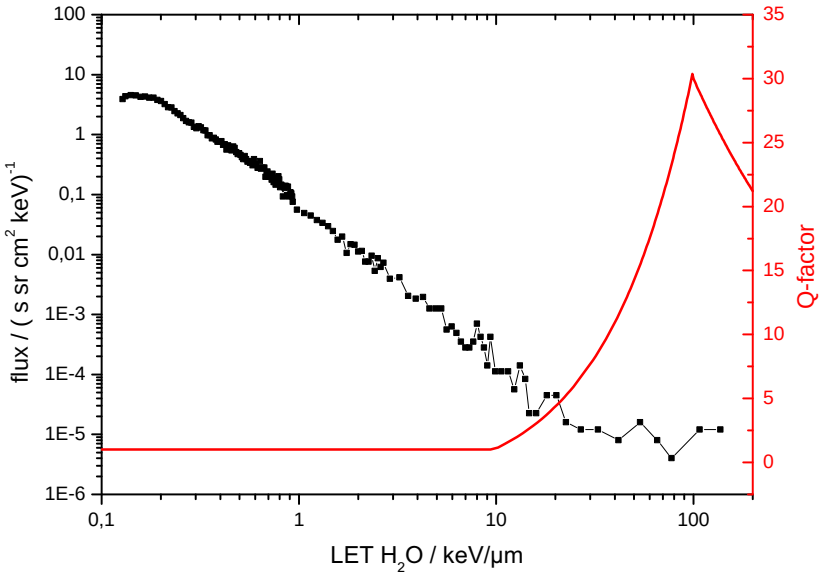

Figure 6.29.: The LET spectrum in water measured at an altitude of 25 km (black curve) and the ICRP60 function in red.

The water conversion factor $F_{\mathrm{Si-water}}$ considers the different stopping powers (deduced for electrons [*ICRU*, 1984]) of particles in water and silicon. *Roos* [1997] and *Beaujean et al.* [2005] showed that the dose rate in silicon can be converted into dose in water by using a conversion factor $F_{\mathrm{Si-water}} = 1.20$. By multiplying the ICRP 60 quality-factor function (red curve in figure 6.29) with the LET spectrum in water one can calculate a mean quality factor ($\bar{Q}$). Due to the determination of the LET in water it is possible to relate a quality factor function to every channel in the spectrum by using the ICRP function. The effect of the ICRP60 function to the measured dose is shown in figure 6.30. Here the black line shows the integrated absorbed dose in water while the red line gives the integrated dose equivalent. One can see that few particles with a LET above 10 keV/μm (see figure 6.29) create the main part of the dose equivalent because these particles have a higher biological effectiveness. The ratio between the total dose equivalent H and the total absorbed dose in water D_w is the mean quality

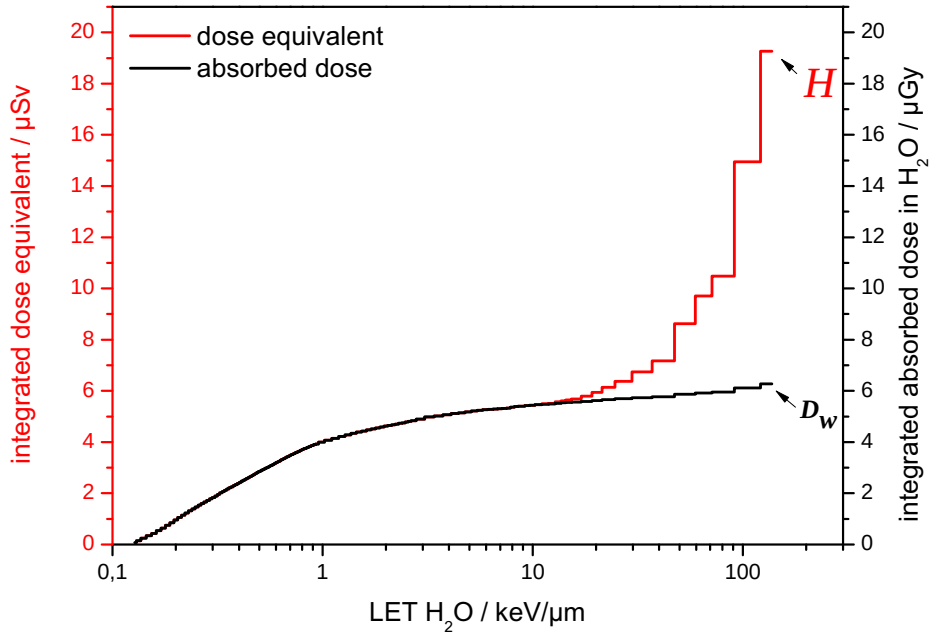

Figure 6.30.: The effect of the ICRP60 function on the measured dose. In black the integrated absorbed dose in water depends on the LET in water and in red the integrated dose equivalent.

factor ($\bar{Q}$) given by:

$$\bar{Q} = \frac{H}{D_w} \tag{6.11}$$

with the definition of the total absorbed dose in water D_w:

$$D_w = \sum_i D_\mathrm{i} \cdot F_{\mathrm{Si-water}} = \sum_i \frac{dE_\mathrm{i} \cdot N_\mathrm{i}}{m} \cdot F_{\mathrm{Si-water}} \tag{6.12}$$

- D_i: absorbed dose in Si for channel i
- N_Si: count rate in channel i
- dE_i: energy loss in channel i in J (1 eV=$1.6022 \cdot 10^{-19}$)
- m: mass of the detector in kg

and the definition of the total dose equivalent H:

$$H = \sum_i D_\mathrm{i} \cdot Q_i \cdot F_{\mathrm{Si-water}} \tag{6.13}$$

- Q_i: quality factor for channel i

In this work a mean quality factor of $\bar{Q} = 3.07 \pm 0.3$ is calculated. The uncertainty is an estimation based on the 10% value[3] published by *Beaujean et al.* [1999, 2005] because it is not possible to calculate a statistical uncertainty with only one measurement.
The DOSTEL onboard of the International Space Station (ISS) lead to the calculation of $\bar{Q} = 3.2 \pm 0.1$ [*Burmeister*, 2013] for comparable location (51.6° northern latitude) and solar activity. Both measurements are in good agreement with each other. Almost identical values onboard the ISS and at an altitude of 25 km were found.

Due to the various measurements of the mean quality factors in different alti-

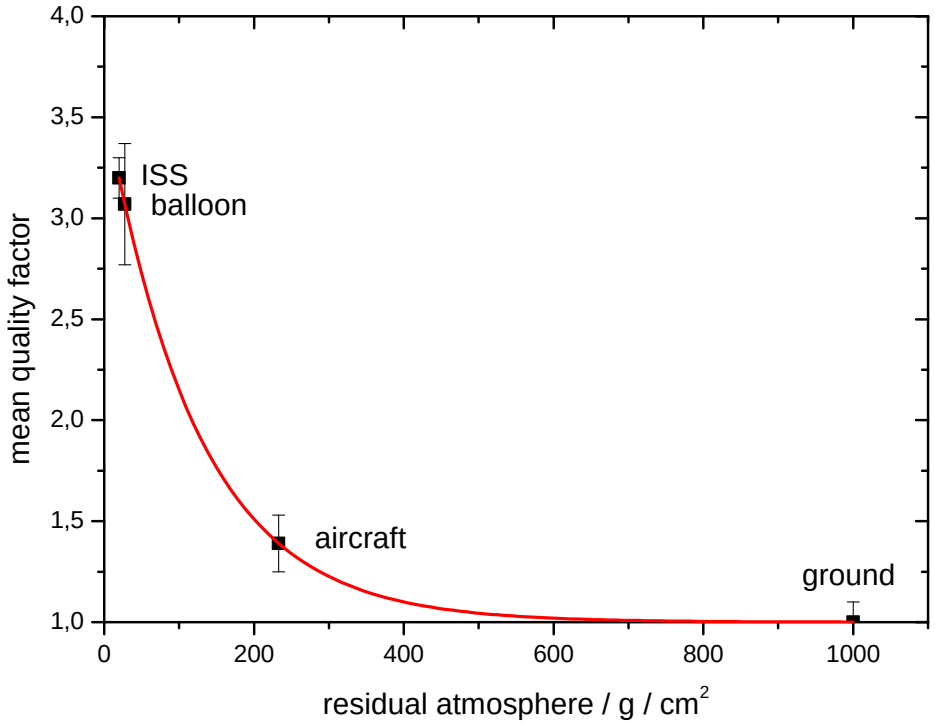

Figure 6.31.: The altitude dependence of the mean quality factor. The value for the ISS altitude was measured by DOSTEL for the northern latitude (55°) and similar solar activity. The other measurements were conducted with FRED.

tudes and in the same cut-off region it is - together with the DOSTEL measurements - possible to calculate an altitude dependency of the mean quality factor.

[3]For a detail explanation see chapter 6.1.3

Figure 6.31 shows the measurements in polar region as function of the residual atmosphere. The red curve shows the following fit function:

$$\bar{Q}(p) = \bar{Q}_0 + A \cdot e^{-\frac{p}{t}} \tag{6.14}$$

with:

- $\bar{Q}_0$=1, mean quality factor on ground
- $A = 2.59 \pm 8 \cdot 10^{-4}$
- $t = 123.11 \pm 0.14 \ \frac{g}{cm^2}$
- p= residual atmosphere in $\frac{g}{cm^2}$

For this comparison the result of the aircraft measurement from Tokio to Frankfurt was used because most of the flight was in a cut-off region near the magnetic poles. A mean altitude of FL350 was used. This is equivalent to a residual atmosphere of 238 g/cm^2 [*ISO*, 1975]. For more details on the mean quality factor see section 6.1.3.
The mean quality factor value measured on ground was 1 because there were no particles measured in the coincidence spectrum with an LET greater than 10 $keV/\mu m$. This is expected because only the minimally ionizing muon particles are measured in this mode.
With the altitude dependence of the mean quality factor $\bar{Q}(p)$ (see eq. 6.14), the water to silicon conversion factor $F = 1.20$, and the altitude dependence of the absorbed dose rate $\dot{D}(p)$ (see eq. 6.9) it is now possible to get an estimation for the altitude dependence of the dose equivalent rate up to 25 km:

$$\dot{H}(p) = F \cdot \bar{Q}(p) \cdot \dot{D}(p) \tag{6.15}$$

Figure 6.32 shows this estimation in red as well as the barometric dose rate model in silicon $\dot{D}(p)$ up to an altitude of 25 km (27 g/cm^2). At an altitude of 25 km a dose equivalent rate of around 30 μSv/h will be expected. Note that the measurement for the calculation of this model was done near solar minimum conditions. The heliospheric modulation potential Φ calculated by *Usoskin et al.* [2011] has a value of round about Φ=500 MV for the time of the measurements. For solar minimum conditions this potential has typical values between 300 and 400 MV, for the solar maximum values above 1200 MV are calculated.

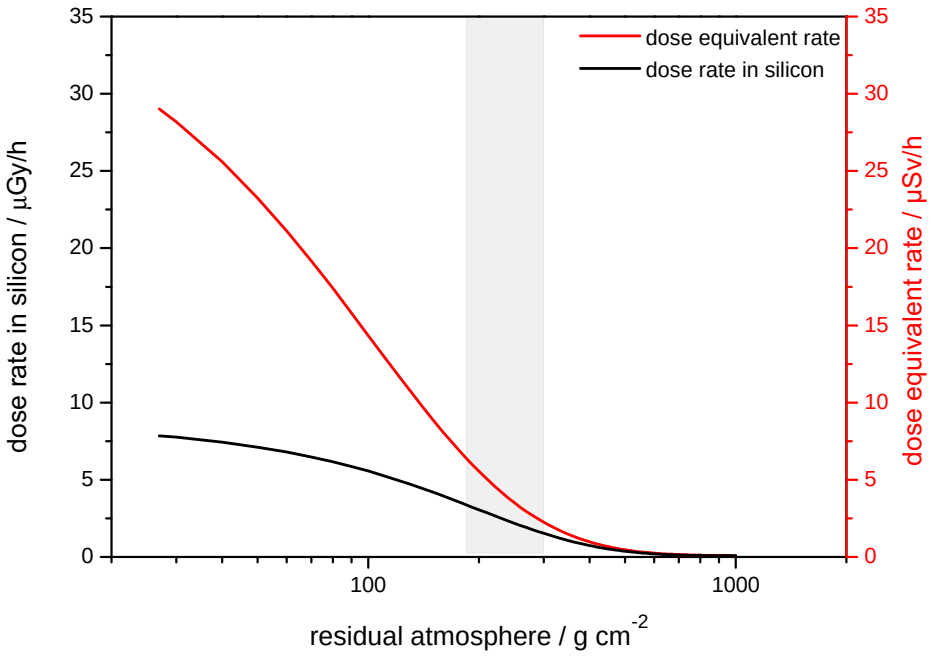

Figure 6.32.: The estimation of the altitude dependence of the dose equivalent rate (in red) and the absorbed dose rate model in silicon (in black).

As a consequence the dose rates decrease with increasing solar activity because the field conditions change. For a detailed analysis, one has also to consider that the dose equivalent is underestimated by a factor of ∼1.5 at common cruising altitude (gray area in figure 6.32) as described in chapter 6.1.3. The reason for this underestimation is that FRED measured mainly charged particles and the response to neutrons is rather poor because the energy transfer of neutron interactions in silicon is small (see section 4.2), and the main part of the dose equivalent at common cruising altitude is the neutron dose [*Baily*, 1982]. However, at higher altitudes charged particles are more dominant because the secondary production of the particles is smaller with increasing altitude and so the production of secondary neutrons, as shown e.g. by *Eyles et al.* [1972]. Protons, heavy nuclei from the secondary production and primary GCR become more important for the dose equivalent rate above the Pfotzer Maximum. Therefore, FRED shows an excellent performance at these altitudes and the presented values can be seen as an important contribution for future planned high altitude flights.

7. Conclusion

The main goal of this work was to measure the radiation exposure for high altitude flights. For this purpose, an unmanned balloon flight near the polar circle was performed. This place is well suited because the highest particle flux and dose rates are expected here. For this investigation the Flight Radiation Environment Detector (FRED) was developed and tested. FRED is composed of four segmented silicon semiconductor detectors. Due to their arrangement it is possible to distinguish between charged and neutral particles. Furthermore, the LET for charged particles can be determined by using coincidence condition with the limited path length according to the opening angle of the telescope.
For the purpose of this work FRED was tested with charged and neutral particles. The charged particle measurements were conducted with several heavy ions at the HIMAC in Japan. An additional measurement was done with a ^{207}Bi-source in order to acquire more data points for the high gain channel. Based on

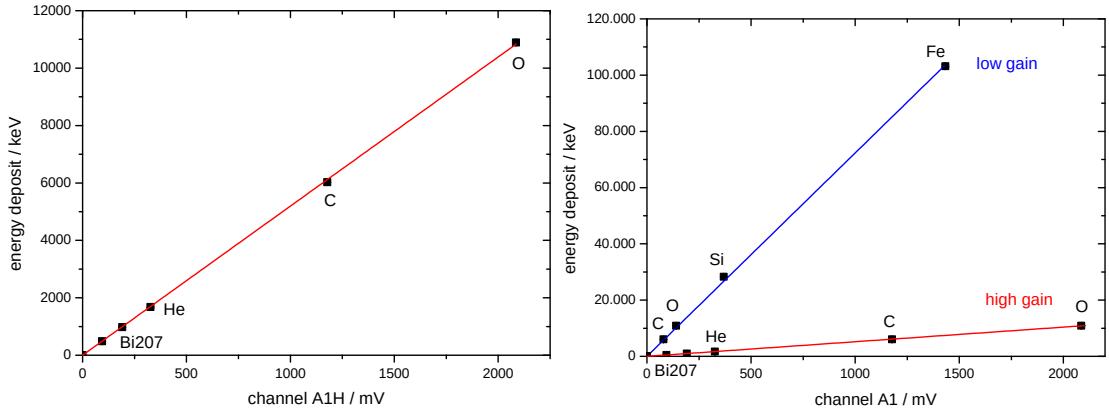

Figure 7.1.: Calibration curve for the high gain of the inner segment of the A-detector (A1H) on the left side (red curve) and the calibration curve for the same detector segment but for the low gain channel (A1L) on the right side (blue curve). Furthermore, a comparison of the two calibration curves is shown in the right panel.

these measurements a calibration of the detector was realized. Figure 7.1 shows the calibration curves for the inner segment of detector A. In the left panel the calibration curve for the high gain (red curve) and in the right panel for the low gain (blue curve) is shown. Furthermore, the right figure shows a comparison of these two curves. It was determined that FRED can measure the energy loss in silicon in a range of 60 keV up to 270 MeV which is equivalent to an LET in water of 0.1 up to 429.8 keV/μm.
The performance of the neutral channel was verified with several neutron measurements at the PTB in Braunschweig and at the iThemba labs in South-Africa. An additional measurement with a ^{137}Cs source was conducted at the Christian-Albrechts-Universität zu Kiel. This investigation has shown that neutron measurements are possible in principle. FRED shows clear neutron edges up to 8 MeV, which are produced by elastic scattering. Above 8 MeV the fraction of the secondary produced particles which can trigger the anticoincidence increases. Furthermore, the observed neutron edges disagree with the theoretical values. Figure 7.2 shows the ratio of measured to expected value in percent. Due to the

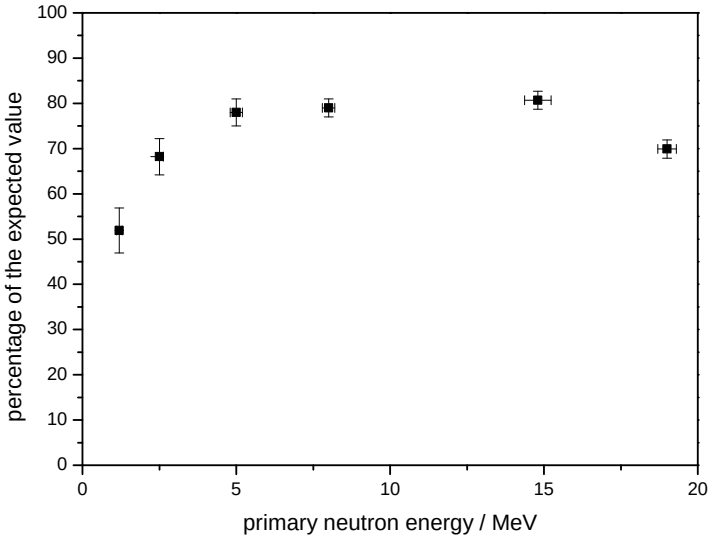

Figure 7.2.: The ratio of measured to expected value in percent

indirect measurement of neutrons by recoil silicon[1] this effect can be explained by the "plasma effect" which was observed for heavy ions [*Seibt et al.*, 1973]. The γ-ray source (^{137}Cs) measurement shows the expected behavior revealing that the

[1] for elastic scattering processes

energy gap between expected and measured value in the neutron measurements is no artifact of the calibration.

In order to verify the performance of FRED in a complex natural radiation field some measurements onboard aircraft were performed. These functionality tests have shown the expected behavior and an excellent performance in this radiation field as shown in Figure 7.3. In the left panel the linear increase of the absorbed

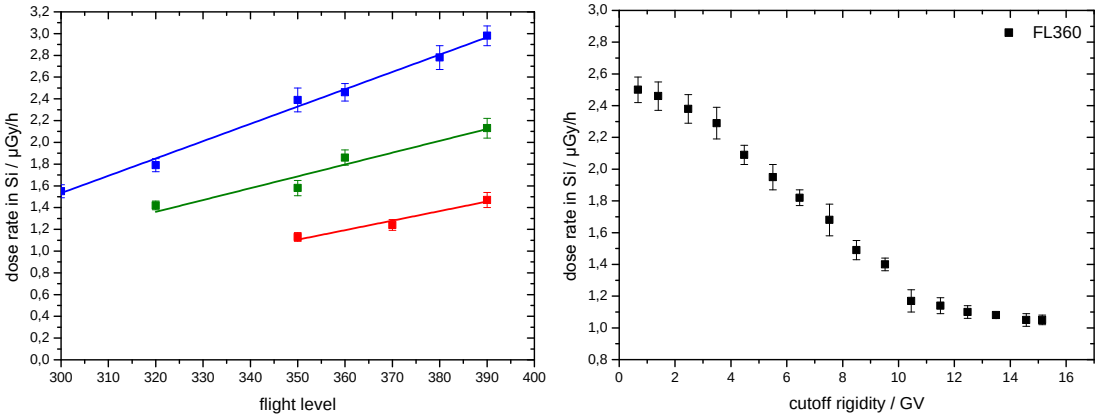

Figure 7.3.: On the left side: The altitude dependence of the dose rate at cruising altitudes measured onboard aircraft in the polar region (blue), in the transition region (green) and in the equator region (red) between the flight level 300 and 400. On the right side: The dose rate versus cut-off rigidity for the flight level 360 in a cut-off rigidity interval of 1 GV.

dose rate in silicon for the polar region (blue), the transition region (green), and the equator region (red) for flight level between 300 and 400 are shown. The right panel shows the expected sigmoid trend of the absorbed dose rate in silicon depending on the cut-off rigidity.

For the investigation in higher altitudes FRED was part of the payload onboard a stratospheric balloon which was launched near Kiruna in the northern part of Sweden. The Pfotzer Maximum was determined to be at a residual atmosphere of 64±3 $\frac{g}{cm^2}$ which is equivalent to an altitude range of 18.9 and 19.6 km. This is in good agreement with other measurements in the polar region, see e.g. [*Bazilevskaja et al.*, 2008]. Figure 7.4 shows in black the altitude dependence of the total count rate in black and for the neutral count rate in red. The Pfotzer maximum range is shown as gray area. Due to the fact that the neutral count rate is composed of γ-rays and neutron hits it shows a wide spread maximum in

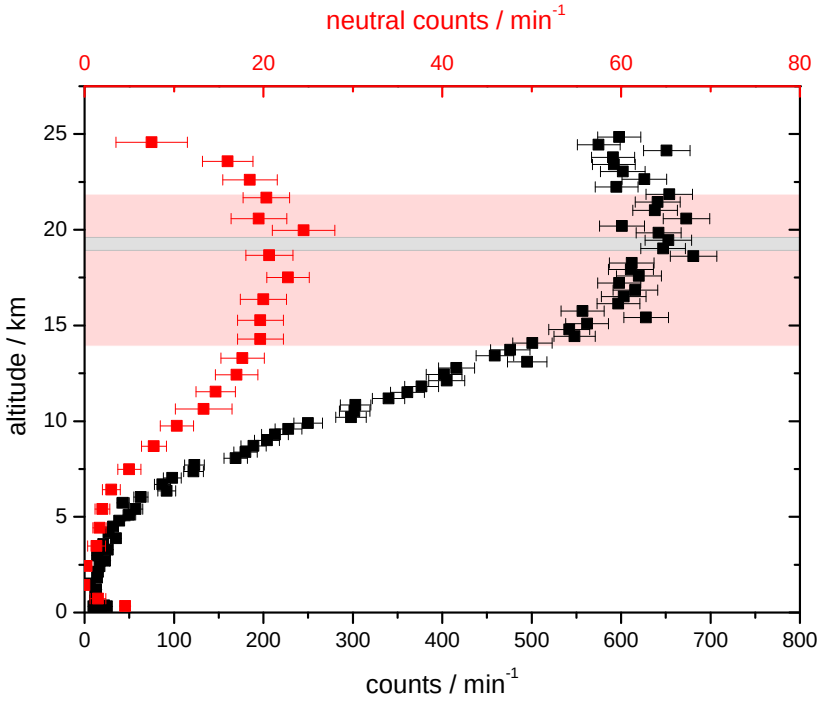

Figure 7.4.: The altitude dependence of the total count rate (black) and the neutral count rates (red). The gray area shows the Potzer maximum and the red area the wide spread maximum of the neutral particles.

the range of 14.5 and 22 km. Based on the measured data onboard the balloon a mathematical function $\dot{D}(p)$ was developed which is given by:

$$\dot{D}(p) = \dot{D}_0 + 2 \cdot \dot{D}_\mathrm{m} \cdot \left(1 + e^{\left(\frac{p-p_0}{S}\right)}\right)^{-1}$$

where:

- $\dot{D}_0$ is the dose rate in Si on ground: 0.068 ± 0.003 μGy/h,
- $\dot{D}_\mathrm{m}$ is the maximum increase of the dose rate in Si: 8.75 ± 0.07 μGy/h,
- p_0 is the minimum of the residual atmosphere: 0 $\frac{g}{cm^2}$,
- S is the scale height: 124.11 ± 1.22 $\frac{g}{cm^2}$

This function describes the dose rate in silicon as a function of the residual atmosphere. Furthermore, the altitude dependence of the mean quality factor $\bar{Q}(p)$ was determined:

$$\bar{Q}(p) = \bar{Q}_0 + A \cdot e^{-\frac{p}{t}}$$

where:

- $\bar{Q}_0 = 1$, mean quality factor on ground
- $A = 2.59 \pm 8 \cdot 10^{-4}$
- $t = 123.11 \pm 0.14 \ \frac{g}{cm^2}$
- p residual atmosphere in $\frac{g}{cm^2}$

Finally it was possible to estimate the dose equivalent rate in an altitude of 25 km. Figure 7.5 shows in black the calculated dose rate in silicon based on

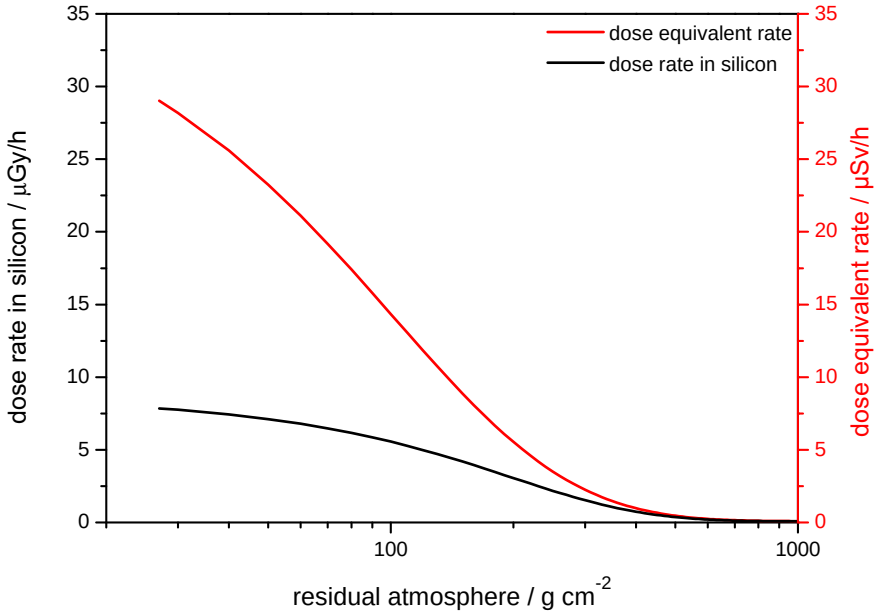

Figure 7.5.: The estimation of the altitude dependence of the dose equivalent rate (in red) and the absorbed dose rate model in silicon (in black).

the barometric dose rate model and in red the corresponding dose equivalent rate. One can see that a dose equivalent rate up to 30 μSv/h can be expected. Figure 7.6 shows a comparison of the measured radiation exposure with others. The value on 25 km is comparable with the radiation exposure onboard the ISS. Furthermore, this figure shows that in the polar regions the measured value on 25 km is 5 times larger than at common cruising altitudes (10 km). One important factor for the radiation exposure at 25 km is the time spend at this altitude. If the flight time for the same destination is 5 times faster than by a commercial

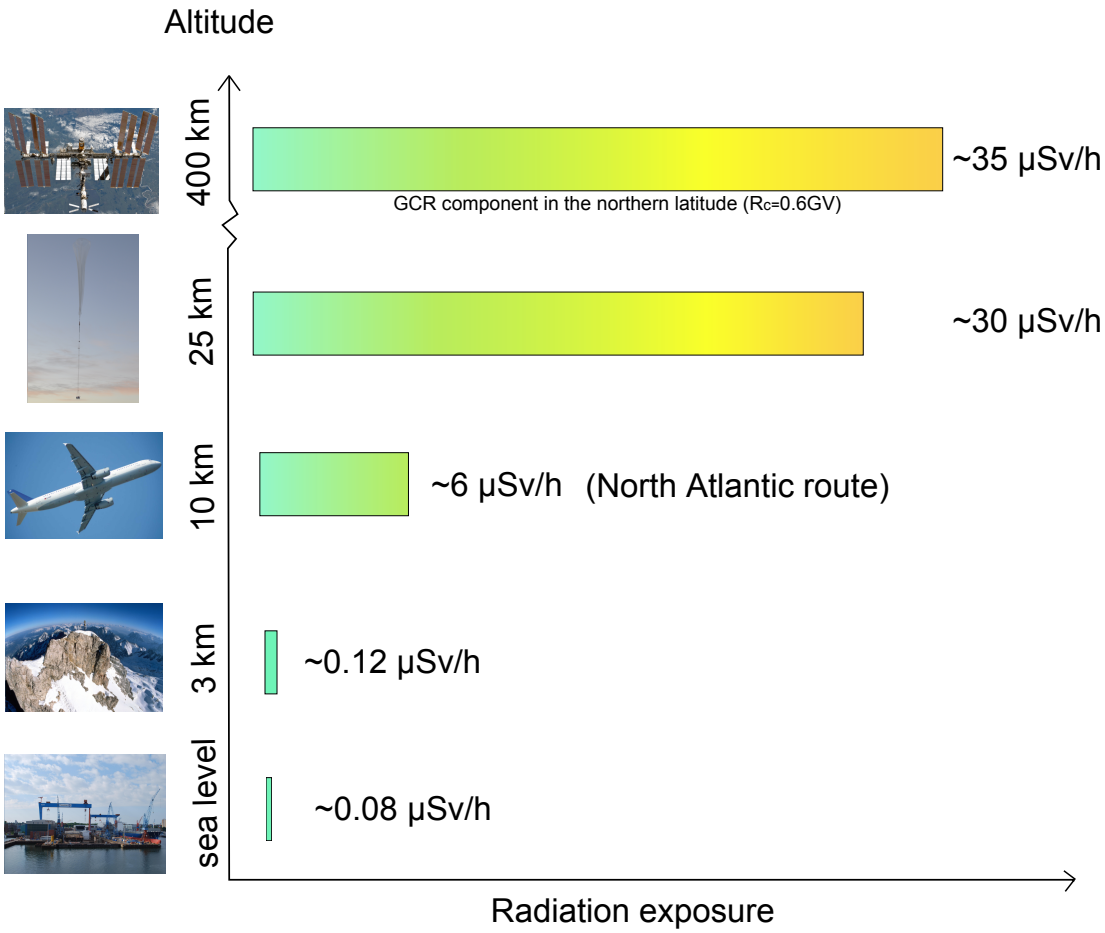

Figure 7.6.: A comparison of the measured radiation exposure at 25 km with others.

airplane the total radiation exposure will be comparable with that at common cruising altitudes. This work has shown that the radiation exposure should be monitored at high altitude flights. For this monitoring dosemeters which are suitable to measure in a mixed radiation field should used, like e.g. FRED. FRED is suitable for this task because it has a wide LET range in water (from 0.1 up to 429.8 keV/μm), it can distinguish between charged and neutral particles and the response to charged particles is very good which are dominates the radiation field at 25 km.

Outlook

For a detailed investigation of the radiation exposure in the stratosphere further measurements are necessary. For example to obtain sufficiently good statistics in

the high LET range to calculate a better mean quality factor one needs a long duration balloon flight with a floating phase of several days. Additionally, several balloon flights at different altitudes could be helpful to improve the altitude dependence of the mean quality factor. Furthermore, a long floating time is necessary to obtain good results for the neutral spectrum due to the low count rate. Taking into account that FRED can not distinguish between neutrons and gammas a more detailed simulation should be conducted for the analysis of the neutral spectrum due to the indirect measurement method of the neutrons and gammas. *Köhler* [2012] shows a possibility for the analysis of separate neutron- and gamma-spectra by inversion calculation. This is a complex method which could not be realized in the frame of this work.

The observed plasma effect could be investigated in more detail for neutron interaction with silicon, e.g. measurements with different detector bias voltage could be done to optimize the effect, because the plasma effect is expected to depend on it.

Bibliography

Allkofer, O., *Teilchendetektoren*, Verlag Karl Thieming, 1971.

Baily, P., Neutron Radiation Dosimetry in High Altitude Flight Personnel, *Aviat. Space Environ, Med. 53(8)*, 808–817, 1982.

Bazilevskaja, G., et al., Cosmic Ray Induced Ion Production in the Atmosphere, *Space Sci. Rev.*, *137*, 149–173, 2008.

Beaujean, R., J. Kopp, and G. Reitz, Radiation Exposure in Civil Aircraft, *Radiation Protection Dosimetry*, *85*, 287–290, 1999.

Beaujean, R., S. Burmeister, F. Petersen, and G. Reitz, Radiation Exposure Measurement Onboard Civil Aircraft, *Radiation Protection Dosimetry*, *Vol. 116*, 312–315, 2005.

Beringer, J. et al. (Particle Data Group), *Cosmic Rays Phys. Rev. D86, 010001*, Particle Data Group, 2012.

Büsching, I., A. Kopp, M. Pohl, R. Schlickeiser, C. Perrot, and I. Grenier, Cosmic-ray propagation properties for an origin in supernova remnants, *The Astrophysical Journal*, *619*, 314–326, 2005.

Burmeister, S., private comunication, from Christian-Albrechts-Universität zu Kiel, 2013.

Casolino, M., N. De Simone, D. Bongue, M. De Pascale, V. Di Felice, L. Marcelli, and the PAMELA Group, Two Years of Flight of the Pamela Experiment: Results and Perspectives, *ArXiv:0810.4980v1*, 2008.

Demtröder, W., *Experimentalphysik 4 Kern-, Teilchen- und Astrophysik*, Springer-Verlag, 2005.

Desorgher, L., E. Flückiger, and M. Gurtner, The PLANETOCOSMICS Geant4 Application, in *36th COSPAR Scientific Assembly*, 2006.

Eyles, C., A. Linney, and R. G.K., A Measurement of the Atmospheric Neutron Flux in the Energy Range 50<E<350MeV, *Planet Space Sci.*, *20*, 1955–1922, 1972.

Goldhagen, P., J. Clem, and J. Wilson, The Energy Spectrum of Cosmic-Ray Induced Neutron Measured on an Airplane Over a Wide Range of Altitude and Latitide, *Radiation Protection Dosimetry*, *110*, 387–392, 2004.

Grieder, P. K., *Cosmic Rays at Earth*, Elsevier, 2001.

Hamrita, H., et al., Description of Current Pulses Induced by Heavy Ions in Silicon Detectors (II), *Nuclear Instruments and Methods in Physics Research A 642(2011)59-64*, *642*, 59–64, 2011.

Herbst, K., Interaction of Cosmic Rays with The Eath' s Magnetosphere and Atmosphere - Modeling the Cosmic Ray Induced Ionization and the Production of Cosmogenic Radionuclides, Ph.D. thesis, Christian-Albrechts-Univesität zu Kiel, 2012.

Hertz, G., *Lehrbuch der Kernphysik, Band II, Physik der Atomkerne*, Verlag Werner Dausien Hanau/Main, 1961.

Hess, V., Über Beobachtungen der durchdringenden Strahlung bei sieben Freiballonfahrten, *Physikalische Zeitschr.*, *13*, 1084–1091, 1912.

ICRP, 1990 Recommendations of the International Commission on Radiological Protection, *Pergamon Press, Oxford, United Kingdom*, *ICRP Publication 60, Ann. ICRP 21(1-3)*, 1991.

ICRU, *Stopping Powers for Electrons and Protons*, Report 37, International Commission on Radiation Units and Measurement Bethesda, MD:ICRU, 1984.

ISO, *Standard Atmosphere, ISO 2533:1975*, International Organization for Standardization, 1975.

Köhler, J., Gamma/neutron Separation in the Martian Radiation Environment, Ph.D. thesis, Christian-Albrechts-Universität zu Kiel, 2012.

Köhler, J., private comunication, from Christian-Albrechts-Universität zu Kiel, 2013.

Knoll, G. F., *Radiation Detection and Measurement*, John Wiley & Sons Inc, 2000.

Krieger, H., *Strahlenphysik, Dosimetrie und Strahlenschutz*, Teubner, 2002.

Laskowski, W., and W. Pohlit, *Biophysik*, Stuttgart, 1974.

Leo, W., *Techniques for Nuclear and Particle Physics Experiments*, Springer-Verlag, 1987.

Longair, M., *High Energy Astrophysics*, Cambridge University Press., 1992.

Möller, T., *Charakterisierung eines Dosimeters zur Messung der Ortsdosisleistung in Flughöhen*, Christian-Albrechts-Universität zu Kiel, Diploma thesis, 2008.

Möller, T., O. Burda, S. Burmeister, B. Heber, F. Langer, and F. Wissmann, In-field Calibration of the Navigation Dosimetry System (NAVIDOS) During Solar Minimum Conditions, *Astrophysics and Space Sciences Transactions*, *8*, 45–49, 2012.

Möller, T., T. Berger, S. Böttcher, S. Burmeister, E. Ehresmann, B. Heber, L. Labrenz, J.and Panitzsch, and R. Wimmer-Schweingruber, The Calibration of the Flight Radiation Environment Detector (FRED), in *Proceedings of 33nd International Cosmic Ray Conference, Rio De Janeiro*, 2013a.

Möller, T., B. Ehresmann, J. Labrenz, and L. Panitzsch, Radiation Measurement on the Stratospheric Balloon BEXUS13, in *Proceedings of 21th Symposium on European Rocket and Balloon Programmes and Related Research*, 2013b.

Möller, T., et al., Longterm Monitoring of Ambient Dose Equivalent Rates at Aviation Altitudes, in *38th COSPAR Scientific Assembly*, *COSPAR Meeting*, vol. 38, p. 3228, 2010.

Musiol, G., J. Ranft, R. Reif, and D. Seelinger, *Kern- und Elementarteilchenphysik*, Deutscher Verlag der Wissenschaft, 1992.

Nolte, R., et al., Quasi-Monoenergetic Neutron Reference Fields in the Energy Range From Thermal to 200 MeV, *Radiation Protection Dosimetry*, *110. Nos 1-4*, 97–102, 2004.

Pauls, M., *Entwicklung eines Neutronendetektors für Dosimetrie*, Christian-Albrechts-Universität zu Kiel, Diploma thesis, 1998.

PDG, *Particle Data Group, http://pdg.lbl.gov/*, Particle Data Group, 2008.

Pfotzer, G., Dreifachkoinzidenzen der Ultrastrahlung aus vertikaler Richtung in der Stratosphere, *Zeitschrift für Physik*, *102*, 23/43, 1936.

Prölss, G., *Physik des erdnahen Weltraums*, Springer-Verlag, 2004.

Roos, F., *Messung der Strahlenexposition in Verkehrsflugzeugen mit einem Halbleiterdetektor*, Christian-Albrechts-Universität zu Kiel, Diploma thesis, 1997.

Röttger, S., private comunication, from Physikalisch-Technische Bundesanstalt, 2013.

Sato, T., and K. Niita, Analytical Functions to Predict Cosmic-Ray Neutron Spectra in the Atmosphere, *Radiat. Res.*, *166*, 544–555, 2006.

Schrewe, U., Global Measurements of the Radiation Exposure of Civil air Crew From 1997 to 1999, *Radiation Protection Dosimetry*, *91*, 347 – 364, 2000.

Seibt, W., K. Sunderström, and Tove.P.A., Charge Collection in Silicon Detectors for Strongly Ionizing Particles, *NUCLEAR INSTRUMENTS AND METHODS*, *113*, 317–324, 1973.

Simpson, J., Elemental and Isotopic Compostion of the Galatic Cosmic Rays, *Annual Reviews of Nuclear and Particle Science*, *33*, 323–381, 1983.

Simpson, J. A., The cosmic ray nucleonic component: The invention and scientific uses of the neutron monitor, *Space Sci. Rev.*, *93*, 11–32, 2000.

Stöcker, H., *Taschenbuch der Physik, Formeln, Tabellen, Übersichten*, Verlag Harri Deutsch, 2004.

Strahlenschutzkommission, *Die Ermittlung der durch kosmische Strahlung verursachten Strahlenexposition des fliegenden Personals*, Gustav Fischer, 1997.

StrlSchV, *Verordnung über den Schutz vor Schäden durch ionisierende Strahlen*, BGB1, 2001.

Sullivan, J., Geometrical Factor and Directional Response of Single Multi-Element Particle Telescopes, *Nuclear Instruments and Methods*, *95*, 5–11, 1971.

Tove, P., and W. Seibt, Plasma Effects in Semiconductor Detectors, *Nuclear Instruments and Methods*, *51*, 261–269, 1967.

Usoskin, I., G. Bazilevskaya, and G. Kovaltsov, Solar Modulation Parameter for Cosmic Rays Since 1936 Reconstructed From Ground Based Neutron Monitors and Ionization Chambers, *Journal of Geophysical Research*, *116*, A02,104, 2011.

Van Allen, J., and H. Tatel, The cosmic ray Counting rate of a Single Geiger Counter from Ground Level to 161 Kilometers Altitude., *Phys. Rev.*, *73(3) Second. ser.*, 245–254, 1948.

Von Lany, C., Grundlegende physikalische Nachweiseigenschaften des Dosimetrie-Teleskops DOSTEL für Neutronen, Ph.D. thesis, Christian-Albrechts-Universität zu Kiel, 2001.

Williams, R., and E. Lawson, The Plasma Effect in Silicon Semiconductor Radiation Detectors, *Nuclear Instruments and Methods*, *120*, 261–268, 1974.

Wirtz, K., and K. H. Beckurts, *Elementare Neutronenphysik*, Springer-Verlag, 1958.

Wissmann, F., Long-Term Measurements of $\dot{H}^*(10)$ at Aviation Altitudes in the Northern Hemisphere., *Radiation Protection Dosimetry*, *No. 4*, 347–357, 2006.

Ziegler, J., SRIM-2003, *Nuclear Instruments and Methods in Physics Research*, *B 219-220*, 1027–1036, 2004.

A. Data Sheet of FRED

Flight Radiation Environment Detector

Detectors:	4 segmented Canberra PIPS Detector
Form:	squared
Edge length:	3 cm
Edge length inner segment:	2.2 cm
Edge length inner segment C1:	2.1 cm (guard ring CX)
Active area A1:	4.41 cm^2
Active area A2:	4.16 cm^2
Active area B1:	4.84 cm^2
Active area B2:	4.16 cm^2
Active area C1:	4.41 cm^2
Active area C2:	4.16 cm^2
Active area D1:	4.84 cm^2
Active area D2:	4.16 cm^2
Detector thickness	300 μm
Geometrical factor telecope A1B1:	2.64 $cm^2 \cdot$ sr
Distance A to B detector:	2.29 cm
Distance B to C detector:	0 cm (glued together)
Distance C to D detector:	0.105 cm
Total dE range in Si:	60 keV - 270 MeV
Total LET Range in water:	0.1 - 429.8 keV/μm
Dimension:	11.2 cm x 10 cm x 9.95 cm
Weight:	371 g
Power consumption:	2.7 W
Detector bias voltage:	-50 V
EMC qualification	RTCA/DO-160F

dE range in Si A1H:	77.85 keV - 18.165 MeV
dE range in Si A2H:	78.90 keV - 18.410 MeV
dE range in Si B1H:	78.75 keV - 18.375 MeV
dE range in Si B2H:	78.60 keV - 18.340 MeV
dE range in Si C1H:	60.00 keV - 17.500 MeV
dE range in Si C2H:	73.50 keV - 17.150 MeV
dE range in Si D1H:	76.20 keV - 17.780 MeV
dE range in Si D2H:	75.45 KeV - 17.605 MeV

dE range in Si A1L:	1.084 MeV - 253.038 MeV
dE range in Si A2L:	1.098 MeV - 256.267 MeV
dE range in Si B1L:	1.107 MeV - 258.358 MeV
dE range in Si B2L:	1.161 MeV - 271.065 MeV
dE range in Si C1L:	1.057 MeV - 246.750 MeV
dE range in Si C2L:	1.066 MeV - 248.846 MeV
dE range in Si D1L:	1.050 MeV - 245.008 MeV
dE range in Si D2L:	1.002 MeV - 233.970 MeV

B. Calibration Curves and Values

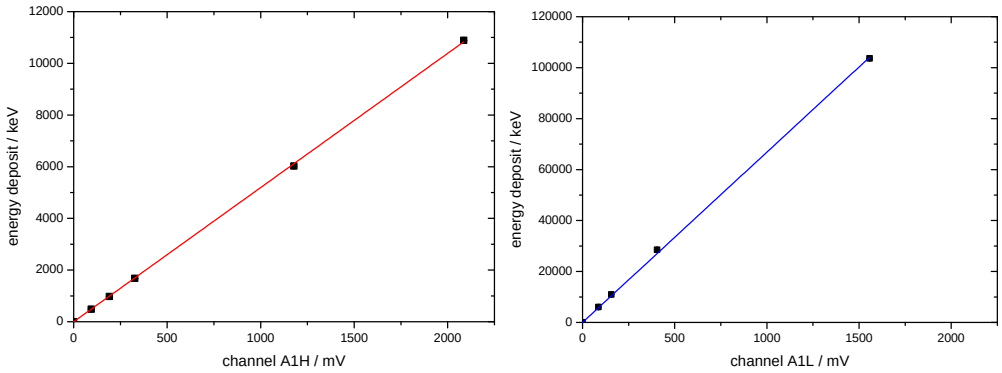

Figure B.1.: Calibration curves A1. On the left side in red for the high gain channel and on the right side in blue for the low gain channel.

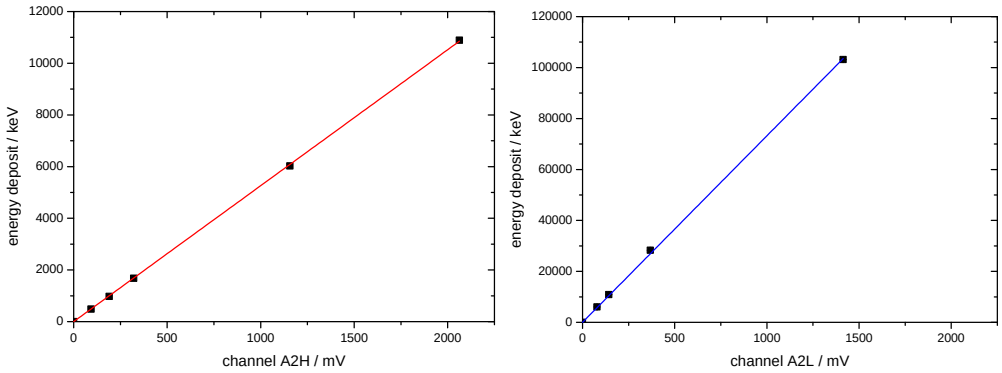

Figure B.2.: Calibration curves A2. On the left side in red for the high gain channel and on the right side in blue for the low gain channel.

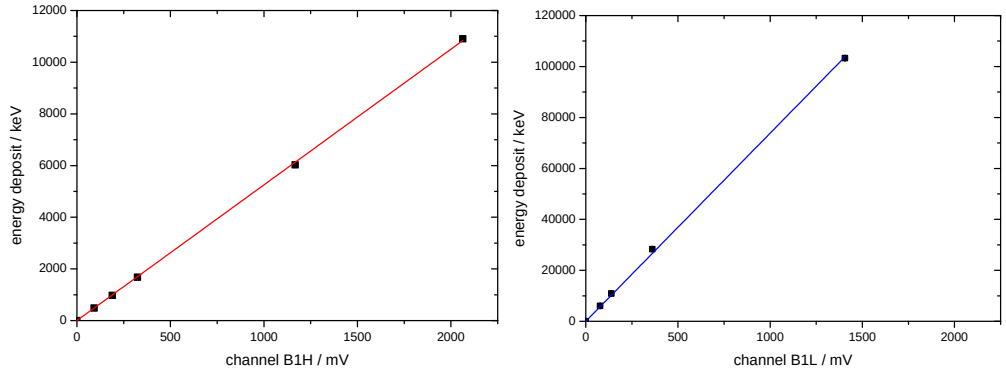

Figure B.3.: Calibration curves B1. On the left side in red for the high gain channel and on the right side in blue for the low gain channel.

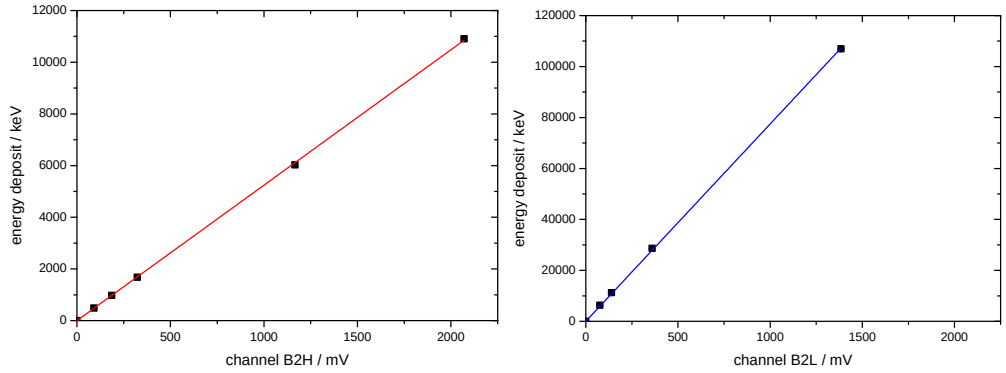

Figure B.4.: Calibration curves B2. On the left side in red for the high gain channel and on the right side in blue for the low gain channel.

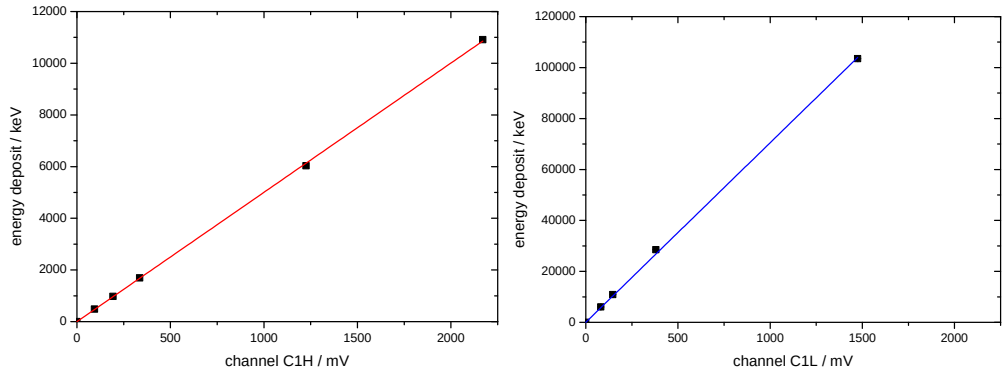

Figure B.5.: Calibration curves C1. On the left side in red for the high gain channel and on the right side in blue for the low gain channel.

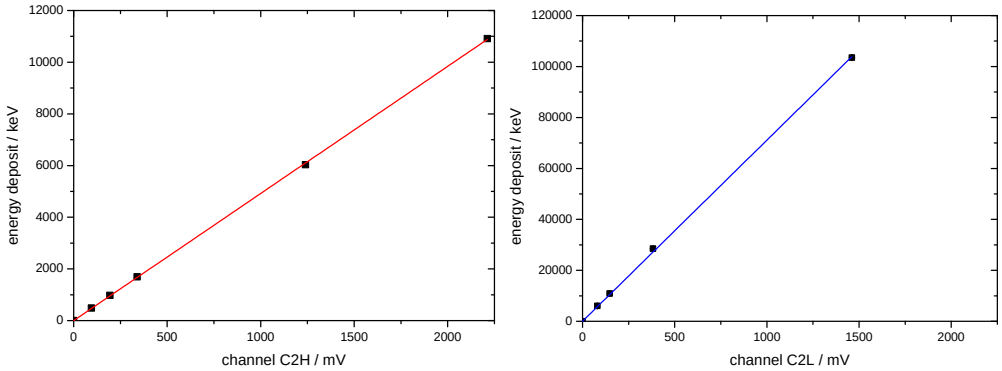

Figure B.6.: Calibration curves C2. On the left side in red for the high gain channel and on the right side in blue for the low gain channel.

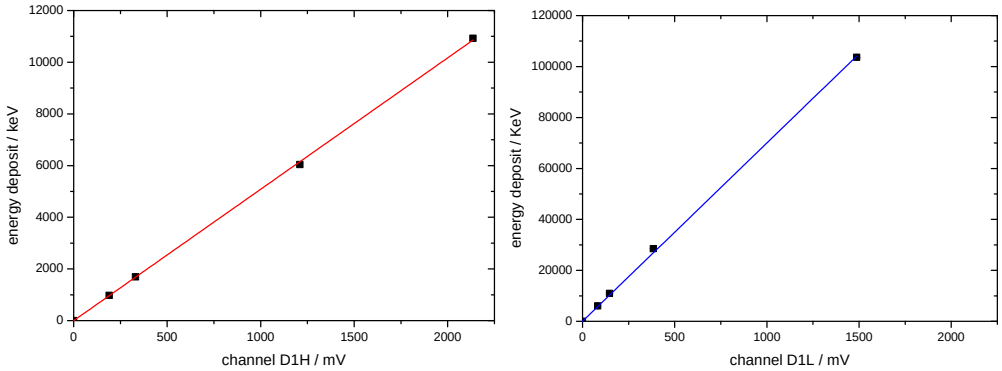

Figure B.7.: Calibration curves D1. On the left side in red for the high gain channel and on the right side in blue for the low gain channel.

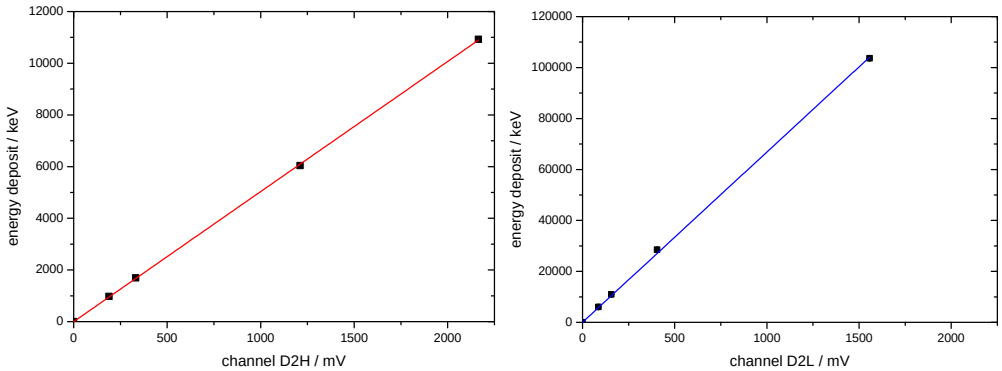

Figure B.8.: Calibration curves D2. On the left side in red for the high gain channel and on the right side in blue for the low gain channel.

Table B.1.: Calibration values A1H

source	Energy / keV	uncertainty / keV	channel / mV	uncertainty / mV
^{207}Bi	481.7	-	93.8	3
^{207}Bi	975.7	-	191.3	3
He 100[1]	1680	8.4	326.7	2
C 400[1]	6024	30.1	1177.6	2
O 400[1]	10893	54.5	2086.3	1

Table B.2.: Calibration values A1L

source	Energy / keV	uncertainty / keV	channel / mV	uncertainty / mV
C 400[1]	6024	30.1	79.5	1
O 400[1]	10893	54.5	140.6	1
Si 600[1]	28293	141.5	369.4	2
Fe 500[1]	103140	515.7	1433.0	3

Table B.3.: Calibration values A2H

source	Energy / keV	uncertainty / keV	channel / mV	uncertainty / mV
^{207}Bi	481.7	-	93.0	3
^{207}Bi	975.7	-	190.0	3
He 100[1]	1680	8.4	321.1	2
C 400[1]	6024	30.1	1156.3	2
O 400[1]	10893	54.5	2063.1	1

Table B.4.: Calibration values A2L

source	Energy / keV	uncertainty / keV	channel / mV	uncertainty / mV
C 400[1]	6024	30.1	78.9	1
O 400[1]	10893	54.5	142.4	1
Si 600[1]	28293	141.5	367.9	2
Fe 500[1]	103140	515.7	1414.1	3

[1] in MeV/nuc

Table B.5.: Calibration values B1H

source	Energy / keV	uncertainty / keV	channel / mV	uncertainty / mV
^{207}Bi	481.7	-	92.5	3
^{207}Bi	975.7	-	189.0	3
He 100[1]	1680	8.4	323.8	2
C 400[1]	6027	30.1	1167.4	2
O 400[1]	10902	54.5	2063.7	1

Table B.6.: Calibration values B1L

source	Energy / keV	uncertainty / keV	channel / mV	uncertainty / mV
C 400[1]	6027	30.1	77.5	1
O 400[1]	10902	54.5	139.1	1
Si 600[1]	28320	141.6	361.0	2
Fe 500[1]	103290	516.5	1405.5	3

Table B.7.: Calibration values B2H

source	Energy / keV	uncertainty / keV	channel / mV	uncertainty / mV
^{207}Bi	481.7	-	91.0	3
^{207}Bi	975.7	-	186.0	3
He 100[1]	1680	8.4	323.5	2
C 400[1]	6027	30.1	1166.7	2
O 400[1]	10902	54.5	2070.4	1

Table B.8.: Calibration values B2L

source	Energy / keV	uncertainty / keV	channel / mV	uncertainty / mV
C 400[1]	6300	31.5	76.2	1
O 400[1]	11220	56.1	139.7	1
Si 600[1]	28680	143.4	360.1	2
Fe 500[1]	106970	534.9	1384.3	3

Table B.9.: Calibration values C1H

source	Energy / keV	uncertainty / keV	channel / mV	uncertainty / mV
^{207}Bi	975.7	-	193.0	3
^{207}Bi	481.7	-	94.2	3
He 100[1]	1690	8.5	335.3	2
C 400[1]	6033	30.2	1225.3	2
O 400[1]	10911	54.6	2170.2	1

Table B.10.: Calibration values C1L

source	Energy / keV	uncertainty / keV	channel / mV	uncertainty / mV
C 400[1]	6033	30.2	81.4	1
O 400[1]	10911	54.6	146.2	1
Si 600[1]	28497	142.5	380.6	2
Fe 500[1]	103470	517.4	1474.7	3

Table B.11.: Calibration values C2H

source	Energy / keV	uncertainty / keV	channel / mV	uncertainty / mV
^{207}Bi	481.7	-	95.0	3
^{207}Bi	975.7	-	193.8	3
He 100[1]	1690	8.5	339.6	2
C 400[1]	6033	30.2	1239.8	2
O 400[1]	10911	54.6	2211.7	1

Table B.12.: Calibration values C2L

source	Energy / keV	uncertainty / keV	channel / mV	uncertainty / mV
C 400[1]	6033	30.2	80.4	1
O 400[1]	10911	54.6	147.6	1
Si 600[1]	28497	142.5	381.9	2
Fe 500[1]	103470	517.4	1460.8	3

Table B.13.: Calibration values D1H

source	Energy / keV	uncertainty / keV	channel / mV	uncertainty / mV
^{207}Bi	975.7		190.0	3
He 100[1]	1690	8.5	331.3	3
C 400[1]	6036	30.2	1209.9	2
O 400[1]	10923	54.6	2135.7	1

Table B.14.: Calibration values D1L

source	Energy / keV	uncertainty / keV	channel / mV	uncertainty / mV
C 400[1]	6036	30.2	82.5	1
O 400[1]	10923	54.6	146.3	1
Si 600[1]	28515	142.6	384.1	2
Fe 500[1]	103650	518.3	1487.6	3

Table B.15.: Calibration values D2H

source	Energy / keV	uncertainty / keV	channel / mV	uncertainty / mV
^{207}Bi	975.7		189.0	3
He 100[1]	1690	8.5	331.6	3
C 400[1]	6036	30.2	1211.0	2
O 400[1]	10923	54.6	2164.3	1

Table B.16.: Calibration values D2L

source	Energy / keV	uncertainty / keV	channel / mV	uncertainty / mV
C 400[1]	6036	30.2	86.7	1
O 400[1]	10923	54.6	156.3	1
Si 600[1]	28515	142.6	405.0	2
Fe 500[1]	103650	518.3	1556.9	3

C. Performance Mesurements

For verification tests of FRED measurements with Polyethylene (PE) at the HI-MAC were performed. Figure C.1 shows in red the primary beam measurement without PE for oxygen on the left panel and for silicon on the right panel. The black curves depicted are the measurements with PE. The PE was placed between the beam window and in a distance of 40 cm to the instrument FRED. These histograms show two effects. First, one can see an energy loss shift to higher energies (black curves) due to the fact that the particles lost a part of their energy in the PE. Because of this their velocity decreased and thus their energy lost in the detectors increased. The second effect is that particles fragmented through nuclear interactions with the PE. This fragmentation occurs also during the primary measurements by interaction with the air molecules, beam window and the beam monitor, but it is not as pronounced. Because of this, the primary silicon peak is smeared out.

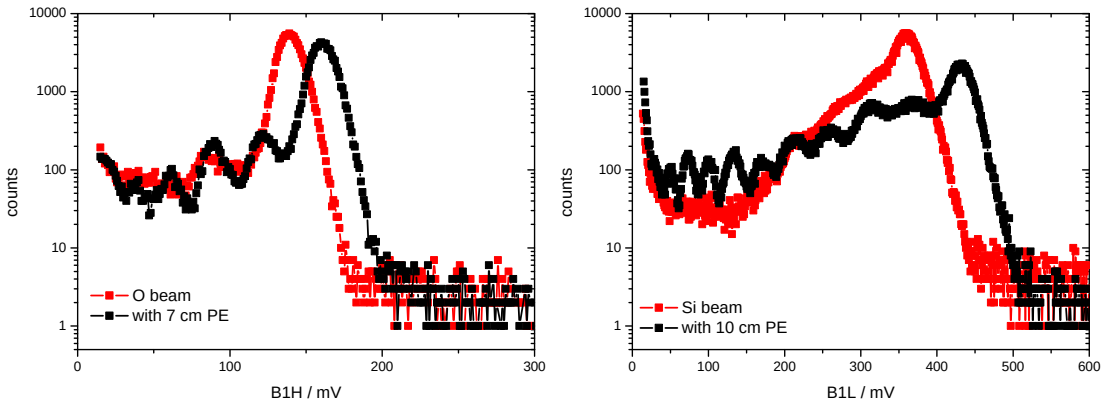

Figure C.1.: Absorber measurements with oxygen on the left side and with silicon on the right side measured in the B1L channel. The red curve depicts the primary beam measurements without absorber and the black curve with PE.

Figure C.2 shows the 2D histograms from the absorber measurements. It shows the signals in the A1L- versus the B1L-detector segment. The histogram on the left side depicts the oxygen measurement with 7 cm PE and the figure on the right side shows the silicon measurement with 10 cm PE. It shows the produced fragments as spots. These fragments can not be used for the calibration because the measured position in the spectrum is not clearly defined due to the contamination of the single spots through other fragments. This can be seen as smeared fragment spots in the 2D spectrum of the silicon measurement.

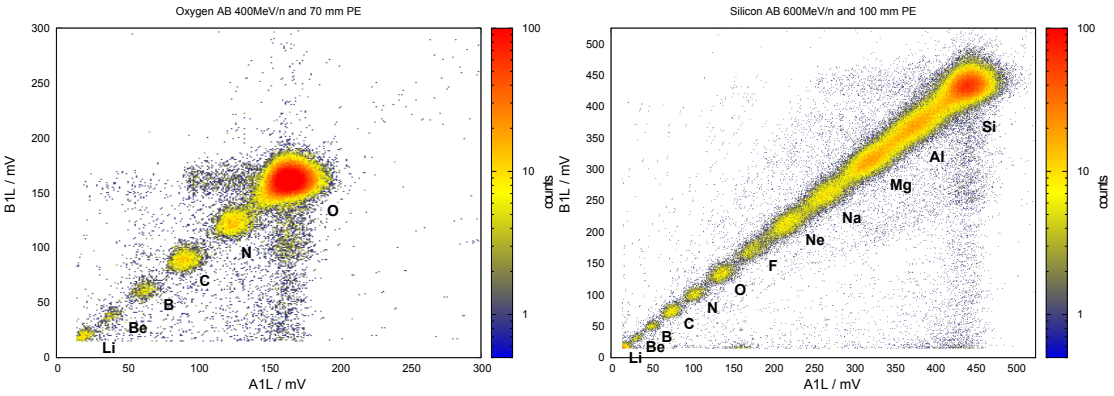

Figure C.2.: The 2-dimensional histogram of the Absorber measurements. On the left side the signals in the A1L- versus the B1L-detector segment for the oxygen measurement with 7 cm PE and on the right side for the silicon measurement with 10 cm PE.

List of Figures

1.1. The natural radiation exposure in several altitudes 2
1.2. Subsonic aircraft 3

2.1. Viktor Hess in his balloon 5
2.2. The energy spectrum of the GCR 6
2.3. The development of the radiation field in the Earth's atmosphere. 7
2.4. Intensity of charged particles in dependence of the altitude 8
2.5. Kiel neutron monitor count rates 9
2.6. Vertical cut-off rigidity 11
2.7. Proton flux in different cut-off regions 11
2.8. Interaction processes in the atmosphere 12
2.9. Particle cascade 14

3.1. The quality factor depending on the LET 18
3.2. The radiation field in cruising altitudes 21
3.3. The ambient dose equivalent rate in cruising altitudes 22

4.1. Bragg-Peak 24
4.2. Reaction channels of the compound nuclear reaction with Si . . . 27
4.3. An ideal γ-ray spectrum for a detector 29

5.1. The mechanical design of FRED. 31
5.2. Cross section of the Detector Stack. 32
5.3. Schematic of the electronics 33
5.4. Schematic of the detector arrangement 34
5.5. Heavy ion measurements 36
5.6. The iron measurement 36
5.7. Calibration measurement with 400 MeV/nuc carbon for low gain of A1-Detector 37

5.8. Calibration curve for the inner segment of the A-Detector (A1) . . 38
5.9. The ^{207}Bi energy loss spectrum 39
5.10. The ^{207}Bi intercalibration of A1H and B1H 40
5.11. The ^{207}Bi intercalibration of C1H 41
5.12. The low-energy neutron spectra 43
5.13. Neutron cross section 44
5.14. Error function fit 45
5.15. The ratio of measured to expected value 46
5.16. Neutron correction function 47
5.17. Spectral fluence of the high-energy neutron measurement 48
5.18. High-energy neutron measurement 49
5.19. High-energy neutron spectrum 50
5.20. High-energy neutron 2D spectra 50
5.21. γ-source measurement 51

6.1. The flight path NRT-FRA 53
6.2. The measurement flights NRT-FRA 54
6.3. The flight path FRA-JNB 55
6.4. The measurement flight FRA-JNB 56
6.5. The altitude dependence of the dose rate in cruising altitudes . . 57
6.6. The dose rate versus cut-off rigidity. 59
6.7. Energy loss spectrum of airplane measurement 59
6.8. Neutral spectrum 60
6.9. The percentage of the composition of the ambient dose equivalent rate 62
6.10. The flight path of the BEXUS13 balloon. 63
6.11. The BEXUS13 lift off at ESRANGE near Kiruna. 64
6.12. The open gondola during the mounting phase. 65
6.13. BEXUS13 housekeeping data from the flight train. 65
6.14. The count rate time profile of the balloon measurement 66
6.15. Dose rate time profile measured on the balloon 67
6.16. Dose rate time profile for the A-detector 67
6.17. Comparison of count rates 68
6.18. Determination of the Pfotzer Maximum 69
6.19. Altitude versus residual atmosphere 71

6.20. Altitude versus counts 71
6.21. Comparison of single and coincidence counts 72
6.22. Altitude dependence of the count rate ratio 73
6.23. The zenith angle distribution 75
6.24. Neutral particle counts during the balloon flight 76
6.25. The altitude dependence of the neutral count rate 77
6.26. The altitude dependence of the total count rate and the neutral count rate. 77
6.27. Altitude dependence of the dose rate in silicon 79
6.28. Altitude dependence of the absorbed neutral dose rate 80
6.29. The LET spectrum in water measured during the balloon flight . 81
6.30. The effect of the ICRP60 function on the measured dose 82
6.31. The altitude dependence of the mean quality factor 83
6.32. The altitude dependence of the dose equivalent rate 85

7.1. Calibration curve for the inner segment of the A-Detector (A1) . . 87
7.2. The percentage of the expected value 88
7.3. Results of the measurements onboard aircraft 89
7.4. The altitude dependence of the total count rate and the neutral count rates. 90
7.5. The altitude dependence of the dose equivalent rate 91
7.6. Comparison of radiation exposure values 92

B.1. Calibration curves A1 103
B.2. Calibration curves A2 103
B.3. Calibration curves B1 104
B.4. Calibration curves B2 104
B.5. Calibration curves C1 104
B.6. Calibration curves C2 105
B.7. Calibration curves D1 105
B.8. Calibration curves D2 105

C.1. Absorber measurements 111
C.2. The 2D histogram of the Absorber measurements 112

List of Tables

3.1. Radiation weighting factor 19
3.2. Maximal accepted values in Germany 20

5.1. Calibration values 38
5.2. Energy loss ranges 39
5.3. Neutron uncertainty 42
5.4. recoil Si in Si 47

6.1. The altitude dependence of the dose rate (aircraft) 58
6.2. Mean quality factors onboard aircraft 61
6.3. Measured total dose onboard aircraft 61
6.4. Measured neutral dose onboard aircraft 62
6.5. Pfotzer Maximum fit parameter 70
6.6. Altitude conversion function fit parameter 70
6.7. Pfotzer Maximum 72
6.8. Zenith angle distribution, mean incident angle, mean path length 75

B.1. Calibration values A1H 106
B.2. Calibration values A1L 106
B.3. Calibration values A2H 106
B.4. Calibration values A2L 106
B.5. Calibration values B1H 107
B.6. Calibration values B1L 107
B.7. Calibration values B2H 107
B.8. Calibration values B2L 107
B.9. Calibration values C1H 108
B.10. Calibration values C1L 108
B.11. Calibration values C2H 108

B.12.Calibration values C2L 108
B.13.Calibration values D1H 109
B.14.Calibration values D1L 109
B.15.Calibration values D2H 109
B.16.Calibration values D2L 109

Danksagung

An dieser Stelle möchte ich mich bei den Menschen bedanken, die mich tatkräftig bei der Fertigstellung dieser Arbeit unterstützt haben. Mein besonderer Dank gilt dabei...

- ... Herrn Prof. Dr. Bernd Heber, der mir die Möglichkeit gab diese Thema zu bearbeiten und jederzeit bereit war über Ergebnisse zu diskutieren. Außerdem bin ich ihm sehr dankbar, dass er mir die vielen Dienstreisen ermöglichte, um diese Arbeit fertig zu stellen.
- ... Herrn Prof. Dr. Robert Wimmer-Schweingruber, der mir durch die Bereitstellung der Experiment Einzelteile erst die Bearbeitung des Themas ermöglichte.
- ... Herrn Dr. Sönke Burmeister für die Anregungen und wissenschaftlichen Diskussionen zu dieser Arbeit.
- ... Herrn Dr. Stephan Böttcher für die Fertigstellung der Elektronik und Herrn Lars Seimetz für die Unterstützung bei CAD Problemen und Fragestellungen.
- ... der DLR Raumfahrtagentur für die Möglichkeit zur Teilnahme am REXUS-BEXUS Programm. Insbesondere möchte ich mich bei Herrn Mark Fittock und Herrn Martin Sigle vom DLR Bremen für die Unterstützung und Organisation während des REXUSBEXUS Programms bedanken. Außerdem gilt mein Dank dem ESRANGE Team für die gute Zusammenarbeit während der BEXUS 11 und 13 Startkampange.
- ... Herrn PD Dr. Frank Wissmann und seinem Team für die Möglichkeit FRED an der PTB mit Neutronen zu bestrahlen.
- ... dem iThemba Labs Team für die gute Strahlzeit am Neutronbeschleuniger in Südafrika.
- ... dem HIMAC Team für die guten Strahlzeiten am Schwerionen Beschleuniger in Chiba. Insbesondere möchte ich mich bei Herrn Hisashi Kitamura bedanken für seine Hilfe während des Aufenthalts in Japan. Ohne seine Übersetzungen wäre der Aufenthalt fast unmöglich gewesen.

- ... dem SpaceLife Programm, wodurch die eine oder andere Tagung und Dienstreise erst ermöglicht wurde. Außerdem möchte ich mich an dieser Stelle bei meinem DLR Betreuer Herrn Dr. Thomas Berger für die wissenschaftlichen Diskussionen bedanken.

- ... der gesamten Abteilung Extraterrestrischen Physik der CAU für das gute und angenehme Arbeitsklima und den vielen Diskussionen die zwischen Tür und Angel gehalten wurden.

- ... Herrn Dr. Bent Ehresmann, Herrn Dr. Konstantin Herbst, Herrn Johannes Labrenz und Herrn Jan-Eike Thomssen für das kritische Durchsehen meiner Arbeit und die vielen guten Anregungen.

- ... meinen Eltern für die Unterstützung während des gesamten Studiums.

- ... zu guter Letzt meiner Freundin Mona Bogs, die mich vor allem während der Endphase der Arbeit immer unterstützt hat.

Eidesstattliche Versicherung

Hiermit versichere ich an Eides Statt, dass ich die vorliegende Arbeit abgesehen vom Rat meiner akademischen Lehrer ohne fremde Hilfe und lediglich unter der Verwendung der angegebenen Literatur sowie den bekannten Nachschlagewerken der Naturwissenschaften angefertigt habe, und sie nach Inhalt und Form meine eigene ist. Diese Arbeit ist unter Einhaltung der Regeln guter wissenschaftlicher Praxis entstanden. Des Weiteren versichere ich, dass diese Arbeit weder ganz noch teilweise an anderer Stelle zur Prüfung vorlag. Frühere Promotionsversuche wurden von mir nicht vorgenommen.

Wie im Text verwiesen, sind Teile der Arbeit in folgenden Tagungsbeiträgen veröffentlicht:

Möller, T. and Berger, T. and Böttcher, S. and Burmeister, S. and Ehresmann, E. and Heber, B. and Labrenz, J.and Panitzsch, L. and Wimmer-Schweingruber, R.F., *The Calibration of the Flight Radiation Environment Detector (FRED)*, Proceedings of 33nd International Cosmic Ray Conference, Rio De Janeiro, 2013.

Möller, T. and Ehresmann, B. and Labrenz, J. and Panitzsch, L., *Radiation Measurement on the Stratospheric Balloon BEXUS13*, Proceedings of 21th Symposium on European Rocket and Balloon Programmes and Related Research, Switzerland, 2013.

Kiel, den

Thomas Möller